II. Research Highlights

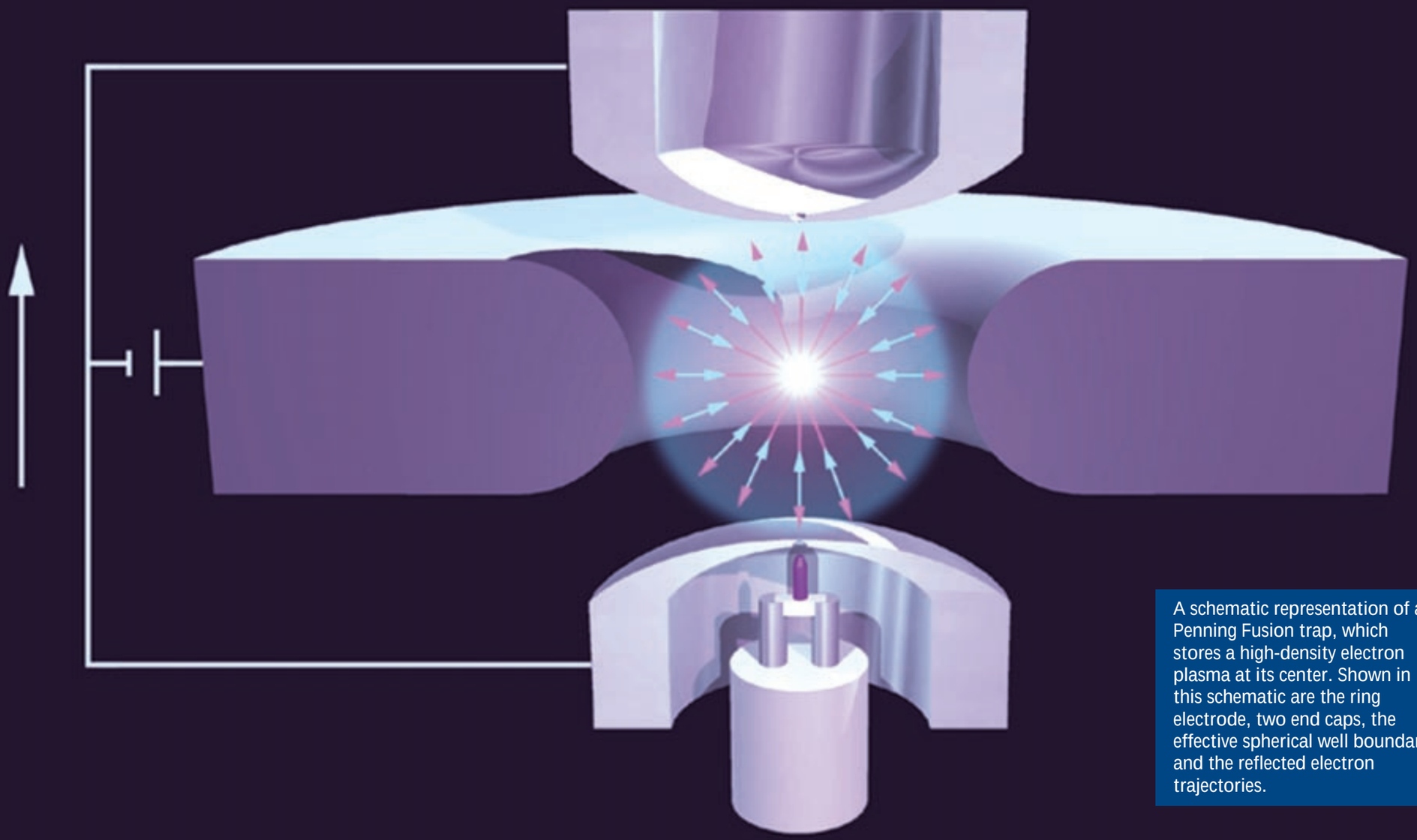

A schematic representation of a Penning Fusion trap, which stores a high-density electron plasma at its center. Shown in this schematic are the ring electrode, two end caps, the effective spherical well boundary, and the reflected electron trajectories.

Diffusion Imaging with Hyperpolarized ^{3}He

D. M. Schmidt, J. S. George (P-21),
S. I. Penttila (P-23),
A. Caprihan, E. Fukushima
(Lovelace Respiratory Research Institute, Albuquerque, New Mexico)

Several novel aspects of nuclear magnetic resonance (NMR) or magnetic resonance imaging (MRI) with hyperpolarized noble gases have recently been demonstrated, including the ability to easily image gas-filled spaces[1,2] and to transfer part of the polarization to other nuclei.[3,4] Using these new techniques, we have been investigating diffusion. We obtained one-dimensional images of ^{3}He gas diffusing in a slice that was tagged by inverting its magnetization, a technique previously used for observing the diffusion of thermally polarized ^{129}Xe gas.[5] Also, a one-dimensional diffusion image of the gas was made with and without a temperature gradient present. Our results show that temperature changes can be monitored by diffusion images of ^{3}He gas.

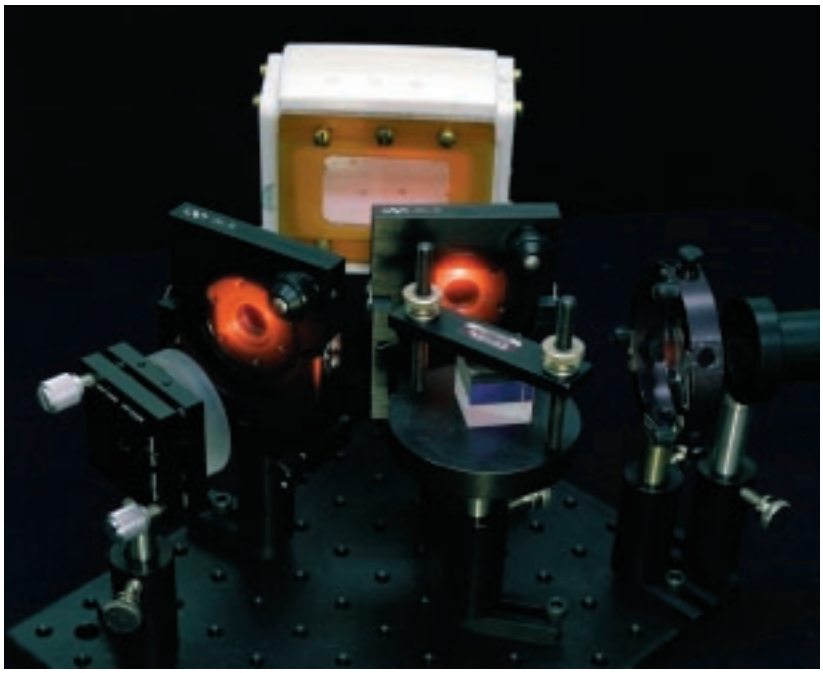

Fig. II-1. A photograph of the portable apparatus used to polarize the ^{3}He gas.

The experiments were performed in an NMR imager/spectrometer at the Lovelace Respiratory Research Institute in Albuquerque, New Mexico. Rather than thermally polarizing the ^{3}He gas in the magnetic field of the imaging magnet, we hyperpolarized the gas externally with a laser. In this technique, rubidium atoms are first polarized with circularly polarized laser light, which then polarizes the ^{3}He gas through spin-exchange collisions.[6,7] The ^{3}He gas was at 7 atm of pressure in a cylindrical glass cell with an inner length of 7.0 cm and an inner diameter of 2.2 cm. Figure II-1 shows the polarizing apparatus. For each set of images, the gas was polarized in the fringe field of the 1.9-T imaging magnet at a distance of 2 m for a few hours using a 15-W diode-laser array.[8] The polarization time constant of the cell (T1) was about 15 h, and with 4 h of optical pumping, a polarization of about 5% was achieved. This polarization is over three orders of magnitude larger than the polarization that would be obtained with conventional thermal polarization, and thus it significantly improves our ability to image the gas. A two-dimensional projection image of the hyperpolarized gas is shown in Fig. II-2.

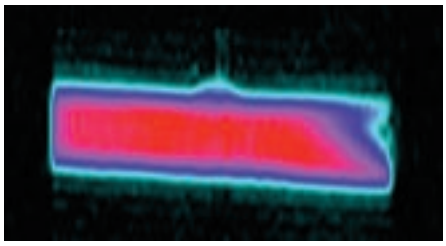

Fig. II-2. A two-dimensional projection image of the hyperpolarized ^{3}He gas in its cylindrical cell. The 1-mm stem that is used for filling the cell is visible in the top-center portion of the image.

A series of one-dimensional images over time were obtained in which the diffusion of two populations of nuclei could be seen in a manner similar to that in Ref. 5. First, the magnetization of the nuclei in a thin, central section of the cylinder was inverted. Then, images were taken every 0.2 s for a total of 5 s, using a constant flip angle of 4.5°. Because the gas had such a long T1, the fraction of the magnetization (sin[4.5°]) that was lost due to dephasing with each image acquisition did not recover over the 5-s duration of the experiment. The series of images, normalized to the same total intensity, are shown in Fig. II-3.

The ^{3}He diffusion coefficient was determined with this data using a simple model. A delta-function spike in density will, through diffusion, form a density profile that is Gaussian, with a variance proportional to the diffusion coefficient and to the time over which diffusion has taken place.[9] We therefore modeled each one-dimensional image by convolving the first image with a Gaussian distribution whose variance V was proportional to a diffusion coefficient D times the time interval t separating the two images: $V = 2Dt$. We then searched for the value of D that minimized the error between the predicted and measured values using a chi-squared statistic. This model does not account for the cell walls, so only the pixels that were sufficiently far away from the walls were used in the fit. In addition, to correct for the decreasing signal, we first normalized each image to the same total signal intensity. A comparison of the experimental data to the model with the best-fitting value of D is shown in Fig. II-4 for a few selected time intervals. A value of $D = (12.3 \pm 0.2)$ mm^2/s was obtained.

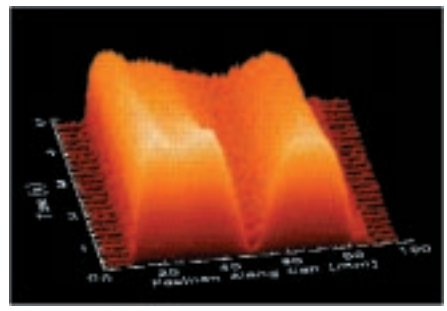

Fig. II-3. A series of one-dimensional images of the gas over time, showing the diffusion of the small central slice of inverted magnetization. Time runs from front to back, with the total duration being 5 s.

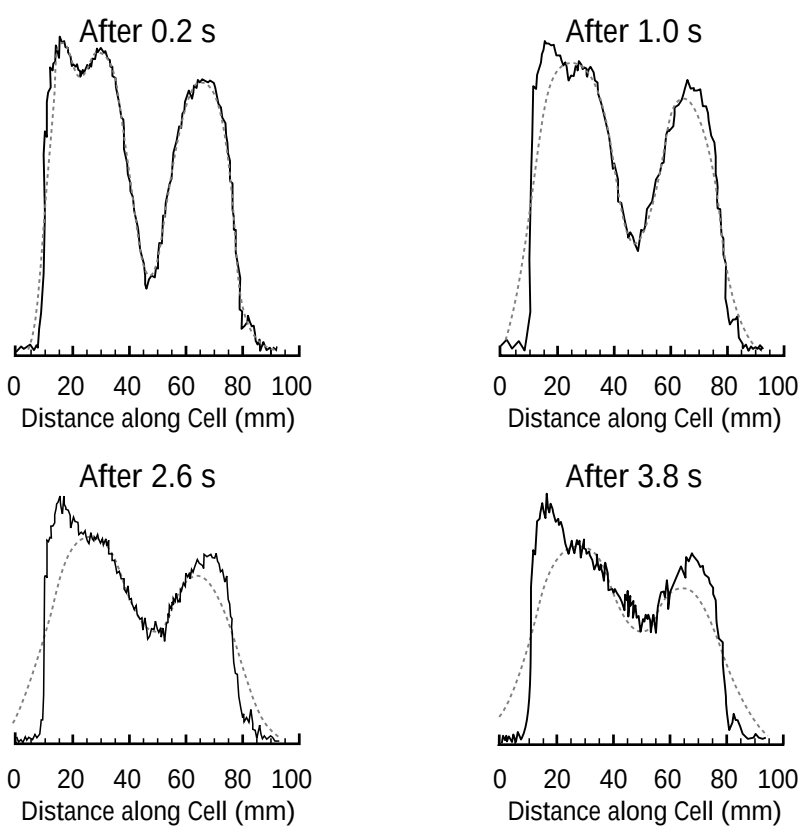

Fig. II-4. A comparison of the data (solid) and model (dashed) for a few selected time intervals using the best-fit value of the diffusion coefficient. The model does not take into account the cell boundaries; the pixels included in the fit are only those that are far enough away from the boundaries to remain unaffected by them.

Next, one-dimensional diffusion images were made using the technique of Stejskal and Tanner.[10] A diffusion coefficient was calculated at each point in the image by taking the ratio of the image intensities with and without a previous magnetic-field gradient in place. With a gradient, the signal will diminish because of diffusion. Knowing the strength and duration of the gradient allows the diffusion coefficient to be determined.

Diffusion can be affected by physical boundaries as well as by temperature or pressure. Images were made both at thermal equilibrium and with a thermal gradient (Fig. II-5). The value of every fifth pixel averaged with its four nearest neighbors is shown in these images. In the upper plot in Fig. II-5, the gas is at thermal equilibrium at room temperature. Error bars in this plot are larger than those in the lower plot because the data for the upper plot were acquired after a shorter polarization time and therefore had smaller signals. The diffusion coefficient away from the ends of the cylinder is consistent with that measured from observing the diffusion of a section of inverted magnetization (described above). The lowering of the diffusion coefficient near the walls of the cylinder is due to the walls restricting the diffusion in this area and is the cause of the edge enhancements discussed in Ref. 11. The lower plot shows a diffusion image when the cylinder had a thermal gradient produced by holding the right end (as viewed in this figure) of the cell in a liquid-nitrogen exhaust plume for a few minutes. The diffusion coefficient decreases with temperature. Again, lowering of the diffusion coefficient at the ends is due to restricted diffusion.

We have demonstrated the use of diffusion imaging with a hyperpolarized noble gas for monitoring temperature and for detecting physical boundaries. Just like relaxation-time images, spatial maps of diffusion can be a useful technique for characterizing the environment of the molecules containing the nuclei being imaged. We believe that diffusion imaging of hyperpolarized noble gases offers unique advantages in characterizing the porosity of materials, studying fractures in rocks, and dynamically imaging the pressure and temperature distributions in biological and acoustical systems.

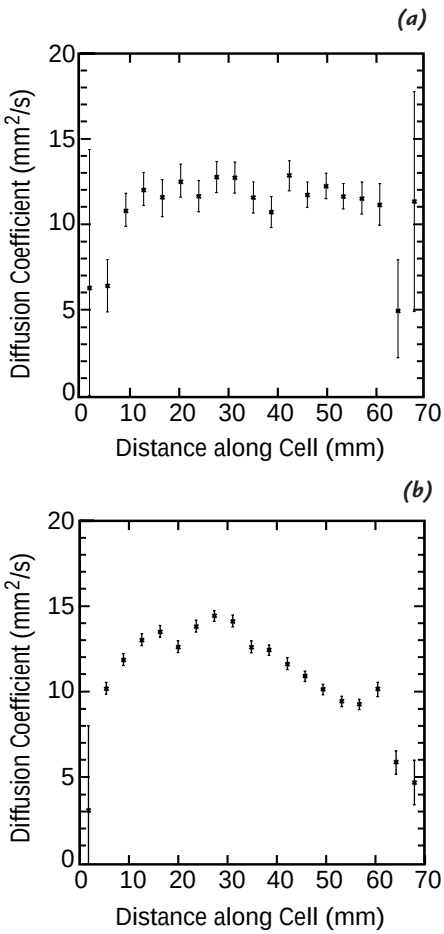

Fig. II-5. Two diffusion images (a) without and (b) with a thermal gradient in place. The reduction in the diffusion coefficient near the cell boundaries in both images is due to restricted diffusion. The decrease in diffusion from left to right in the lower image reflects the decrease in temperature from left to right.

References

1. M. S. Albert, G. D. Cates, B. Driehuys, et al., "Biological Magnetic Resonance Imaging Using Laser-Polarized ^{129}Xe," *Nature* **370**, 199 (1994).

2. H. Middleton, R. D. Black, B. Saam, et al., "MR Imaging with Hyperpolarized ^{3}He Gas," *Magnetic Resonance in Medicine* **33**, 271 (1995).

3. C. R. Bowers, H. W. Long, T. Pietrass, et al., "Cross Polarization from Laser-Polarized Solid Xenon to $^{13}CO_2$ by Low-Field Thermal Mixing," *Chemical Physics Letters* **205**, 168 (1993).

4. G. Navon, Y.-Q. Song, T. Rõõm, et al., "Enhancement of Solution NMR and MRI with Laser-Polarized Xenon," *Science* **271**, 1848 (1996).

5. M. Pfeffer and O. Lutz, "Observation of Diffusion in Xenon Gas by NMR," *Journal of Magnetic Resonance A* **113**, 108 (1995).

6. N. D. Bhaskar, W. Happer, and T. McClelland, "Efficiency of Spin Exchange between Rubidium Spins and ^{129}Xe Nuclei in a Gas," *Physical Review Letters* **49**, 25 (1982).

7. W. Happer, E. Miron, S. Schaefer, et al., "Polarization of the Nuclear Spins of Noble-Gas Atoms by Spin Exchange with Optically Pumped Alkali-Metal Atoms," *Physical Review A* **29**, 3092 (1984).

8. W. Cummings, O. Häusser, W. Lorenzon, et al., "Optical Pumping of Rb Vapor Using High-Power $Ga_{1-x}Al_xAs$ Diode Laser Arrays," *Physical Review A* **51**, 4842 (1995).

9. E. L. Cussler, *Diffusion: Mass Transfer in Fluid Systems* (Cambridge University Press, New York, 1984), p. 40.

10. E. O. Stejskal and J. E. Tanner, "Spin Diffusion Measurements: Spin Echoes in the Presence of a Time-Dependent Field Gradient," *Journal of Chemical Physics* **42**, 288 (1965).

11. P. T. Callaghan, A. Coy, et al., "Diffusive Relaxation and Edge Enhancement in NMR Microscopy," *Journal of Magnetic Resonance A* **101**, 347 (1993).

A Debris-Free Plasma Radiation Source for Extreme Ultraviolet Lithography

D. M. Oró, R. D. Fulton,
D. V. Morgan (P-22),
J. C. Goldstein, M. E. Jones (XPA),
B. C. Carlsten, J. M. Kinross-Wright,
D. C. Nguyen, S. J. Russell (LANSCE-9)

In the quest for increased performance, the microelectronics industry has been reducing the size of individual elements, also known as features, on integrated circuits by a factor of two roughly every six years. Smaller feature sizes result in reduced distance and, therefore, reduced transit time between features, allowing the integrated circuits to be driven at higher clock speeds. Also, greater feature density allows for increased functionality, permitting one chip to perform the tasks that previously required several. This year, commercial devices will become available with 0.18-μm features and with 125 million transistors on a single chip.

In the commercial production of integrated circuits, the patterns for the features are imaged onto a silicon wafer by projection photolithographic methods that use visible and ultraviolet light sources with conventional optics. It is anticipated that this technology will reach its limit at a feature size of 0.15 μm. Achieving features smaller than 0.1 μm using a commercially feasible process will demand advances in future lithography techniques such as using extreme ultraviolet (EUV) radiation in conjunction with molybdenum/silicon multilayer reflective optics. These optics have a maximum theoretical reflectivity of 76% at a wavelength of 13 nm, which is more than an order of magnitude smaller than the shortest wavelength used in today's commercial processes. Using 13-nm radiation will allow for the imprinting of features that may ultimately be smaller than 0.05 μm.

Most of the proposed EUV lithography (EUVL) sources involve the interaction of a high-energy-density source (such as a laser, an electron beam, or an arc discharge) with a solid target. Although all of these methods offer efficient production of EUV radiation, debris generated from solid targets has been demonstrated to deteriorate the very expensive, metal, multilayer system optics. From FY94 to FY96, Los Alamos and Northrop Grumman were developing a debris-free EUVL source under a cooperative research and development agreement (CRADA). This source exploits the predicted anomalous energy deposition of a short-pulse electron beam in a preformed plasma. As a result, the plasma is heated and ionized to a charge state in which efficient radiation with a wavelength of 13 nm or less is generated upon recombination. Because solid targets are avoided, the production of debris is avoided as well. The effort at Los Alamos had three distinct phases: experimental verification of the anomalous energy absorption; construction of a short-pulse, high-brightness accelerator; and the final experiments with the accelerator.

Anomalous energy deposition into a preformed target plasma by a relativistic electron bunch is predicted when the temporal duration (bunch length) is less than or equal to the inverse of the plasma frequency of the target plasma. For a bunch this short, the plasma can no longer respond to the individual electrons but instead responds collectively to the bunch. The energy loss is predicted to scale as the square of the effective charge of the bunch. For a bunch with a few nanocoulombs of charge, ~10^{10} electrons, this scaling suggests a

considerable enhancement of stopping power over that of individual electrons. The bunch loses energy by driving a large-amplitude electrostatic wave in the target plasma—that is, by generating a plasma wake field. The goal of this work is to drive the wake-field generation process into the nonlinear, wave-breaking regime so that the energy deposited into the plasma wave will efficiently heat and ionize a plasma column that will generate EUV.

Initial experiments to demonstrate anomalous energy absorption are carried out with the accelerator developed for the Los Alamos Free-Electron Laser as the source of the electron bunches. For these experiments, the accelerator is configured to produce 15-ps, 4-nC electron bunches with an energy of 15.5 MeV. The bunches are produced in a manner that accelerates a series of 1–8 bunches with a spacing of 9.2 ns between each bunch (collectively referred to as a macropulse). The macropulse is injected into a 10-cm-long gas cell containing either 0.18 or 0.5 torr of argon. As the first few electron bunches pass through the cell, a weakly ionized (~0.1% ionization) argon plasma column is created by collisional ionization. The plasma frequency, ω_{pe}, increases with increasing plasma electron density, n_e, by the relationship $\omega_{pe} \propto \sqrt{n_e}$. When the inverse of the plasma frequency equals the bunch length, T_b, or, equivalently, when a critical electron-density is reached (that is, when $n_e \cong 3 \times 10^{15}/T_b^2$ cm^{-3}, where T_b is in picoseconds), the plasma responds collectively to the next bunch and slows the bunch, transferring energy to the background plasma electrons. The heated background plasma ionizes the neutral gas. After the macropulse exits the gas cell, the energy of the individual bunches in the macropulse is measured with a time-resolved energy spectrometer. The plasma density along the ionized filament in the cell is measured with a 94-GHz microwave interferometer.

Figure II-6 shows the measured energy for each bunch with and without gas in the cell. The linear drop in energy for each succeeding bunch measured in the vacuum case is an artifact of the acceleration process. The measured bunch energies with gas in the cell show the anticipated results. The collisional losses of the first three bunches are too small to be detectable by our technique. As the ionization increases, the energy loss suddenly increases, peaks at an optimum plasma electron density, and then lessens as the density becomes too high for efficient energy loss for the fixed bunch length. Figure II-7 shows the percentage of energy loss as a function of the plasma electron density. The maximum observed energy loss is 2.2% (for 0.18 torr) and corresponds to an enhancement of 3.4×10^4 over that expected from collisional ionization and radiative losses. Also shown in Fig. II-7 is the result of numerical simulations of the anomalous energy loss. The simulations, which were performed by researchers in XPA with the particle-in-cell plasma simulation code ISIS, show good agreement with the measurements.

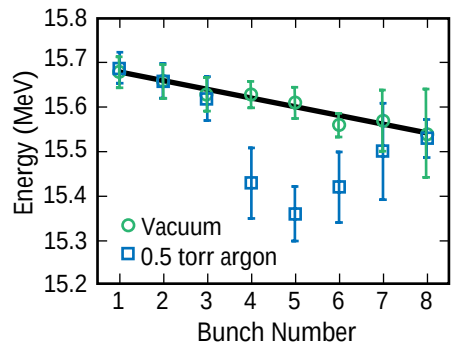

Fig. II-6. Electron energy plotted versus the number of injected electron bunches. The line is a linear fit to the energy of the bunches without a gas fill; the negative slope is an artifact of the acceleration process.

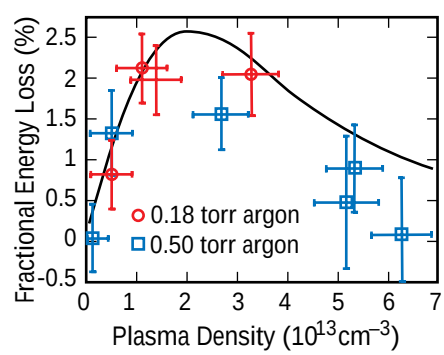

Fig. II-7. Energy loss plotted versus plasma density. The curve is the result from numerical modeling with ISIS.

Although these experiments demonstrate, for the first time, the predicted anomalous energy deposition, the amount of energy deposited is not sufficient to heat and ionize the plasma for EUV production. The fractional energy loss per unit length of a bunch is proportional to the plasma density for a bunch of optimal duration. Numerical calculations show that an 8-MeV, 1.5-nC bunch with a duration of 0.75 ps would suffer an energy loss of 80% for an interaction length of 2.5 mm in a neon plasma with an electron density of ~10^{16} cm^{-3}. Thermalization of the deposited energy results in a 10- to 20-eV plasma filament producing EUV from Ne^{4+} and Ne^{5+} ions. As part of the second phase of the CRADA, a linear accelerator (linac) that can produce bunches with these parameters has been constructed by researchers in AOT-9 (now LANSCE-9). Using photocathode technology, the linac produces 8-MeV-electron bunches with 1.5 nC of charge and an initial length of 20 ps. A time-of-flight compressor, which uses the energy spread created in the acceleration process, reduces the bunch duration to 0.75 ps with no loss of charge. The accelerator can create a macropulse of a series of bunches with a spacing of 9.2 ns. Northrop Grumman developed a pulsed, supersonic gas jet that produces a 0.4-cm × 1-cm jet of neon with a density of neutral atoms of ~10^{19} cm^{-3}. A photograph of the accelerator is shown in Fig. II-8.

As was seen in the initial experiments, it is anticipated that the first few bunches in the macropulse will create a weakly ionized plasma column in which a trailing pulse will strongly couple and deposit a significant amount of its energy. The configuration of the experiment does not permit time-resolved measurements of the individual bunch energies. The primary diagnostics are two filtered silicon photodiodes that view the interaction region. One diode is coated with layers of titanium, zirconium, and carbon that are 5 nm, 200 nm, and 50 nm

Fig. II-8. The EUVL linac located at Los Alamos. The accelerator generates 8-MeV, 1.5-nC electron bunches that are compressed to a bunch length of 0.75 ps.

thick, respectively. This layering results in a filter that has a band-pass between 6 and 16 nm (200 to 77 eV), which blocks any longer wavelengths and passes radiation shorter than 1.3 nm (950 eV). The second diode has a 127-μm beryllium layer that passes wavelengths shorter than 0.9 nm (1265 eV) and blocks all longer wavelengths. This combination of filters permits the detection of radiation between 6 and 16 nm with the Ti/Zr/C-coated diode while rejecting any signals that may be from x-rays and gamma rays because these signals would be seen in the beryllium-filtered diode.

Figure II-9 shows data from the two diodes. Distinct pulses are evident in the Ti/Zr/C-filtered diode that are absent in the beryllium-filtered diode, indicating the generation of radiation within the 6- to 16-nm band. The first pulse seen in the data is coincident with the fourth bunch of a macropulse that contains 10 bunches. The timing is confirmed by measuring the pulses recorded when a metal target is placed in the interaction region. (Using a metal target results in a gamma-ray pulse for each bunch in the macropulse; this pulse is seen in both detectors.) These results show behavior similar to that seen in the initial experiments. The first few bunches of the macropulse show negligible coupling, after which strong EUV generation occurs for the next few pulses. For these experiments, it can only be assumed that the optimum plasma electron density for this bunch length corresponds to the peak in the EUV generation. (The microwave interferometer used in the initial experiments was not used for these experiments because the plasma electron density is beyond its measurement capabilities.) From the energy absorbed by the photodiode, we estimate that on the order of 1% of the bunch's energy is converted to radiation in this band.

These experiments demonstrate debris-free EUV production using anomalous energy deposition of an electron bunch into a plasma. The technique shows promise as a source for EUVL; however, measurements of the conversion efficiency into the 13-nm (±0.15 nm) band are needed. Northrop Grumman estimates the production cost of a commercial EUV source based on this technology to be $1.5 million, an amount that is comparable to cost estimates of laser-based systems.

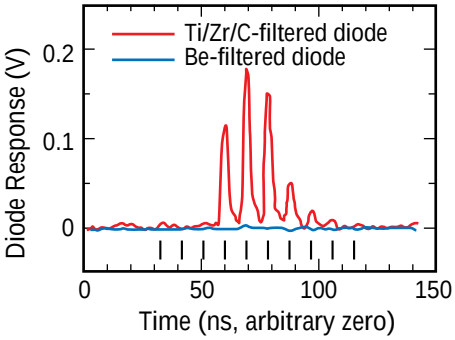

Fig. II-9. Data from the silicon photodiodes that view the interaction region. They indicate the production of EUV in the 6- to 16-nm-wavelength band. The black vertical bars mark the time that each of the 10 electron bunches from a macropulse passes through the interaction region. The data are for a single macropulse.

Pulsed-Power Experiments at the Pegasus II Facility

Collaborators from P Division, DX Division, MST Division, X Division, and Bechtel

Overview of the Facility

Pegasus II is a pulsed-power facility at Los Alamos National Laboratory that is used to conduct a variety of experiments in the high-energy-density regime that have applications to the physics of nuclear weapons as well as to basic science. The facility (Fig. II-10) consists of 144 energy-storage capacitors arranged as a two-stage Marx bank with a maximum erect voltage of 100 kV. The 4.3-MJ stored energy for this voltage makes Pegasus II one of the largest capacitor-bank facilities in the world. Pegasus II is used to produce peak currents as high as 12 MA in cylindrical inductive loads and can be operated either with or without a fast opening switch. In addition to conducting plasma- and hydrodynamic-physics experiments, researchers at the Pegasus II facility continue to address technological issues of developing an efficient switch. As a result of the destruction associated with the dissipation of the large stored energy, repair and replacement of components follow each experiment, and shots are fired approximately every two weeks. Several different experimental campaigns in support of the nuclear-weapons program are conducted and involve both heavy, solid liners and thin aluminum foils as the loads for the machine. The foil targets become plasmas during an implosion; in the foil-implosion experiments the imploding plasma stagnates on the axis of the cylindrical system, and the kinetic energy is converted to thermal energy and radiation. The solid-liner experiments are mainly used to address hydrodynamic issues and often involve the impact of the liner on an internal target package. The contact person for Pegasus II projects is Jack Shlachter of P-22.

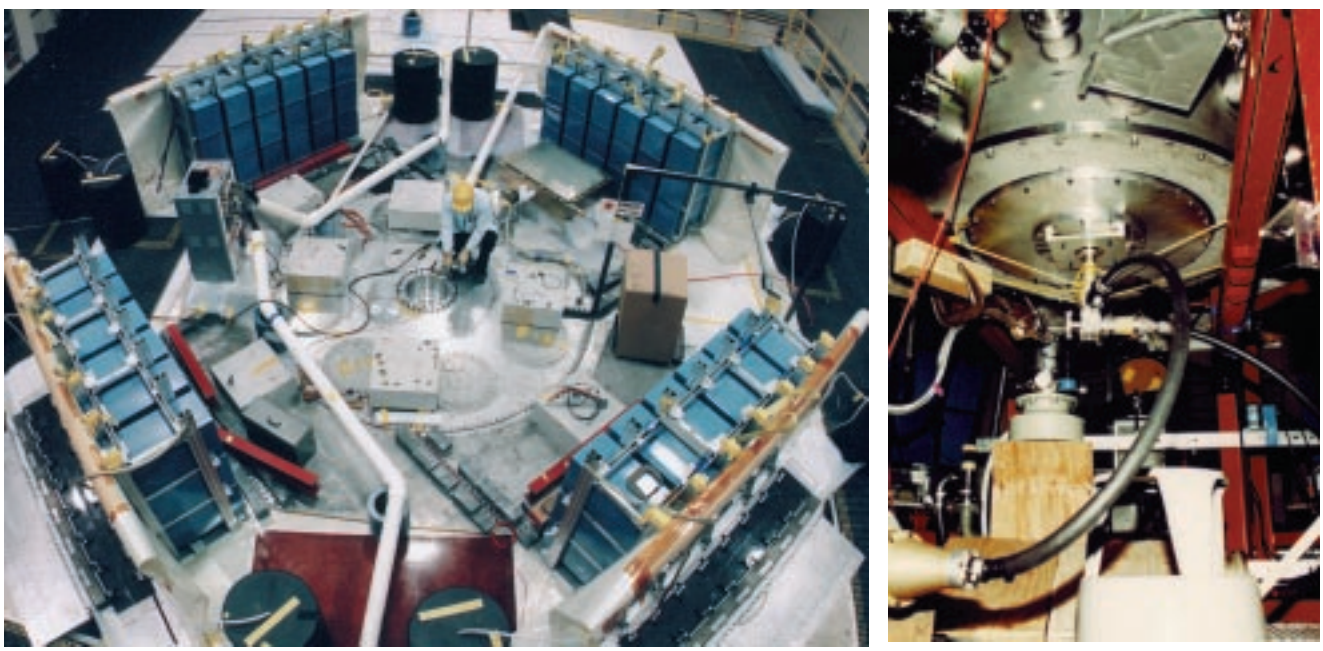

(a) *(b)*

Fig. II-10. View of (a) the upper half and (b) close-up of the target chamber in the lower half of Pegasus II.

Summary of Physics Capabilities

Research during the past two years has been focused mainly on hydrodynamic experiments that use a standardized solid drive liner. The active portion of the liner, made from unalloyed (1100 series) aluminum, is a 3.2-g right hollow cylinder (4.8-cm outer diameter, 2-cm height, and 0.4-mm wall thickness) designed to remain at solid-aluminum density during the course of the experiment. For typical Pegasus II operating conditions, the impact of this liner on an internal target with a diameter of a few centimeters results in shock pressures of 100–500 kbar with liner velocities of ~3 km/s at a peak current of 6 MA and an impact time of ~10 μs.

Ejecta Experiments

When a shock wave interacts at a solid/gas (or liquid/gas) interface, some of the solid or liquid material can be emitted into the gas region. These materials can range in size from submicron to hundreds of microns and are referred to as ejecta. The amount, size, and velocity of ejecta will depend on material properties such as the grain size and surface finish as well as the state of the shock wave in the material. This phenomenon occurs in a nuclear weapon when a shock wave interacts at the interfaces between weapon materials and the gases. At this interface, metallic ejecta can be injected into the gas, contributing to the mix of those materials with the gas, which in turn has an effect on the performance of the nuclear device.

In order to characterize and understand ejecta distributions, P Division has developed an in-line Fraunhofer holography technique to make measurements of the ejecta in dynamic systems. The diagnostic has been developed and implemented on numerous experiments based at Pegasus II. The ejecta experiments use the standard aluminum implosion cylinder with various 3.0-cm target packages inside. When the liner driver impacts a target cylinder, a shock wave is set up in the target. The shock wave then propagates through the 400-μm-thick target, and the ejecta are emitted at the target/vacuum interface. An additional 1.6-cm-diameter cylinder (collimator) with various slit openings is used to control the amount of ejecta that passes through to the axial center. The entire load assembly thus consists of three cylinders with the same axis. To make a holographic measurement of the ejecta, a 60-mJ, 100-ps, 1.5-cm-diameter laser pulse is transported along the collimator axis. The laser beam then interacts with the ejecta that have passed through the collimator slits. This interaction occurs some time after the driver-liner cylinder impacts the target cylinder. The actual hologram is made when the scattered light from the ejecta interferes with the unscattered laser light (reference beam) at the plane of the film. Measuring particles of a few microns in size requires that the holographic film be placed a few centimeters from the ejecta. However, at this distance the film would be destroyed in the experiment. To address this problem, our researchers have developed an optical transfer system that relays the interference pattern 93 cm from the ejecta to the holographic film. The hologram contains information about particles ranging from a few microns to a hundred microns in diameter over a volume of 1 cm^3.

In addition to the holography diagnostic, a visible shadowgraphy, dark-field imaging technique has also been developed. Unlike holography, this diagnostic does not provide three-dimensional information; however, it does provide spatially resolved and time-resolved data about the ejecta front as it moves through space. This diagnostic uses a long-pulsed ruby laser (a 450-μs pulse). The laser passes through the ejecta, and a framing camera makes time-dependent, spatially resolved shadowgrams of the ejecta. This technique has been applied successfully to many experiments. Ejecta data have been obtained for both aluminum and tin targets for which the target surface finish and shock strength have been varied.

Complex Hydrodynamic Experiments

Using the same standard aluminum drive cylinder on Pegasus II, our researchers have conducted a separate series of experiments to look at complex hydrodynamic problems. These experiments offer an approach to studying the vorticity and mixing of materials induced by a shock passing across a nonuniform boundary. Although the details of the target design for an individual experiment vary, one example consists of xenon gas surrounded by three layers; the inner and outer layers are made of lucite and the middle layer of gallium (Fig. II-11). The gallium layer is 2 mm thick all the way around, but one half has a smaller radius than the other half. Thus, a step is formed at the junction where these two half-cylinders meet. As the main shock passes across this nonuniform boundary, vorticity and mixing of materials are calculated to occur. We are mainly using axial x-rays to look for the calculated disruptions. Sufficiently high quality x-ray images will provide us with a code benchmark for this particular hydrodynamic phenomenon.

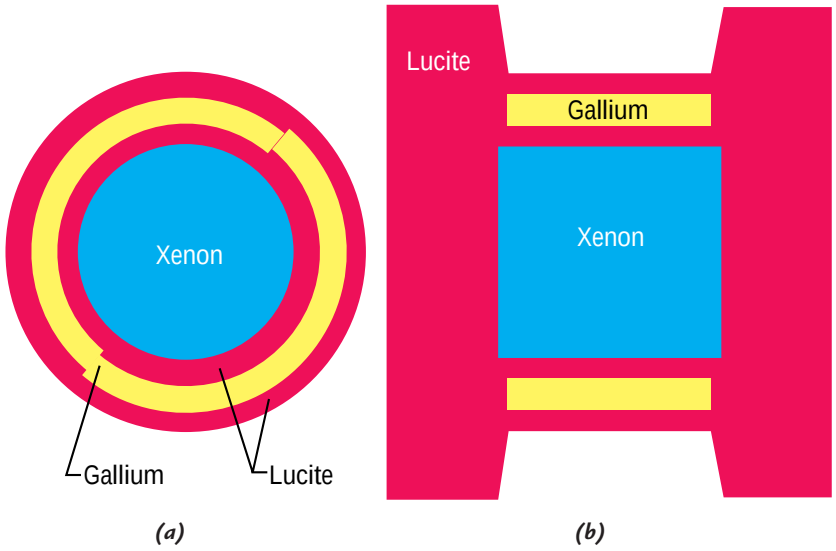

Fig. II-11. Schematic (a) end view and (b) side view of the target package for the complex hydrodynamic experiments.

Liner-Stability Experiments

A series of Pegasus II experiments examining the stability of the imploding liner at near-melt conditions has been conducted. These experiments are motivated by the desire to take full advantage of the Pegasus II facility for performing hydrodynamic studies and to anticipate conditions that will be produced on the Atlas facility that is slated for operation in 1999. Although one-dimensional calculations show that liners can be accelerated to high velocities with a significant fraction of the liner remaining in the solid state, a more detailed analysis using two-dimensional magnetohydrodynamic codes indicates that the liner may break up as a result of instabilities. To provide experimental tests of these calculations, we modify standard liners by coating the inner surface of the aluminum with a thin layer of gold to allow for detailed radial radiographic imaging. For some shots, the liner is fabricated with a precisely machined sinusoidal perturbation in the outer surface. Radiographic images provide experimental data on the observed growth rate of the perturbation as a function of spatial axial wavelength; these data can then be compared with theoretical estimates. Figure II-12 shows radiographic data from a sinusoidally perturbed liner.

Megabar Experiments

The major limitation on imploding-liner conditions is the rise in material temperature associated with the deposition, through the high current, of Ohmic heat. Experiments that require ultrahigh-pressure shock generation, greater than the ~300 kbar achieved with standard aluminum liners on Pegasus II, are of interest for weapons research as well as for basic science. One approach to producing such high pressures on Pegasus II involves the use of composite liners. These systems consist of an outer liner of aluminum with an inner layer of platinum. The aluminum constitutes the bulk of the assembly mass and carries the current. Its low density allows the assembly to achieve maximum velocity. The platinum has a high density and provides for a high shock pressure but remains solid as a result of its high melting point and its relatively low electrical conductivity. With these composite liners, it appears that multimegabar pressures can be achieved on Pegasus II; preliminary results indicate that this approach to high pressures is worth pursuing.

Fig. II-12. Static and sequential x-ray radiographic images of a sinusoidally perturbed liner during implosion.

Near-Term Plans

As the utility of Pegasus II becomes more widely recognized, new experiments and campaigns are being proposed. The present shot schedule includes experiments designed by outside users (from Lawrence Livermore National Laboratory, France, Britain, and Russia) as well as by local researchers. Emphasis for all of these experiments is

on issues associated with implosions of heavy metal liners, covering physics topics such as high material strain at high strain rates, Rayleigh-Taylor mix/demix, and laboratory production of ultrahigh magnetic fields. Initial experiments on Pegasus II designed to achieve a peak magnetic field of 6 MG will involve the compression of an axial "seed" magnetic field by the imploding liner. This flux-conservation approach is similar to that used in explosively driven experiments but has the advantages of being fielded in a laboratory environment.

Switch Development

The experiments involving heavy-liner implosions use the Pegasus II facility in a direct-drive mode. Closure of the switches on the capacitor bank couples the current directly to the load through the transmission line. The characteristic waveform for this mode has a peak current at a quarter-cycle time of several microseconds. In the opening-switch mode, the current is allowed to build up to the peak value in a parallel circuit branch and then is rapidly switched to the load. The particular opening switch selected for Pegasus II is a plasma-flow switch; development of this switch is an ongoing activity and involves detailed evaluation of the behavior of a plasma formed between the two conductors in the vacuum coaxial region near the load. Several Pegasus II experiments have been conducted to test the dependence of switch performance on the mass and configuration of the switch material. Additional experiments are being conducted on a smaller pulsed-power facility to analyze possible sources for lost current in the coaxial region. Successful development of opening switches is important for radiation-production experiments on Pegasus II and on its successor, Atlas.

Applications to Basic Science

Pegasus II has applications to a number of important basic-science areas, and the planned Atlas facility will substantially extend these capabilities. The applications extend into the areas of plasma physics, geophysics, planetary physics, astrophysics, and condensed-matter physics. These applications are based upon the capability to produce extreme conditions of pressure, density, magnetic field, and material velocity. As mentioned above, the near-term Pegasus II experiments are designed to reach magnetic fields of 6 MG. When Atlas becomes available in 3 years, axial fields approaching 20 MG should be possible. Field strengths this high can open up new areas of condensed-matter physics. At 2 MG, for example, the Zeeman splitting in materials approaches the thermal energy in a solid and substantially exceeds the magnetic-exchange energy. Thus, magnetic properties of materials should be greatly modified in fields this high. At field strengths above 10 MG, the cyclotron radius of a conduction electron in a crystal becomes less than one lattice constant, meaning that the conventional transport properties of materials are field dominated. Some potential experiments include extending present high-field experimental studies, such as magnetization of high-critical-temperature superconductors and cyclotron resonance in low-mobility materials, and moving into new experimental arenas, such as studying new conductivity mechanisms and quantum-limit phenomena in atoms.

Pegasus II also has the capability to achieve very high pressures, both through shock compression and quasi-adiabatic compressions. With Pegasus II, pressures in the megabar regime are possible. Although such conditions may also be reached using gas guns and diamond anvil cells, the pressures achievable with Atlas will significantly exceed the limits of other conventional techniques. Among problems of great interest in high-pressure research for Pegasus II and Atlas are understanding the thermal properties of the earth's core materials near the center of the earth (i.e., at pressures in the 3-Mbar range) and measuring the equation of state (EOS) of dense, strongly coupled plasmas (which is of importance in testing models of theoretical plasma physics and in benchmarking theories of the interiors of giant planets and brown-dwarf stars). Fundamental studies of material instabilities are also being made at Pegasus II and will be extended on the Atlas facility.

Atlas Capabilities

Atlas is a funded construction project to develop a 36-MJ pulsed-power driver; this energy is approximately 10 times that of Pegasus II. When charged to its full voltage of 240 kV, Atlas will deliver over 40 MA to a load in a pulse rising in about 4 μs. Atlas will provide a rich experimental environment for programmatic experiments in the high-energy-density regime and will be a platform for many basic-physics experiments. Computational studies performed on a 70-g aluminum liner (called the Atlas standard liner) indicate that implosion velocities exceeding 20 km/s will be attained with the inner surface of the liner remaining unmelted. Thus, Atlas will be a premier driver for hydrodynamics and material studies in the very-high-pressure regime. Shock pressures exceeding 30 Mbar will be possible in high-Z materials, and direct, accurate EOS experiments in this range appear feasible. This significantly exceeds the range of any direct EOS experiments conducted by conventional techniques. At these pressures, materials are heated into the multielectronvolt regime and thus will become ionized dense plasmas (e.g., for tungsten at 25 Mbar, the temperature is 8 eV). Atlas will also provide the ability to reach high densities using near-adiabatic compressions. This is important for reaching dense plasma states that cannot be achieved by shock compression. As a hydrodynamic driver, Atlas will be used to extend the high-strain-rate and instability experiments that are now being developed at Pegasus II. Atlas has many uses for basic science. Concepts now being developed for Atlas include dense-plasma properties, materials studies in 20-MG fields, and magnetized target fusion.

Quantum Information Science

R. J. Hughes, W. T. Buttler,
M. H. Holzscheiter, P. G. Kwiat,
S. K. Lamoreaux, G. L. Morgan,
C. G. Peterson, C. Simmons,
A. G. White (P-23),
G. G. Luther (P-22),
M. Schauer (P-24),
M. S. Gulley, V. Sandberg,
D. Tupa (P-25),
A. G. Petschek (P-DO),
R. Laflamme, W. H. Zurek (T-6),
D. F. V. James (T-4),
J. E. Nordholt (NIS-1),
J. M. Ettinger (NIS-8),
M. S. Neergaard (NIS-9),
E. Knill (CIC-3)

Introduction

The representation of information by classical physical quantities such as the voltage levels in a microprocessor is familiar to everyone. But over the past decade, quantum information science has been developed to describe binary information in the form of two-state quantum systems, such as photon polarization states. (A single bit of information in this form has come to be known as a "qubit.") Remarkable new capabilities in the world of information security have been predicted that make use of quantum-mechanical superpositions of information, a concept that has no counterpart in conventional information science. For example, quantum cryptography allows two parties to communicate securely even in the presence of hostile monitoring by a third party. A quantum computer would make use of logical operations between many qubits and would be able to perform many operations in parallel. Certain classically intractable problems, such as factoring large integers, could be solved efficiently on a quantum computer. We have experimental projects underway in quantum cryptography, quantum computation, and interaction-free measurement, which also takes advantage of quantum properties.

Quantum Cryptography

One of the main goals of cryptography is for two parties ("Alice" and "Bob") to render their (binary) communications unintelligible to a third party ("Eve"). This can be accomplished if Alice and Bob both possess a secret random-bit sequence, known as a cryptographic key. For example, in "one-time pad" encryption Alice adds the key to the original message, known as plaintext, and communicates the sum (ciphertext) to Bob. He is able to recover the plaintext by subtracting his key from the ciphertext, but Eve, who is assumed to have monitored the transmitted ciphertext, is unable to discern the underlying plaintext through the randomization introduced with Alice's key. So, although key material conveys no useful information itself, it is a very valuable commodity, and methods for Alice and Bob to generate key material securely are correspondingly important.

Using quantum cryptography, or, more accurately, quantum key distribution (QKD), Alice and Bob can create shared cryptographic key material whose security is assured by the laws of quantum mechanics. They first independently generate secret random-number sequences, which then undergo a bit-wise comparison that requires the preparation, transmission, and measurement of a single photon for each bit. Alice's photon-state preparations and Bob's measurements are determined by their bit values and are chosen from sets of nonorthogonal possibilities, such as linear and circular polarization. This comparison algorithm, which may be publicly known, ensures that Bob detects a photon (with some quantum-mechanically determined probability) only if he has the same bit value as Alice. They retain only the detected bits from their initial sequences. These subsets are the raw key material from which a pure key is distilled using classical error-detection

techniques. Eve can neither "tap" the key transmissions (owing to the indivisibility of a photon) nor copy them (owing to the quantum "no-cloning" theorem). Furthermore, the nonorthogonal nature of the quantum states ensures that if Eve makes her own measurements, she will be detected through the elevated error rate arising from the irreversible "collapse of the wave function" that she introduces.

QKD offers many security and ease-of-use advantages over existing key-distribution methods. Traditional key distribution using trusted couriers requires cumbersome security procedures for preparing, transporting, and handling the key before any communications can take place and may even be impractical (e.g., re-keying a satellite). In contrast, quantum keys do not even exist before the QKD transmissions are made, and a key can be generated at message-transmission time. Public-key cryptography also avoids many of the difficulties of key distribution by courier but provides only the conditional security of intractable mathematical problems, such as integer factorization. Accurate assessment of an adversary's computing power over the useful lifetime of encrypted information, which may be measured in years or even decades, is notoriously difficult: unanticipated advances in fields such as quantum computation could render public-key methods not just insecure in the future but also retroactively vulnerable. QKD could be used for real-time key generation in cryptographic applications where this long-term risk is unacceptable.

The physical systems that can support QKD transmissions determine the potential uses of quantum cryptography. We have demonstrated that QKD is possible over multikilometer optical-fiber paths: the necessary quantum coherence of the QKD transmissions persists even outside the controlled environment of a physics laboratory. At the infrared wavelengths required, germanium or indium-gallium arsenide avalanche photodiodes can be persuaded to detect single photons but at the penalty of a high noise and, hence, a high error rate. Removing these errors reduces the amount of key material and limits transmission distances to 100 km or so. (Optical amplifiers cannot be used to extend this range because they cannot replicate the nonorthogonal quantum states used in QKD.)

In our experiment we demonstrated quantum cryptography over 24 km of optical fiber that had been installed for network applications between two LANL technical areas. We have recently increased the propagation distance to 48 km; Fig. II-13 shows the system that was used in this demonstration. Our system incorporates an encryption/decryption feature that allows us to use the quantum-key material to encrypt short text messages at the sending computer and decrypt them at the receiving computer. This experiment shows that QKD could be used to generate cryptographic keys over "open" optical-fiber links between secure "islands," such as between different government agencies in the Washington, D.C., area.

In a separate experiment we are developing QKD for "free-space," line-of-sight communications, such as surface-to-aircraft. This technology could also possibly be used for the re-keying of satellites in low-earth orbits. So far, we have achieved low-error-rate transmissions over 205 m within our laboratory, but we will extend this distance to several kilometers in the near future. These new experiments will take place outdoors and will allow us to assess the daylight background and atmospheric optics issues that will impact the key rate and error rate. Quantum cryptography is likely to be the first practical application of the foundations of quantum mechanics, which illustrates the often unexpected value of basic research.

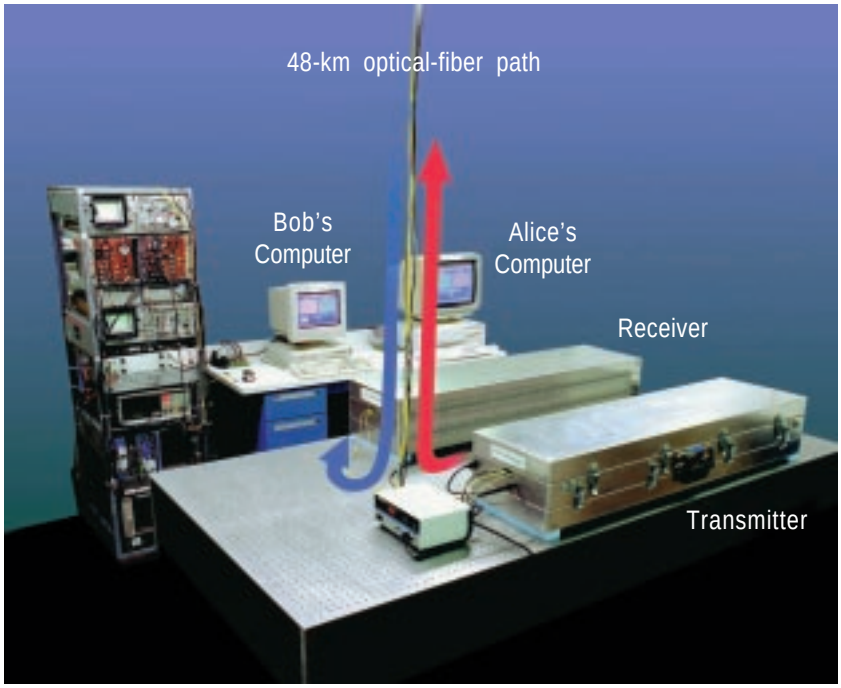

Fig. II-13. The 48-km quantum-cryptography system.

Quantum Computation

With two or more qubits it becomes possible to consider quantum logical-gate operations in which a controlled interaction between qubits produces a coherent change in the state of one qubit that is contingent upon the state of another. These gate operations are the building blocks of a quantum computer (QC), which in principle is a very much more powerful device than any classical computer because the superposition principle allows an extraordinarily large number of computations to be performed simultaneously. In 1994 it was shown that this "quantum parallelism" could be used to efficiently find the prime factors of composite integers. Integer factorization and related problems that are computationally intractable with conventional computers are the basis for the security of modern public-key cryptosystems. However, a quantum computer running at desktop PC speeds could break the keys of these cryptosystems in only seconds (as opposed to the months or years required with conventional computers). This single result has turned quantum computation from a strictly academic exercise into a subject whose practical feasibility must be urgently determined.

The architecture of a quantum computer is conceptually very similar to a conventional computer: multiqubit, or "multibit," registers are used to input data; the contents of the registers undergo logical-gate operations to effect the desired computation under the control of an algorithm; and, finally, a result must be read out as the contents of a register. The principal obstacles to constructing a practical quantum computer are (1) the difficulty of engineering the quantum states required; (2) the phenomenon of "decoherence," which is the propensity for these quantum states to lose their coherence properties through interactions with the environment; and (3) the quantum measurements required to read out the result of a quantum computation. The first proposals for practical quantum-computation hardware, based on various exotic technologies, suffered from one or more of these problems.

In 1994 it was proposed that the basic logical-gate operations of quantum computation could be experimentally implemented with laser manipulations of cold, trapped ions (Fig. II-14): a qubit would comprise the ground (S) state (representing binary 0) and a suitably chosen metastable excited (D) state (to represent binary 1) of an ion isolated from the environment by the electromagnetic fields of a linear radio-frequency quadrupole (RFQ) ion trap.

The principal components of this technology are already well developed for frequency-standard and high-precision spectroscopy work. Existing experimental data suggest that adequate coherence times are achievable, and a read-out method based on so-called "quantum jumps" has already been demonstrated with single trapped ions. We are developing an ion-trap quantum-computer experiment using calcium ions, with the ultimate objective of performing multiple gate operations (and possibly small computations) on a register of several qubits in order to determine the potential and physical limitations of this technology.

The heart of our experiment is a linear RFQ ion trap with cylindrical geometry in which strong radial confinement is provided by radio-frequency potentials applied to four "rod" electrodes and axial confinement is produced by a harmonic electrostatic potential applied by two "end caps." After laser cooling on their 397-nm S-P transition, several calcium ions will become localized along the ion trap's axis because their recoil energy (from photon emission) is less than the spacing of the ions' quantum vibrational energy levels in the axial confining potential. Although localized to distances much smaller than the wavelength of the cooling radiation, the ions nevertheless undergo small amplitude oscillations, and the lowest frequency mode is the axial center of mass (CM) motion in which all the ions oscillate in phase along the trap axis. The frequency of this mode, whose quantum states will provide a computational "bus," is set by the axial potential. The inter-ion spacing is determined by the equilibrium between this axial potential, which tends to push the ions together, and the ions' mutual Coulomb repulsion. For example, with a 200-kHz axial CM frequency, the inter-ion spacing is on the order of 30 μm.

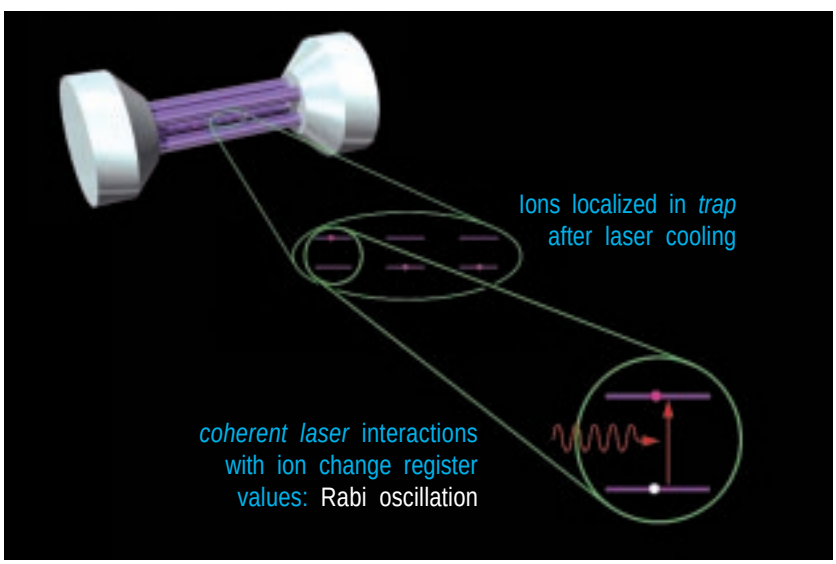

Fig. II-14. A schematic representation of the ion traps and logical gates created by laser-manipulated ions in quantum computation.

Because of its long radiative lifetime (~1 s), the S-D transition has such a narrow width that it develops upper and lower sidebands separated from the central frequency by the CM frequency. With a laser that has a suitably narrow linewidth and is tuned to the lower sideband, an additional stage of laser cooling is used to prepare the "bus" qubit (CM vibrational mode) in its lowest quantum state ("sideband cooling"). On completion of this stage, the QC is prepared with all qubits in the $|0\rangle$ state, ready for quantum computation.

The narrow-linewidth laser tuned to the S-D transition is the essential tool for changing the contents of the quantum register of ions and performing quantum logical-gate operations. By directing this laser at an individual ion for a prescribed time, we will be able to coherently change the value of the qubit that the ion represents through the phenomenon of Rabi oscillations. An arbitrary logical operation can be constructed from a small set of elementary quantum gates, such as the so-called "controlled-NOT" operation, in which the state of one qubit is flipped if a second qubit is in the "1" state but left unchanged if the second qubit is in the "0" state. This gate operation can be effected with three laser operations, using quantum states of the ion's CM motion as a computational bus to convey quantum information from one ion to the other. The result of the quantum computation can be read out by turning on the S-P laser. An ion in the "0" state will fluoresce, whereas an ion in the "1" state will remain dark. So, by observing which ions fluoresce and which are dark, a value can be obtained. We have recently succeeded in trapping calcium ions in our ion trap and imaging them with a charge-coupled device (CCD) camera. This is the first step toward creation of a quantum register.

We have also studied the intrinsic computational potential of ion-trap QCs. By taking into account the relevant decoherence mechanisms, we have found that on the order of one million gate operations could be performed on registers of 50 or so ions. This is a tremendous amount of quantum computation relative to the current state of the art: one logic operation on two qubits. Furthermore, because a QC can create an arbitrary quantum state using quantum logic operations, this computational capacity opens up a wide variety of quantum-mechanics experiments in domains that are today computationally inaccessible. We expect therefore that ion-trap QCs will allow us to explore quantum computation and the foundations of quantum mechanics.

Interaction-Free Measurement

Another area of great interest in the study of the role of quantum mechanics in information is that of "interaction-free measurements," in which the existence of nontransmitting objects (absorbers or scatterers) can be ascertained with arbitrarily small absorption/scattering taking place. In the simplest scheme, an interferometer is tuned for complete destructive interference for one of the output ports. The presence of an object in one of the arms removes the possibility of interference, so that a detector in the "dark" output port now has a chance of detecting an incident photon, which was not possible in the absence of the object. By varying the reflectivity of the inteferometer beam splitters, up to 50% of the measurements can be made interaction-free, as has been demonstrated in our lab.

More amazing, the fraction of interaction-free measurements can actually be made arbitrarily close to 1 by using a repeated interogation scheme—an application of the "Quantum Zeno" effect. In this case, there is an arbitarily small chance that any photons are absorbed by the object, and yet one gains definite information about its presence because the object inhibits an otherwise coherent evolution of the interrogating photon. For example, using simple optical elements, the polarization state of the photon can be made to rotate in small, equal steps from horizontal to vertical. However, the presence of an object that absorbs only the vertical component of the polarization at each stage will inhibit this rotation by collapsing the photon's wave function at each step back into the initial horizontal polarization. The total probability that the photon is ever actually absorbed can be made arbitrarily small by using many steps. Thus, without the object, the final state of polarization is vertical, but with the object present, the polarization becomes "trapped" in the horizontal. Paradoxically, it is the very presence of the absorbing object that alters the quantum state of the interrogating particle, ensuring that it is only rarely absorbed.

At LANL (in collaboration with researchers from the University of Innsbruck), we have achieved measurements that are up to 85% interaction free, which is the first demonstration to break the 50% limit. Efficiencies in excess of 95% are now being sought using a fast switching system. Also, we have begun investigating the practical implementation of interaction-free imaging, in which the techniques would be used to take a pixellated image of an object, again with the goal of negligible absorption or scattering. To date a resolution of less than 10 μm has been achieved in a simple, one-dimensional system looking at objects such as thin wires, optical fibers, and hairs. Finally, one of the most exciting prospects is the ability to couple to a quantum object, such as a single atom or ion, which can be in a superposition state. Using the techniques of interaction-free measurements, the quantum state can be transferred to the interrogating light, allowing the production of macroscopic entangled states of light and Schrödinger-cat states.

Please see the tutorial at http://p23.lanl.gov/Quantum/kwiat/ifm-folder/ifmtext.html for more information.

Stockpile Stewardship and Nuclear Science with GEANIE at LANSCE/WNR

R. O. Nelson, G. D. Johns, G. Chaparro (LANSCE-3),
W. S. Wilburn, D. M. Drake (P-23),
M. B. Chadwick, P. G. Young (T-2),
D. E. Archer, J. A. Becker,
L. A. Bernstein, W. Younes (Lawrence Livermore National Laboratory),
S. W. Yates (University of Kentucky)

GEANIE (for Germanium Array for Neutron-Induced Excitations) is a large, escape-suppressed germanium detector array in the Weapons Neutron Research (WNR) facility at the Los Alamos Neutron Science Center (LANSCE). The use of GEANIE with the intense, pulsed, white source of neutrons at LANSCE/WNR[1] provides new and powerful capabilities for Science-Based Stockpile Stewardship (SBSS) and nuclear science. The acquisition, installation, operation, and use of the array is a major collaborative effort between researchers from Lawrence Livermore National Laboratory and Los Alamos National Laboratory. The primary goal of the collaboration is to determine the ^{239}Pu(n,2n) cross section to an accuracy of ±10%. Other important nuclear data needs are also being addressed. The unique combination of a high-resolution gamma-ray (γ-ray) spectrometer with a high-energy neutron source provides exciting opportunities in nuclear physics as well.

Advances in the technology of germanium-detector fabrication and in accelerator technology have enabled major advances in nuclear physics. In the past, these improvements have focused on nuclear-structure physics with large arrays of escape-suppressed germanium detectors used at accelerator facilities with heavy-ion beams. The important characteristics of such arrays for nuclear spectroscopy are high energy resolution (1/1000), good efficiency, escape suppression for background reduction, and high granularity. Perhaps the best known physics from these arrays is the discovery of superdeformed bands.[2,3]

The development and use of GEANIE at LANSCE/WNR creates a powerful new tool for SBSS. The use of a spallation neutron source makes it possible to simultaneously measure excitation functions over a wide energy range. At full power, the WNR spallation source is the most intense high-energy neutron source in the world. This is the first time that a large γ-ray detector array has been used at a neutron spallation source. This unique combination opens up new possibilities for research in areas of nuclear excitation that previously have been difficult to access.

Measuring characteristic γ rays that follow neutron-induced reactions usually allows the determination of both the reaction channel—for example, (n,2n) or (n,3n)—and the particular level excited in the product nucleus. In addition, the reaction thresholds and cross-section peaks observed in excitation functions provide valuable information for the identification and study of the various reaction products. Because of the high neutron energies available, many different reactions are possible. A short list includes the following: (n,$n'\gamma$), (n,$xn\gamma$) [where x = 2, 3, 4, . . .], (n,$p\gamma$), (n,$np\gamma$), (n,$a\gamma$), and (n,$na\gamma$).

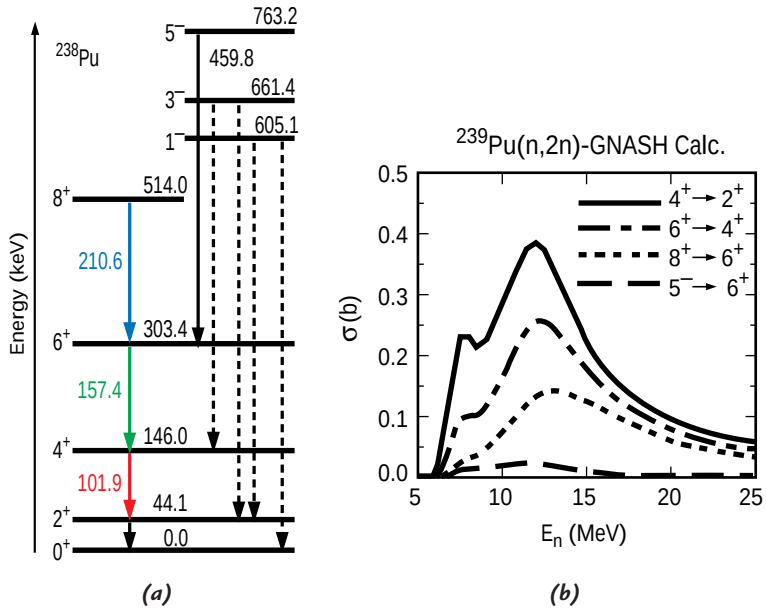

Fig. II-15. (a) Level scheme showing the ground-state rotational band and negative parity band in ^{238}Pu. (b) The GNASH-calculated values of the cross sections of these lines as a function of neutron energy.

An accurate measurement of the ^{239}Pu(n,2n)^{238}Pu reaction cross section is needed to better understand the radiochemical data from past Nevada Test Site experiments. From measured γ-ray production cross sections, we obtain an estimate of total reaction cross sections as a function of incident neutron energy. By combining our results with calculations from the coupled preequilibrium and Hauser-Feshbach computer program GNASH,[4] we can use theory to account for the fraction of the cross section that is not measured with our technique. Figure II-15 shows GNASH values for the excitation functions of some of the γ rays in ^{238}Pu resulting from the ^{239}Pu(n,2n) reaction. In Fig. II-16 we show the GNASH-predicted cross-section ratios of (n,2$n\gamma$) to (n,2n) for some of the stronger transitions. The ability to simultaneously measure excitation functions for many γ-ray transitions provides numerous checks for validation of the data and of the models used in the GNASH code.

Because a large fraction of the γ-ray cascade populates the lowest-lying states in the product nucleus, the cross sections for the decay of the low-lying states provide the best measure of the total reaction cross section. A limitation of this technique occurs for very low energy states, such as the first excited state in ^{238}Pu at 44 keV above the ground state. Very-low-energy γ-rays are highly internally converted (emitting an electron) as well as being highly attenuated in the sample, making these transitions difficult to observe. This technique of determining the reaction cross section from the partial γ-ray cross section can be used for $E_\gamma > 100$ keV. It provides a means to study nuclei via (n,xn) reactions (where x = 1, 2, 3, . . .), probing nuclei that are otherwise difficult to access. Our previous experiments[5] with a single unsuppressed germanium detector, in which we observed reactions on ^{208}Pb up to (n,9n), laid much of the

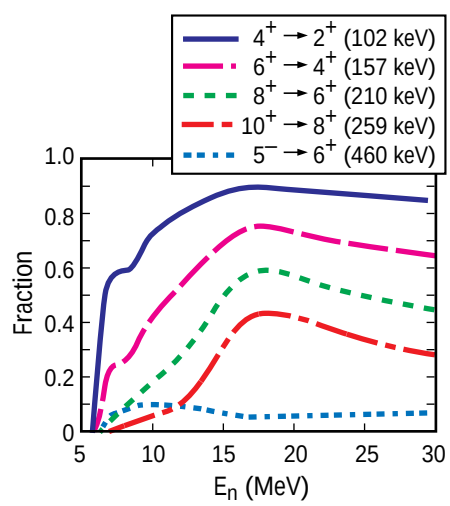

Fig. II-16. Cross-section ratios from GNASH calculated values. The 4$^+$-to-2$^+$ transition has over 70% of the total reaction cross section for E_n > 10 MeV.

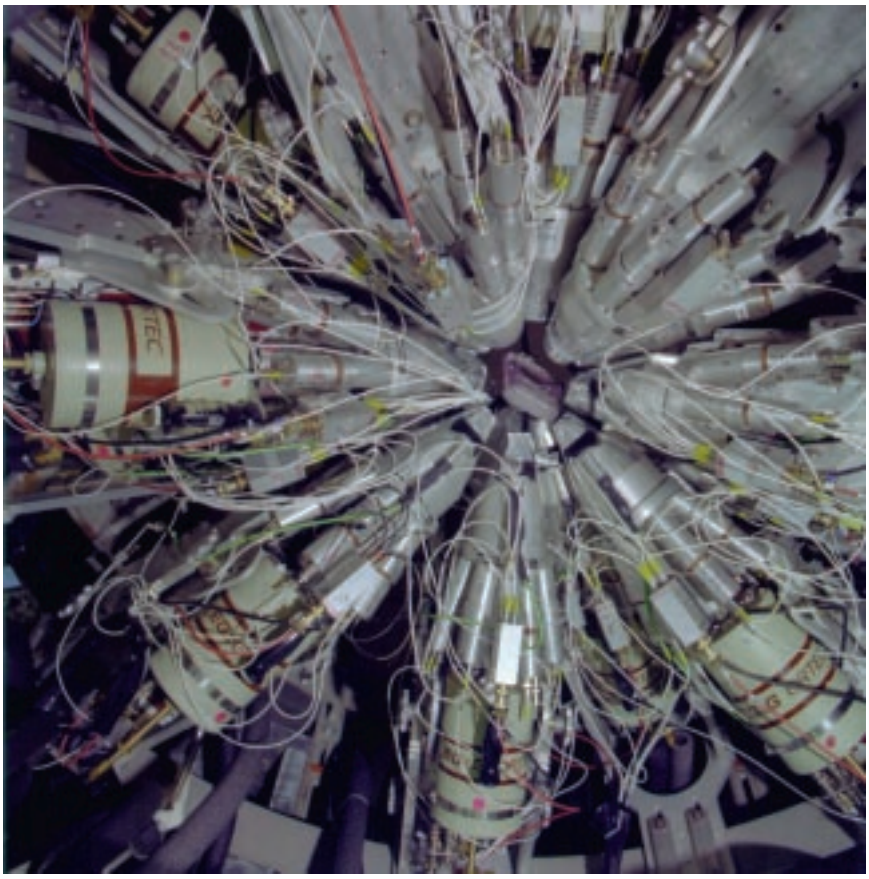

Fig. II-17. Photograph of GEANIE.

groundwork for applying this technique to actinides. The innovation of using planar germanium detectors was important for successful actinide studies, too.

GEANIE presently consists of 20 bismuth germanate (BGO) escape-suppression shields surrounding 20 germanium detectors. Figure II-17 is a photograph of the detector array. GEANIE was built using elements of the High-Energy-Resolution Array (HERA),[6] which was developed by the Nuclear Structure group at Lawrence Berkeley National Laboratory. GEANIE is located 20 m from the production target on a neutron flight path that is 60° to the incident proton beam.

Of the 20 escape-suppressed germanium detectors, 7 have planar geometry and the remaining 13 are coaxial. The coaxial detectors are 25% efficient relative to a 3-in. × 3-in. NaI(Tl) detector. The BGO escape-suppression shields improve the peak-to-total ratio for the coaxial detectors from ~0.15 to ~0.45 for a 1.33-MeV γ ray. All of the germanium detectors are interchangeable within the suppression shields, and the efficiency of the array is on the order of 1% for the full absorption peak of a 1.33-MeV γ ray. Short-term plans call for adding six more unsuppressed germanium detectors to the array. The long-term goal is to operate the array with a total of 30 suppressed germanium detectors, 10 planar and 20 coaxial.

Timing and energy resolution are equally important in our experiments. The timing resolution of the germanium detectors is important because we use it to deduce the incident neutron energy based on the time of flight. Optimal energy resolution is always important in resolving closely spaced γ rays, but this is particularly true for experiments with actinide samples that have closely spaced nuclear levels and numerous γ-decay transitions. The planar germanium detectors produce higher timing and energy resolution than the coaxial detectors, and the planar detectors also have lower background rates from the scattered neutrons because of their thin geometry. The limitation of the planar detectors is their reduced efficiency at higher γ-ray energies. A combination of both coaxial and planar germanium detectors provides a powerful spectrometer for a wide range of experiments. The useful energy range for the coaxial germanium detectors extends from ~50 keV to over 5 MeV. The corresponding range for the planar detectors is from ~30 keV to over 500 keV.

The data that we acquired include single γ-ray events as well as γ-γ coincidences. Both types of data can be used to deduce cross sections, and the coincidence data permit more detailed spectroscopy to be undertaken. The coincidence data enable background reduction that helps in observing less intense γ-ray lines. Our data-acquisition system is based on the 4π array system at Michigan State University.

The use of γ rays is an important tool for (n,xn) measurements on actinide nuclei because the production of neutrons from fission interferes with a direct measurement of the (n,xn) neutrons. The good peak-to-total ratio of the GEANIE detectors allows the resolution of individual γ-ray lines above the background from fission and other γ rays. The planar detectors play an especially important role in these measurements because they have excellent energy resolution and are relatively insensitive to neutrons. This is the first time that multiple planar germanium detectors have been used to study actinide nuclei. Figure II-18 shows a planar detector spectrum from a ^{238}U sample. The uranium x-rays and the first 4^+-to-2^+ excited-state γ-ray transition are clearly visible. The observation of this low-energy transition makes possible an accurate measurement of the $(n,2n)$ cross section.

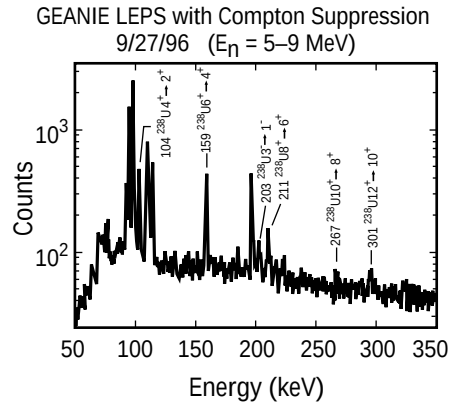

Fig. II-18. Spectrum from planar germanium detectors showing the 4^+-to-2^+ transition located between large x-ray peaks. Gamma rays from higher-lying levels are indicated as well. These data are for neutron energies between 5 and 9 MeV.

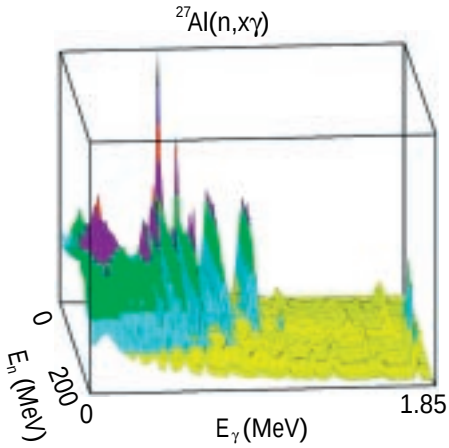

(a)

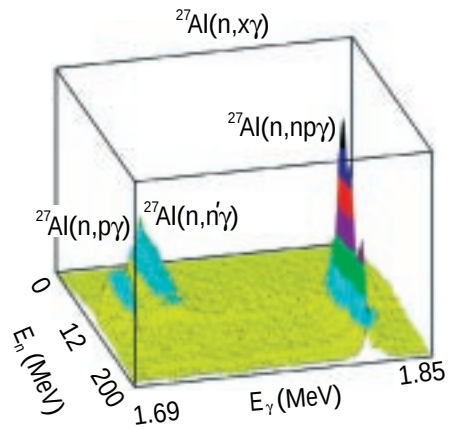

(b)

Fig. II-19. (a) Gamma-ray data from ^{27}Al(n,xγ). The "ridges" are yields from various γ-ray transitions. (b) Detail of part of the data in (a) showing peaks from three different reactions, inelastic scattering, (n,pγ), and (n,npγ).

We designed special ^{239}Pu samples encapsulated in a frame with thin beryllium windows to allow good low-energy γ-ray transmission. The design, fabrication, and use of these samples required a major effort. Using these samples, we have acquired data and observed the 6^+-to-4^+ and other transitions in ^{238}Pu. The radioactive decay of the plutonium makes data acquisition and background reduction challenging. The initial data reduction has been started, and further data will be acquired during the LANSCE accelerator operating period in 1997.

GEANIE at WNR offers an opportunity for complete spectroscopy in regions of angular momentum and excitation that are inaccessible with other neutron sources or with charged-particle beams. Such studies allow detailed tests of nuclear-structure models and level-density parameterizations. Neutron inelastic scattering is expected to be an especially valuable reaction for complete spectroscopy because it tends to populate all levels within the constraints of the angular momentum imparted to the nucleus. Data taken with an ^{27}Al sample that were collected in a brief run in November 1996 show the power of GEANIE/WNR to investigate nuclear excitations. A three-dimensional spectrum from the ^{27}Al($n,x\gamma$) single-event data is shown in Fig. II-19. Gamma rays produced by neutrons with energies from 1 to 200 MeV can be seen as ridges in part (a) of Fig. II-19. This plot shows one-half of the γ-ray energy range measured in the experiment. Part (b) of Fig. II-19 shows a small section of the data from part (a). In this region, γ-rays from ($n,n'\gamma$), ($n,p\gamma$), and ($n,np\gamma$) reactions are visible. The incident neutron energies at which these reactions are energetically allowed are all different, as can be seen by the different points along the E_n axis at which the "ridges" first occur.

From a brief run on a ^{196}Pt target we observed the ^{196}Pt(n,15$n\gamma$) reaction. This is the highest neutron multiplicity we have seen yet and demonstrates the potential for reaching neutron-deficient nuclei.

A sampling of the physics that will be pursued at GEANIE is contained in the objectives of proposals submitted to the December 1996 LANSCE Program Advisory Committee. The proposals included a search for rigid triaxial motion, an investigation of single-particle vibrational interactions in rare-earth nuclei, level-density studies, an exploration of exotic neutron-deficient nuclei, a verification of the double octupole phonon in ^{208}Pb, a search for intermediate states in ^{180}Ta to explain its cosmic abundance, and a study of the level statistics in ^{27}Al. Another proposal is to measure the Lu(n,xn) reaction cross sections for use as a diagnostic in experiments related to Accelerator Production of Tritium (APT). Off-line experiments with GEANIE are planned for times when the accelerator is not in operation. GEANIE is an important asset for stockpile stewardship and is attracting outstanding researchers because of the research opportunities available.

References

1. P. W. Lisowski, C. D. Bowman, et al., "The Los Alamos National Laboratory Spallation Neutron Sources," *Nuclear Science and Engineering* 106, 208 (1990).

2. P. J. Twin et al., "Observation of a Discrete-Line Super-deformed Band up to in ^{152}Dy," *Physical Review Letters* 57, 811 (1986).

3. B. Singh, R. B. Firestone, and S. Y. F. Chu, "Table of Super-deformed Nuclear Bands and Fission Isomers," Lawrence Berkeley National Laboratory report LBL-38004 (January 1996).

4. P. G. Young, E. D. Arthur, and M. B. Chadwick, "Comprehensive Nuclear Model Calculations: Introduction to the Theory and Use of the GNASH Code," Los Alamos National Laboratory report LA-12343-MS (July 1992).

5. H. Vonach et al., "^{207,208}Pb($n,xn\gamma$) Reactions for Neutron Energies from 3 to 200 MeV," *Physical Review C* 50, 1952 (1994).

6. F. S. Stephens, "Spectroscopy of the Highest-Spin States," *Proceedings of the International Symposium on In-Beam Nuclear Spectroscopy* (Debrecen, Hungary, May 14–18, 1984), Akadémiai Kiadó, Budapest, p. 205 (1984).

Measurements of Stimulated-Raman-Scattering Instability Relevant to Ignition Hohlraum Plasmas

J. C. Fernández, B. S. Bauer, J. A. Cobble, G. A. Kyrala, D. S. Montgomery, R. G. Watt, M. D. Wilke (P-24), W. M. Wood (P-22), D. F. DuBois, H. A. Rose (T-13), H. X. Vu (XPA), B. H. Wilde (XTA), B. H. Failor (Physics International, San Leandro, California), R. Kirkwood, B. J. MacGowan (Lawrence Livermore National Laboratory)

Introduction

Control of laser-plasma instability is important for the success of laser fusion,[1] particularly indirect drive.[2] For indirect drive, laser beams enter a cavity (called a hohlraum) made of a material that has a high atomic number and that reaches a high ionization state (high Z). The high-Z plasma efficiently converts laser energy into x-rays, which in turn drive the implosion of a fusion capsule. Ignition hohlraums, such as those planned for the National Ignition Facility (NIF),[2] are expected to contain underdense plasmas (a few millimeters in size) with electron temperatures (T_e) in the kiloelectronvolt range. Present NIF hohlraum designs rely on the plasma pressure from a helium-hydrogen gas fill to tamp intrusion into the hohlraum volume by the gold-wall plasma, while allowing laser propagation inside the hohlraum.[3] Thus, the longest scale lengths are expected to be within the low-Z helium-hydrogen plasma.

Because scientists lack a fundamental understanding of many aspects of laser-plasma instabilities, it is desirable to study these instabilities in plasma conditions that are as close as possible to those expected in NIF hohlraums. Radiation-hydrodynamic simulations of NIF hohlraums[4] with the LASNEX code[5] (an inertial confinement fusion [ICF] design code) indicate that a variety of plasma conditions will exist within the NIF hohlraum. Not all of these conditions can be studied. Both inspection and postprocessing of LASNEX simulations of NIF hohlraums[6] show that it is clearly worth considering the millimeter-scale plasmas, with low Z, $n_e / n_c \approx 0.1$, and $T_e \approx 3$–5 keV expected in NIF-hohlraum plasmas (n_e is the electron density and n_c is the critical density above which the laser's light cannot propagate). Present lasers cannot reproduce all of the required conditions simultaneously, but they can approach the conditions so that useful data can be obtained.

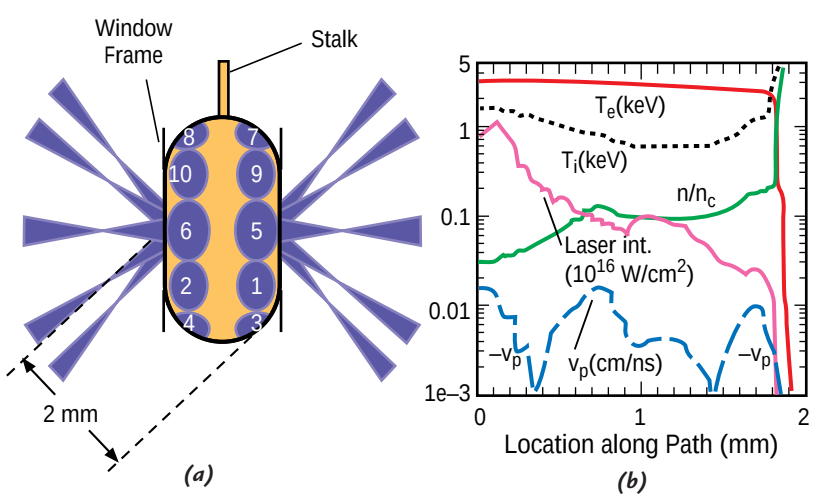

Fig. II-20. (a) An illustration of the gas-filled hohlraum. The footprints of the 10 Nova beams incident on the inner wall are indicated; those on the far wall have a dashed outline. (b) Calculated profiles within the hohlraum along a beam path (starting at the laser entrance hole) are plotted for a time of 1 ns.

Plasma Conditions

In this article we discuss the results obtained with toroidally shaped hohlraums,[7,8] which approach NIF conditions when illuminated with the Nova laser at Lawrence Livermore National Laboratory.[9] These targets were designed by X Division and fabricated by MST Division, and the experiments were fielded by P-Division scientists at Los Alamos. An illustration of the hohlraum is shown in Fig. II-20, reproduced from Fig. 1 of Ref. 7. It is cylindrically symmetric with a length of 1.6 mm and a diameter of 3.2 mm. All 10 laser beams operate at a wavelength of 351 nm. In the toroidal hohlraum we have used various gas fills, contained by thin, 0.3-μm-thick silicon nitride windows covering the laser entrance hole (LEH). Typical fills are low-Z gases such as C_5H_{12}, C_5D_{12}, CF_4, and $CF_4 + C_5H_{12}$ mixtures at 1 atm of pressure, designed to fully ionize to $n_e / n_c = 0.11$. They span the range $Z_{eff} = 2.5$–8. The calculated spatial profiles of n_e, T_e, T_i, and plasma-flow speed (v_p) along the direction of laser propagation ($\hat{k}_0$) for C_5H_{12} are also shown in Fig. II-20. For C_5H_{12}, $T_e = 3$ keV has been measured,[7,8] which is in agreement with LASNEX simulations. From Fig. II-20, the scale lengths for density, $L_n \equiv n_e / (\hat{k}_0 \cdot \nabla n_e)$, and velocity, $L_v \equiv c_s / (\hat{k}_0 \cdot \nabla v_p)$ are similar ($L_n \approx L_v \gtrsim 1$–2 mm). In the latter definition c_s is the ion-acoustic speed.

Laser-Plasma Instability

In the long-scale NIF plasmas, high levels of laser-plasma instability are predicted by linear convective theory.[10] Stimulated Raman scattering (SRS)[11] and stimulated Brillouin scattering (SBS),[12] in particular, could be significant. SRS and SBS involve scattering of laser light by electron-plasma (Langmuir) waves and ion-acoustic waves, respectively. From the initial noise level, these unstable waves would develop a growing amplitude in space. The backscattering direction is expected to have the highest spatial gain. The calculated gains from linear theory, even assuming smooth laser beams, are generally enormous (exp[25]–exp[30]) in plasmas such as ours,[6] and nonlinear saturation mechanisms are expected to occur. The high-energy glass-laser beams used for ICF are not spatially uniform. They have a broad distribution of intensities about the average value. Without any beam modification, these nonuniformities appear mostly as relatively large scale spatial fluctuations, with dimensions nonnegligible relative to the beam diameter.[13] Spatial smoothing can be accomplished with a binary random-phase plate (RPP),[14] which breaks the raw beam into smaller beamlets with a random 0 or π phase delay. RPPs produce a spatially "smooth" focal spot envelope with a superimposed fine-scale speckle (or "hot spot") pattern. The statistics of RPP hot spots are well known,[15] and it is clear that a significant fraction of the beam energy is tied up in hot spots. The known RPP hot-spot statistics allow better theoretical modeling of SBS and SRS in real plasmas, which recently has been successfully done by T-Division scientists.

SRS Onsets

We have verified that laser hot spots change the character of SBS and SRS instability onsets relative to theoretical predictions for smooth beams. With smooth beams, convective amplification of thermal density fluctuations would yield an SRS reflectivity that depends exponentially on laser intensity and L_n (≈ plasma size). But in the fluid model in Ref. 16, which is applicable to SBS and SRS in NIF conditions, instability gain on hot spots is computed including effects such as beam diffraction and pump depletion. Including diffraction is important because it can significantly decrease the spatial gain within a hot spot when the beam *f*-number is moderately small.[16,17] When the results are integrated over the RPP hot-spot distribution, the system becomes nonlinear and exhibits critical behavior. To understand the implications of the model in Ref. 16, one may consider a plasma with a sufficiently long L_n or L_v and a given seed or noise level of electrostatic waves (acoustic for SBS, Langmuir for SRS) that are sufficiently damped. We define the amount of laser light backscattered by such a seed in terms of its reflectivity R_{seed}. As the averaged intensity I of the beam envelope is increased starting from a value below the onset of instability, the laser reflectivity R sharply increases from R_{seed} once a critical intensity I_c is exceeded. The critical intensity is given approximately by the value of I, at which the linear convective gain ($R/R_{seed} = \exp[G]$) is approximately e^1 over the typical length of a hot spot, $l_{hs} \approx 7f^2\lambda$. This stands in contrast to the value $G = 2\pi$ of the gain exponent customarily taken as the threshold for significant convective instability. According to the model, even if we start with the minimum seed given by thermal density fluctuations (typically $R_{seed} \approx 10^{-8}$), once I increases moderately beyond I_c, then most hot spots undergo pump depletion (all the light is scattered) and R levels off.

We have investigated SRS onsets by varying I and measuring the SRS reflectivity from toroidal hohlraums filled with 1 atm of C_5H_{12}.[18] Figure II-21 shows the results. As with SBS, as I increases above a value I_c (about 10^{14} W/cm^2 in this case), the SRS reflectivity rises steeply and saturates at about 20%. Figure II-21 includes a fit to the data using the model in Ref. 16. The observed value of I_c for SRS is consistent with our best theoretical estimate.

The concept of a critical intensity for parametric instability seems to be fairly robust in long-scale plasmas. The critical intensity for SBS also has been measured both in the Nova toroidal hohlraums[7] and in Trident open plasmas.[20] The magnitude of I_c for SBS is predicted by the model in Ref. 16 to a reasonable approximation for a variety of plasma conditions.

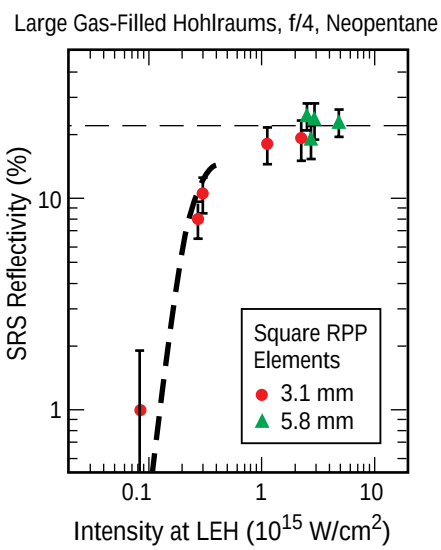

Fig. II-21. A plot of the SRS reflectivity into the interaction-beam cone, integrated over time, versus the interaction-beam intensity at the hohlraum laser entrance hole. The uncertainty in the beam intensity is approximately ±10% of its value.

SRS-Saturation Scaling

We have studied SRS saturation in the toroidal Nova hohlraums. For laser-intensity values similar to those in present NIF designs, it is observed that SRS is in a saturated state so that further increases in laser intensity do not yield a higher beam reflectivity. It is also observed that the SRS reflectivity depends on the damping rate of ion-acoustic waves (IAW), which is normalized to the real ion-acoustic frequency (ν_i/ω_i). Because SRS does not involve IAWs directly, this dependence may seem paradoxical. However, SRS can couple to other processes by further parametric decay of the SRS daughter electron-plasma wave, or SRS Langmuir wave (LW). The leading candidate is the Langmuir Decay Instability (LDI), in which the SRS LW further decays into an IAW and another LW,[22] as seen experimentally.[23] For a sufficiently strong laser drive, LDI daughter LWs themselves undergo LDI decay, creating so-called Langmuir turbulence. Langmuir turbulence is also relevant to ionospheric plasmas.

The dependence of SRS reflectivity on ν_i/ω_i has been studied with various gas fills in toroidal hohlraums, all at 1 atm of pressure and all designed to ionize to $n_e / n_c = 0.11$.[21] Both ν_i and ν_e are dominated by collisionless Landau damping for the plasma conditions of interest. In plasmas with multiple ion species, Landau damping of acoustic waves depends on the relative masses of the ions.[24,25] We have explored this fact, using the hohlraum gas fill, to vary ν_i/ω_i in our experiments. Again, C_5H_{12}, C_5D_{12}, CF_4, and C_5H_{12} + CF_4 low-Z gas fills are used.

The time-integrated SRS reflectivity data are shown in Fig. II-22. The data in this figure clearly show that as acoustic damping increases, SRS reflectivity increases. The laser intensity at the LEH is kept in the range of 2×10^{15} to 3.6×10^{15} W/cm^2. The observed scaling versus ν_i is consistent with the linear scaling predicted by a model of SRS saturation by Langmuir turbulence.[26]

SRS Images

It is very likely that SBS and SRS are spatially and temporally localized within the plasmas we study and do not have smooth, convective growth along the whole path of the laser beam within the plasma. In addition, it appears that SBS and SRS can mutually couple.[27–31] In order to resolve these issues, it is very desirable to image the scattered light in space and time and thus localize the SRS and SBS processes within the target. We have deployed two optical imaging instruments, the full-aperture-backscatter station imager (FABSI) and the axial imager at the Nova laser, to accomplish this task.[32,33]

In order to show the potential of SRS imaging as a density diagnostic, we show in Fig. II-23 an image of a conventional methane-filled, cylindrical Nova hohlraum using SRS light from the axial-imager diagnostic. We use the fact that the wavelength of SRS light depends on n_e. This type of hohlraum is used for studies of capsule illumination symmetry,[34] although this particular hohlraum has no capsule. The diagnostic was outfitted with a 550- to 650-nm band-pass filter, corresponding to n_e / n_c of 5%–15%. Out of the 2.2-ns pulse,

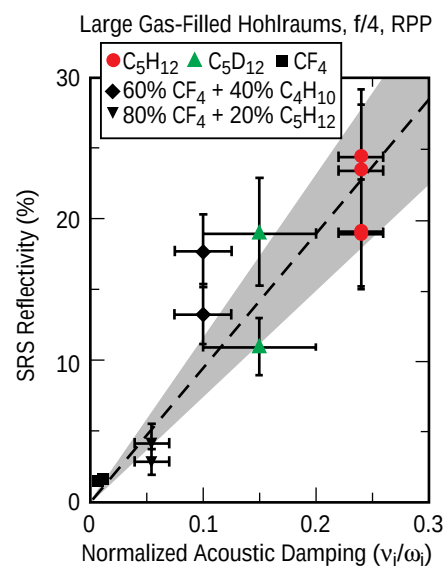

Fig. II-22. Raman backscatter reflectivities of the interaction beam for low-Z hohlraum gas fills. The least-squares linear fit (forced zero intercept) is shown. The shaded area shows the 95% confidence level for the fit.

the frame shown was gated for the 0.2- to 0.7-ns period. The image, when compared with the diagram on the bottom, shows that the LASNEX simulation predicts well the radial location of the 0.05-n_c density contour. However, although LASNEX correctly predicts a slight density buildup at the hohlraum axis, the observed density appears to be higher than the LASNEX prediction.

Summary

In summary, the speckled nature of laser beams used in ICF is an important factor in laser-plasma instability processes. For example, models that account for the laser speckles successfully predict the observed onsets of backscattering due to SBS and SRS. Linear convective theory predicts very large levels of SRS backscattering from the long-scale plasmas expected in ignition hohlraums. Our observations of SRS saturation are inconsistent with linear-theory scaling, but are qualitatively understood in terms of other processes. In particular, we have shown direct evidence for the dependence on acoustic damping of the SRS reflectivity. Since SRS itself is unrelated to acoustic waves, this dependence is evidence of other parametric processes determining the nonlinear saturation of Raman backscatter. We have great expectations from optical imaging diagnostics recently deployed at Nova. They could help elucidate important outstanding questions relating to SBS and SRS nonlinear saturation and could also prove to be a valuable density diagnostic.

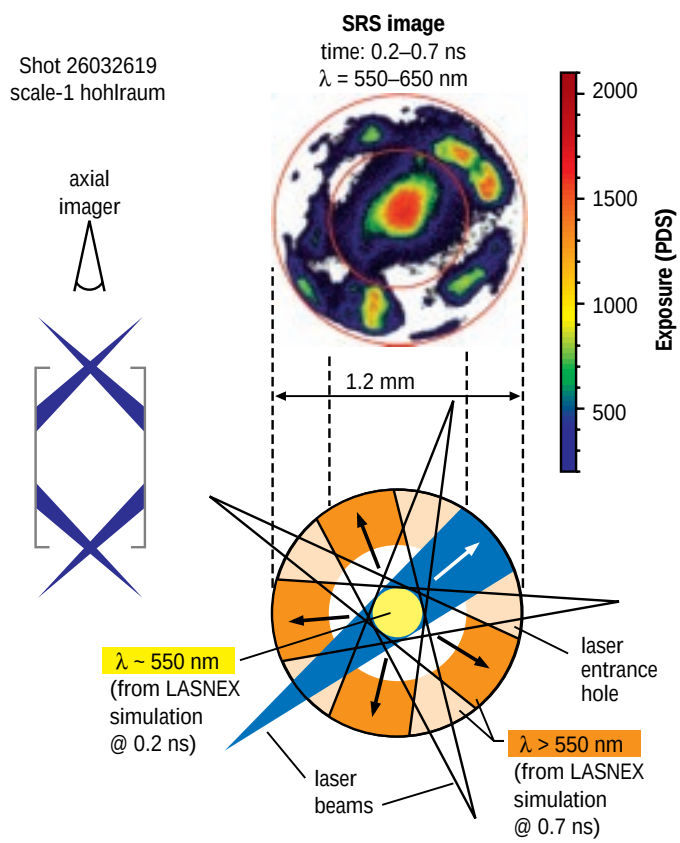

Fig. II-23. An image of the Raman scatter from a methane-filled scale-1 Nova hohlraum. The diagram on the left shows a side view of the hohlraum illumination geometry and the imager line of sight. The diagram on the bottom shows the hohlraum view from the imager location.

References

1. J. H. Nuckolls, L. Wood, et al., "Laser Compression of Matter to Super-High Densities: Thermonuclear (CTR) Applications," *Nature* **239**, 139 (1972).

2. J. D. Lindl, R. L. McCrory, and E. M. Campbell, "Progress toward Ignition and Burn Propagation in Inertial Confinement Fusion," *Physics Today* **45:9**, 32 (1992).

3. S. W. Haan, S. M. Pollaine, J. D. Lindl, et al., "Design and Modeling of Ignition Targets for the National Ignition Facility," *Physics of Plasmas* **2**, 2480 (1995).

4. W. J. Krauser, N. M. Hoffman, D. C. Wilson, et al., "Ignition Target Design and Robustness Studies for the National Ignition Facility," *Physics of Plasmas* **3**, 2084 (1996).

5. G. Zimmerman and W. Kruer, "Numerical Simulation of Laser-Initiated Fusion," *Comments on Plasma Physics and Controlled Fusion* **2**, 51 (1975).

6. B. J. MacGowan, B. B. Afeyan, C. A. Back, et al., "Laser-Plasma Interactions in Ignition-Scale Hohlraum Plasmas," *Physics of Plasmas* **3**, 2029 (1996).

7. J. C. Fernández, J. A. Cobble, B. H. Failor, et al., "Dependence of Stimulated Brillouin Scattering on Laser Intensity, Laser *f* Number, and Ion Species in Hohlraum Plasmas," *Physical Review E* **53**, 2747 (1996).

8. B. H. Wilde, J. C. Fernández, W. W. Hsing, et al., "The Design and Characterization of Toroidal-Shaped NOVA Hohlraums That Simulate National Ignition Facility Plasma Conditions for Plasma Instability Experiments," in *Proceedings of the 12th International Conference on Laser Interaction and Related Plasma Phenomena* (Osaka, Japan, April 1995), *AIP Conference Proceedings* **369:1**, 255 (1996).

9. E. M. Campbell, J. T. Hunt, E. S. Bliss, et al., "Nova Experimental Facility (Invited)," *Review of Scientific Instruments* **57**, 2101 (1986).

10. M. N. Rosenbluth, "Parametric Instabilities in Inhomogeneous Media," *Physical Review Letters* **29**, 565 (1972).

11. M. V. Goldman and D. F. DuBois, "Simulated Incoherent Scattering of Light from Plasmas," *Physics of Fluids* **8**, 1404 (1965).

12. L. M. Gorbunov, "Perturbation of a Medium by a Field of a Strong Electromagnetic Wave," *Soviet Physics JETP* **28**, 1220 (1969).

13. P. E. Young, K. G. Estabrook, W. L. Kruer, et al., "Backscattered Light near the Incident Laser Wavelength from 0.35 μm Irradiated Long Scale Length Plasmas," *Physics of Fluids B* **2**, 1907 (1990).

14. Y. Kato, K. Mima, N. Miyanaga, et al., "Random Phasing of High-Power Lasers for Uniform Target Acceleration and Plasma-Instability Suppression," *Physical Review Letters* **53**, 1057 (1984).

15. H. A. Rose and D. F. DuBois, "Statistical Properties of Laser Hot Spots Produced by a Random Phase Plate," *Physics of Fluids B* **5**, 590 (1993).

16. H. A. Rose and D. F. DuBois, "Laser Hot Spots and the Breakdown of Linear Instability Theory with Application to Stimulated Brillouin Scattering," *Physical Review Letters* **72**, 2883 (1994).

17. V. V. Eliseev, W. Rozmus, et al., "Effect of Diffraction on Stimulated Brillouin Scattering from a Single Laser Hot Spot," *Physics of Plasmas* **3**, 3754 (1996).

18. J. C. Fernández, B. S. Bauer, J. A. Cobble, et al., "Measurements of Laser-Plasma Instability Relevant to Ignition Hohlraums," *Physics of Plasmas* **4**, 1849 (1997).

19. B. B. Afeyan, A. E. Chou, and W. L. Kruer, "New Regimes of Parametric Instabilities in Plasmas with Flat-Topped and Depleted Tail Velocity Distribution Functions," submitted to *Physical Review Letters*.

20. R. G. Watt, J. Cobble, D. F. DuBois, et al., "Dependence of Stimulated Brillouin Scattering on Focusing Optic *f* Number in Long Scale-Length Plasmas," *Physics of Plasmas* **3**, 1091 (1996).

21. J. C. Fernández, J. A. Cobble, B. H. Failor, et al., "Observed Dependence of Stimulated Raman Scattering on Ion-Acoustic Damping in Hohlraum Plasmas," *Physical Review Letters* **77**, 2702 (1996).

22. D. F. DuBois and M. V. Goldman, "Radiation-Induced Instability of Electron Plasma Oscillations," *Physical Review Letters* **14**, 544 (1965).

23. K. L. Baker, R. P. Drake, B. S. Bauer, et al., "Thomson Scattering Measurements of the Langmuir Wave Spectra Resulting from Stimulated Raman Scattering," *Physical Review Letters* **77**, 67 (1996).

24. H. X. Vu, J. M. Wallace, and B. Bezzerides, "An Analytical and Numerical Investigation of Ion Acoustic Waves in a Two-Ion Plasma," *Physics of Plasmas* **1**, 3542 (1994).

25. E. A. Williams, R. L. Berger, R. P. Drake, et al., "The Frequency and Damping of Ion Acoustic Waves in Hydrocarbon (CH) and the Two-Ion-Species Plasmas," *Physics of Plasmas* **2**, 129 (1995).

26. B. Bezzerides, D. F. DuBois, and H. A. Rose, "Saturation of Stimulated Raman Scattering by the Excitation of Strong Langmuir Turbulence," *Physical Review Letters* **70**, 2569 (1993).

27. C. J. Walsh, D. M. Villeneuve, and H. A. Baldis, "Electron Plasma-Wave Production by Stimulated Raman Scattering: Competition with Stimulated Brillouin Scattering," *Physical Review Letters* **53**, 1445 (1984).

28. H. A. Rose, D. F. DuBois, and B. Bezzerides, "Nonlinear Coupling of Stimulated Raman and Brillouin Scattering in Laser-Plasma Interactions," *Physical Review Letters* **58**, 2547 (1987).

29. D. M. Villeneuve, H. A. Baldis, and J. E. Bernard, "Suppression of Stimulated Raman Scattering by the Seeding of Stimulated Brillouin Scattering in a Laser-Produced Plasma," *Physical Review Letters* **59**, 1585 (1987).

30. H. A. Baldis, P. E. Young, R. P. Drake, et al., "Competition between the Stimulated Raman and Brillouin Scattering Instabilities in 0.35-μm Irradiated CH Foil Targets," *Physical Review Letters* **62**, 2829 (1989).

31. D. S. Montgomery, B. B. Afeyan, B. J. MacGowan, et al., "Persistent Anti-Correlation of Stimulated Raman and Brillouin Scattering Levels in Laser-Produced Plasmas," submitted to *Physical Review Letters*.

32. J. C. Fernández, R. R. Berggren, K. S. Bradley, et al., "Improved Optical Diagnostics for the NOVA Laser," *Review of Scientific Instruments* **66**, 626 (1995).

33. M. D. Wilke, J. C. Fernández, R. R. Berggren, et al., "Full Aperature Backscatter Station Imager Diagnostic System for Far-Field Imaging of Laser-Plasma Instabilities at Nova," *Review of Scientific Instruments* **68**, 672 (1997).

34. N. D. Delamater, T. J. Murphy, A. A. Hauer, et al., "Symmetry Experiments in Gas-Filled Hohlraums at NOVA," *Physics of Plasmas* **3**, 2022 (1996).

Planar, Ablative Rayleigh-Taylor Instability Growth in Copper Foils Driven by Nova Hohlraum Radiation

G. T. Schappert, S. E. Caldwell,
W. W. Hsing (P-24),
D. E. Hollowell (XTA)

The Rayleigh-Taylor (R-T) instability is an instability of the interface between two materials when a lighter material pushes on and accelerates a heavier material. This situation can occur in implosions of inertial confinement fusion (ICF) capsules as well as in stellar dynamics in astrophysics. Of particular interest is the ablative R-T instability, in which the lower-density ablated material accelerates the bulk material through a rocket effect. The theory for this case was worked out some time ago, leading to an exponential growth rate γ for a perturbation in the ablation surface. This rate depends on the wave number of the perturbation, the scale length of the density gradient across the ablation front, the acceleration of the interface, and the mass-ablation rate. The instability growth rate for the ablatively driven acceleration is less than the classical growth rate (without ablation) under otherwise identical conditions. This reduced rate of instability growth is referred to as ablative stabilization.

The purpose of our research is to experimentally explore the ablative R-T instability in a high-density material and obtain results that can be modeled by various laboratory codes, thus benchmarking these codes with real experiments. The R-T experiments were performed at the Nova laser at Lawrence Livermore National Laboratory. The material that we investigated was copper, and the ablative drive was the ~180-eV radiation density generated in a scale-1 hohlraum. Two distinct experimental configurations were used: one with face-on radiography to measure perturbation growth, the other with edge-on shadowgraphy imaging of the growth. Both configurations used 6.7-keV x-rays. The two layouts are shown in Fig. II-24, and they are described in detail below.

Eight of the ten Nova laser beams (each with a wavelength of 0.351 μm [3ω], a pulse length of 2.2 ns, and an energy of about 3 kJ) were focused into the cylindrical hohlraum to generate the radiation drive of about 180 eV. The other two beams (each with a wavelength of 0.527 μm [2ω], a pulse length of 2–4 ns, and an energy of 3–4 kJ) were passed through random-phase plates to produce fairly smooth focal spots with diameters of about 500 μm on a 2-mm-diameter, 18-μm-thick iron disk. These beams generated 6- to 8-keV helium-like iron lines. This iron backlighter was used for both radiography and shadowgraphy. X-ray imaging devices were filtered with a 0.5-mil, cold-iron foil to remove the higher-energy lines and leave only the $1s^2$-$1s2p$ He_α line at 6.7 keV.

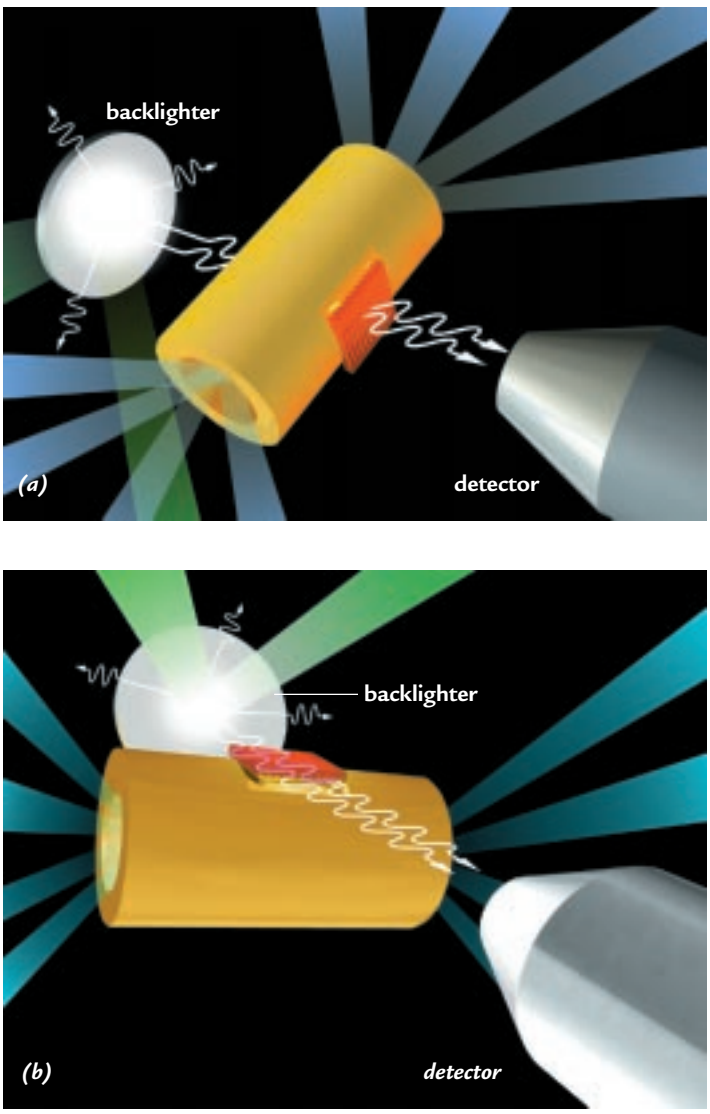

Fig. II-24. The experimental layout for (a) face-on radiography and (b) edge-on shadowgraphy, showing the eight Nova drive beams in blue, the two backlighter beams in green, the hohlraum in gold, the copper foil in red, and the x-rays that are emitted from the backlighter.

The hohlraums were standard scale-1 gold cylinders that were 2750 μm long and 1600 μm in diameter, with a 25-μm wall thickness and 75%-open end caps for laser-beam entrance holes. The copper targets were mounted over a hole in a slightly flattened region of the cylinder. For face-on radiography, a second hole in the cylinder diametrically across from the target let the backlighter radiation traverse the hohlraum and the target. The target was an 18-μm-thick flat copper foil with 45- or 80-μm-wavelength, 0.5-μm-amplitude sinusoidal corrugations milled on one side. A 600-μm × 600-μm square with the corrugations facing inward was mounted across the opening in the hohlraum.

For face-on radiography (Fig. II-24a), the target was imaged with a gated x-ray imager (GXI) along a line of sight that was normal to the target and that continued through the target and hohlraum to the center of the iron backlighter disk behind the hohlraum. The GXI produced 16 pinhole images in groups of four. Within a group, the images were separated by about 60 ps, and the time separation between groups was adjustable. The temporal resolution of the GXI was about 100 ps; the growth indicated in each image was averaged over that time. Each image then recorded the transmission of the 6.7-keV backlighter x-rays through the foil. The growth of the periodic perturbation caused by the R-T instability in the foil was mapped onto a periodic contrast variation in the GXI image, as shown in Fig. II-25. Also shown in Fig. II-25 is a line-out across the contrast corrugations. The oscillations at the fundamental wavelength and the appearance of a second harmonic are superimposed on the shape of the backlighter image.

The line-out for each image was analyzed, and the temporal development of the foil perturbation growth was reconstructed. The three major steps in this analysis are the subtraction of the backlighter image, Fourier analysis of the periodic perturbations, and correction of the Fourier components for the spatial resolution of the instrument. The amplitudes of the corrected Fourier

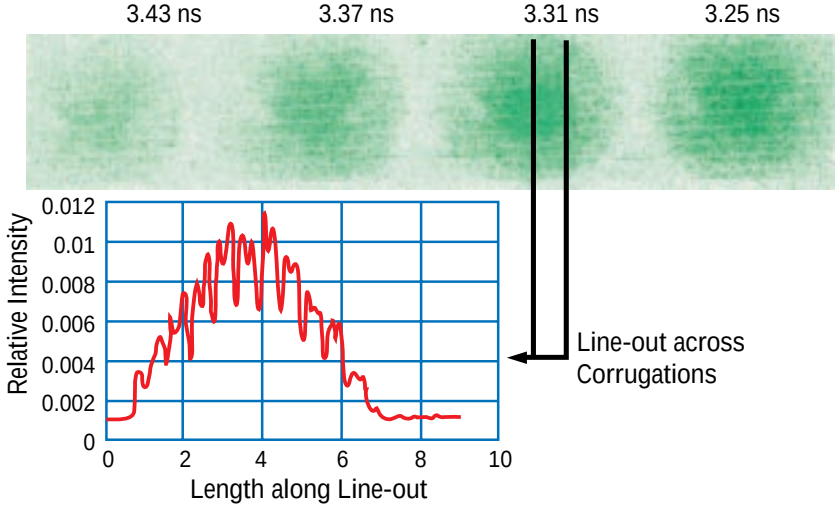

Fig. II-25. A time sequence of radiographs from a gated x-ray imager.

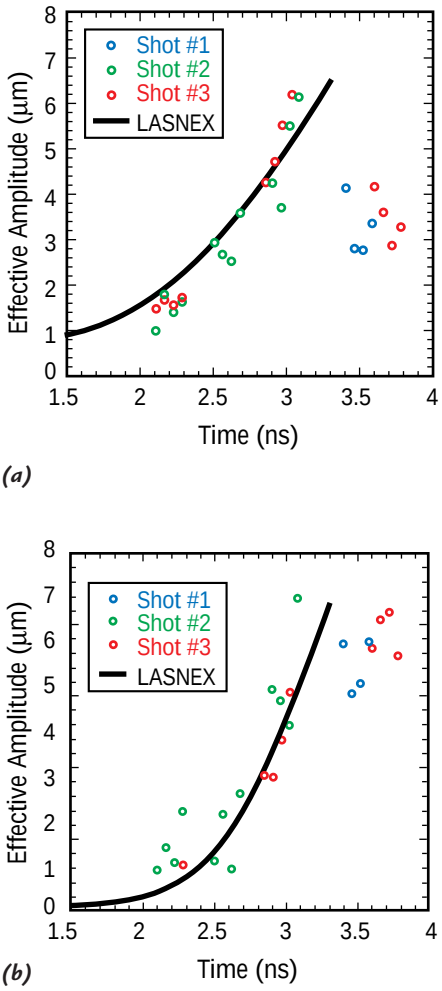

Fig. II-26. (a) The growth of the fundamental wavelength for the 45-µm corrugation. (b) The growth of the second harmonic for the 45-µm corrugation. The colors of the data points correspond to three different shots.

components reflect the growth of the contrast, that is, the integral of $\kappa\rho(x)\mathrm{d}x$ through the foil, where κ is the absorption coefficient of cold copper at 6.7 keV and ρ is the density. Although the copper was heated, the absorption at 6.7 keV is nearly the same as that for cold copper. Dividing the contrast amplitude by the cold-copper absorption coefficient gives an effective spatial amplitude based on cold, normal-density copper.

Figure II-26 shows this amplitude as a function of time for the 45-µm-wavelength perturbation and its second harmonic at 22.5 µm, respectively. The initial 0.5-µm amplitude of the fundamental wavelength is too small to give an observable contrast, and the second harmonic starts from zero amplitude since it was not initially present in the foil. The data for the fundamental wavelength show an initial exponential growth followed by an abrupt drop. This sharp drop is not fully understood. One would expect a gradual saturation of the amplitude followed by a decrease of all the harmonic amplitudes as the bubble-and-spike plasmas homogenize. Because the scatter in the data indicates fairly large error bars, the data could be consistent with a gradual saturation followed by a gradual drop.

Also shown in Fig. II-26 is a planar, two-dimensional LASNEX calculation (a calculation using an ICF design code) of the R-T growth using the Nova hohlraum drive. Considering the scatter of the data, the agreement is quite good for the earlier times. For later times, the calculation runs into numerical problems, which are being addressed. Results for the 80-µm corrugation foils showed slower growth and poorer agreement with our simulations. A shortcoming of this technique is that the contrast modulation in the GXI image does not directly reflect the spatial development of the perturbation in the foil but only the integral through the material. The bubble-and-spike formation in the later stages of R-T growth is observed indirectly as the appearance and growth of the second harmonic and, presumably, as higher harmonics if the instrument spatial resolution is sufficient. To observe this aspect of the R-T instability, we imaged the R-T growth in an edge-on configuration (Fig. II-24b).

The target was again mounted across an opening in the slightly flattened side of the hohlraum, offset with two 50-µm spacers. The line of sight was edge-on, down the length of the corrugations onto the center of the backlighter disk, which was also visible between the two spacers and the hohlraum and target. Two imaging techniques were used in this configuration. A GXI was used to image the growth of the corrugations directly edge-on. The bubble-and-spike formation at about 3.6 ns in an 80-µm-wavelength

corrugated foil is shown in Fig. II-27. The bright region in the lower half of the image is the direct view of the backlighter disk. The shadow of a 25-μm-diameter, gold-wire fiducial is seen in the lower right. The shadow of the lower edge of the copper foil and the spikes toward the top are clearly visible. In this case, the 6.7-keV backlighter x-rays propagated down the 600-μm-long channels of bubbles and spikes, resulting in the dark spikes and lighter bubbles. The light stripe near the top of the image is a view of the backlighter through the 50-μm offset between the foil and the hohlraum. We suspect that the dark region above the bubble-spike region and below the offset is foil plasma from the edges of the foil that were left behind in the drive because the foil was somewhat larger than the opening in the hohlraum. We plan to repeat these shots with foils mounted such that the front and back edges are well inside the opening.

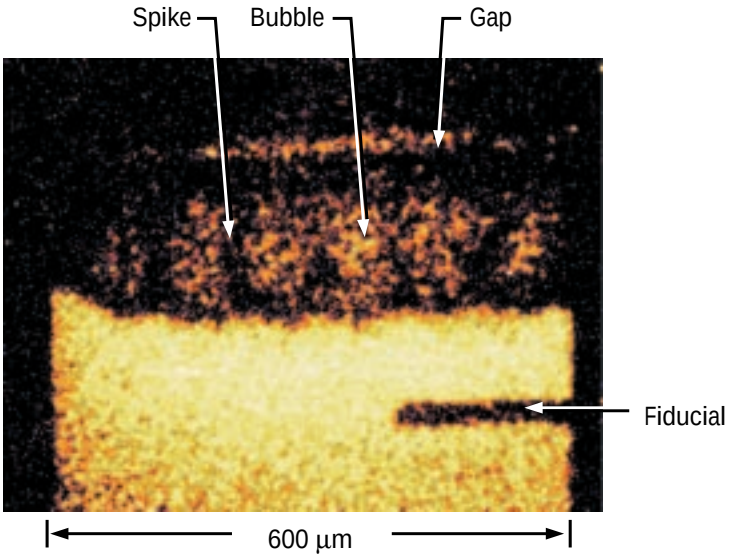

Fig. II-27. A side-on image of the bubbles and spikes.

The GXI images at various time steps can be analyzed to determine the net motion of the foil away from the hohlraum. A more precise measurement of the motion can be made with a streak camera. There is, however, a difference. The GXI image is in two dimensions, whereas the streak camera images only one. Figure II-28a shows a typical streak of the motion of a 45-μm-wavelength corrugation foil. The bright portion of the streak image is the direct view of the backlighter, showing the shadow of a fixed fiducial across the lower half of the image. The upper half shows the near-parabolic path of the back of the foil and the expanding copper plasma with the spikes and bubbles above it. Across the top in the image is the view to the backlighter through the 50-μm offset between the hohlraum and target. Figure II-28b shows the trajectories for a flat foil, for two foils with 45-μm corrugation wavelengths, and for two foils with 80-μm corrugation wavelengths. Also shown is a LASNEX calculation for a foil with a 45-μm corrugation wavelength. The agreement is quite good. There seems to be no dependence of the foil trajectory on the corrugation wavelength within the error of the measurements, considering that the time origin for the five shots is within ±100 ps, consistent with the limitations of the Nova electrical-trigger system.

The experiments discussed above are part of a laser-based, above-ground experiments (AGEX) program to study hydrodynamic instabilities. The preliminary experimental results presented are in reasonable agreement with modeling. However, better diagnostics (better in both spatial and temporal resolution), more accurate techniques for deconvolving the instrument function, and simulations that cover the whole temporal range of the experiment are required to benchmark a calculation in detail. This work is in progress.

The authors would like to thank the P-24 Nova technicians, the MST target-fabrication staff, and the Nova operations staff for their contributions to these experiments.

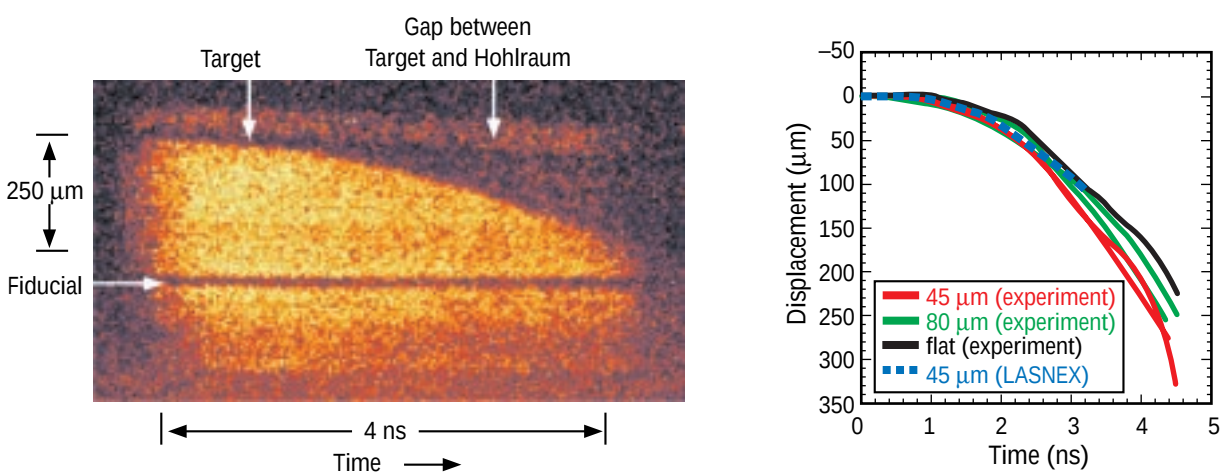

Fig. II-28. (a) The steaked motion of the back of the 45-μm corrugated target. (b) The streaked motion of the back of a flat foil and the backs of foils with 45- and 80-μm corrugation wavelengths. Also included is the LASNEX simulation for a foil with a 45-μm corrugation wavelength.

Penning Fusion Experiment

M. M. Schauer, T. B. Mitchell (P-24), D. C. Barnes (XCM)

For over forty years, physicists have pursued the goal of a fusion energy device. Work toward this goal has concentrated on devices that attempt to heat and store neutral plasmas, such as gases consisting of positive ions and electrons in equal or almost equal numbers. These devices have reached impressive temperatures and densities, but the confinement times have left much to be desired because neutral plasmas are prone to instabilities.

At the other end of the spectrum are Penning and Paul traps, which store nonneutral plasmas consisting of pure clouds of electrons, positive ions, or negative ions. These devices have achieved virtually infinite confinement times, but the densities of the stored plasmas have been limited by the Coulomb repulsion between the constituent particles. The limiting value of the density attainable is known as the Brillouin limit. The Penning Fusion Experiment (PFX) seeks to circumvent this limitation in a small electron Penning trap.

In their simplest form, Penning traps are composed of a ring electrode and two end caps (Fig. II-29). If the ring electrode is biased positively with respect to the end caps, the potential inside the trap is a saddle potential that provides confinement for electrons along the trap axis. Obviously, the electrons are not confined radially by the electrostatic potential; they are instead prevented from escaping radially by a magnetic field that is applied parallel to the trap axis. An electron confined by these fields will execute an axial oscillation in the electrostatic well and a cyclotron orbit about the magnetic-field lines. Additionally, the electric and magnetic fields will give rise to an $E \times B$ drift of the center of the cyclotron orbit about the trap axis.

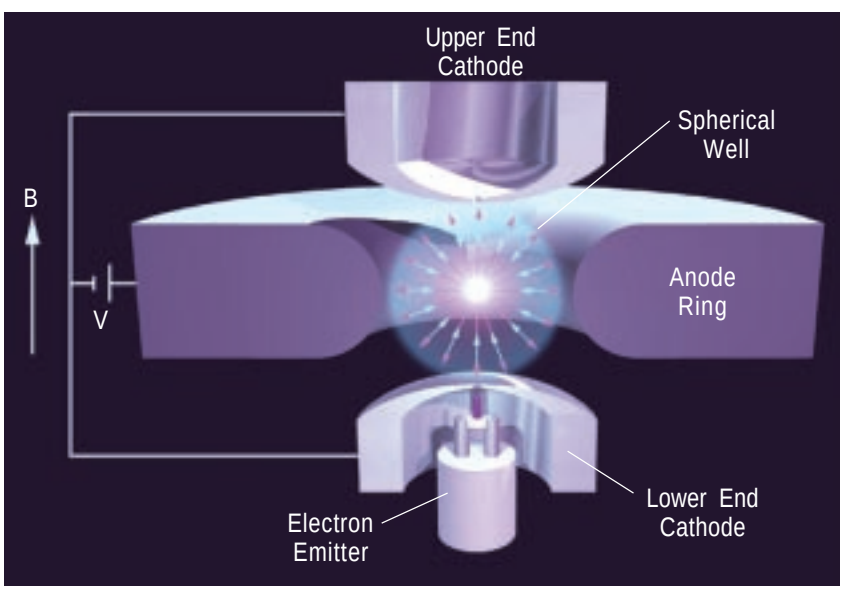

Fig. II-29. Schematic representation of the Penning trap showing the effective spherical well boundary and the reflected electron trajectories.

PFX uses these oscillations to produce a high-density plasma at the center of the trap. This is accomplished by introducing a low-energy, low-divergence electron beam from a LaB_6-crystal electron emitter through a 400-μm-diameter hole in the lower end cap and reflecting it by means of a small, negative voltage applied to the upper end cap. In the absence of scattering, an electron in the beam will simply return to the emitter or to the lower end cap and be lost from the trap. If, however, some of the electron's energy is scattered from its axial motion into its radial degrees of freedom, the electron will remain confined in the axial well and will execute a combination of the oscillations described above.

For a proper choice of trapping potential and applied magnetic field, the period of an electron's axial motion will be twice the period of its radial motion, and any orbit originating at the center of the trap will be constrained to pass through the center again. A collection of electrons that all follow such orbits will produce a dense, "focused" plasma. An alternate picture is that the combined electric and magnetic fields provide an effective well that is spherical for the proper choices of the field strengths. Then, any trajectory originating at the trap center will be reflected back on itself by the spherical wall of the well. This situation is shown schematically in Fig. II-29.

It is important to note that the electrons executing these orbits have zero (or near-zero) angular momentum. To preserve this beam-like state, it is essential that scattering occur mostly at or near the trap center. Excessive numbers of collisions away from the center will result in a more-or-less uniform electron cloud that will effectively wash out the focus. To minimize this thermalizing scatter, we operate PFX at liquid-helium temperature, thereby assuring an extremely low background pressure ($<10^{-10}$ torr). Intrabeam scattering does occur throughout the electron-beam volume but, because of the narrow energy distribution of the beam electrons, proceeds at a sufficiently slow pace to allow focusing effects to dominate the thermal background that is generated. In fact, as we explain later, a small amount of intrabeam scattering is desirable.

In order to maximize the density attained, it is desirable to use high electric-field strengths. Hence, the trap must be designed to hold high ring voltages. The present trap, through judicious choice of materials and the excellent vacuum achieved in the cryogenic environment, is capable of holding up to 30 kV across the 1.5-mm gap between the ring and the end caps. Addition of the magnetic field significantly degrades the voltage standoff so that the actual operation is limited to voltages below 10 kV. Figure II-30 is a picture of the trap assembly, which consists of titanium electrodes and precision ceramic spacers.

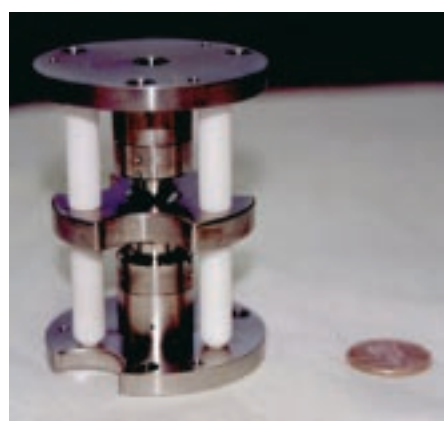

Fig. II-30. The trap used in these experiments. The spacing between the titanium end-cap electrodes is 6 mm and is maintained to within 5 μm by high-precision, polished alumina spacers. The inner diameter of the ring electrode is also 6 mm.

PFX has been operating for almost two years and has conclusively demonstrated the formation of a density focus. The hallmark of this focus is scattering of the injected electron current to the ring electrode. As is evident from Fig. II-29, the electron orbits in the focused, spherical state extend all the way to the ring and thus allow electron current to flow from the beam to the ring. Figure II-31a shows a plot of the current flowing to the ring for a fixed magnetic field as the ring voltage is increased. The sharp peak occurs at the voltage at which a focused state is expected to exist for the given magnetic field.

Current to the anode is shown for two different values of the electron current that is injected through the hole in the lower end cap. For the lower injection current, essentially no current flows to the anode, while at the higher current, a full 20% of the injected current is deflected to the ring. An interesting indication of the mechanism by which the focus establishes itself appears when one examines more closely the relation between the injected current and that current flowing to the anode ring. This data is shown in Fig. II-31b for a fixed magnetic field and anode voltage. The blue curve is for increasing injection current, while the red curve is for decreasing injection current.

The hysteresis is an indication of the role played by thermal electrons. These electrons are scattered out of the injected beam by the intrabeam scattering mentioned earlier and form a uniform (that is, unfocused) thermal population that coalesces to the trap center and remains there for several seconds. An equilibrium is established between scattering into and loss out of the trap, so the density of this population is related to the magnitude of the injected current. At some threshold value, the space charge of the thermal plasma becomes large enough to significantly deflect the injected electrons, thereby forming a density focus as described above. Once established, the focus maintains itself by virtue of its own space charge disintegrating only when the replenishment rate falls below a critical value. This critical value is represented by the lower threshold of the red curve.

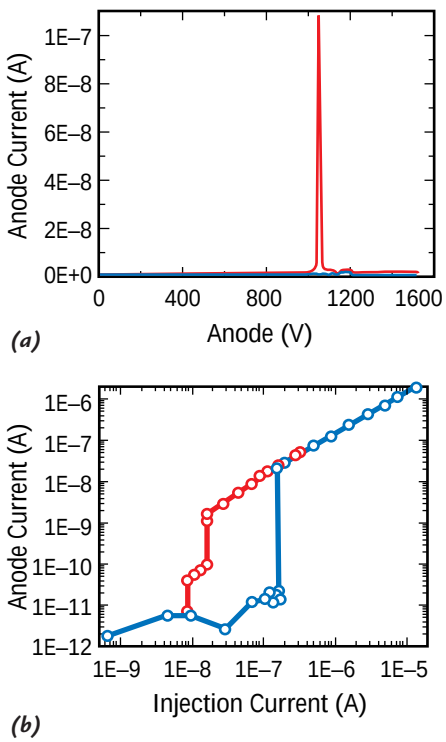

Fig. II-31. (a) The total electron current flowing to the anode ring plotted as a function of the voltage for a fixed magnetic field with two different values of the current injected into the trap. (b) The total electron current flowing to the anode at a fixed "spherical" point as a function of the total current injected into the trap.

Although the attained density has not been directly measured, a numerical calculation of the density has been performed based on PFX data and physical parameters. The results of these calculations are shown in Fig. II-32. The calculation shows a plasma core of peak density approximately 35 times the Brillouin limit with a radius of roughly 20 μm. This calculation is consistent with core sizes inferred from the widths of resonance peaks in various scattering diagnostics. Also shown in Fig. II-32 is the potential in the trap volume, including the space-charge potential of the electron plasma.

Figure II-32 provides the impetus for much of the future work planned for PFX. One can imagine introducing neutral atoms into the trap volume that will be ionized and accelerated by collisions with plasma electrons. The space charge of the electron plasma will confine some of the ions thus produced and will result, it is hoped, in a high-density, thermonuclear plasma. We are presently working on such a gas-introduction capability.

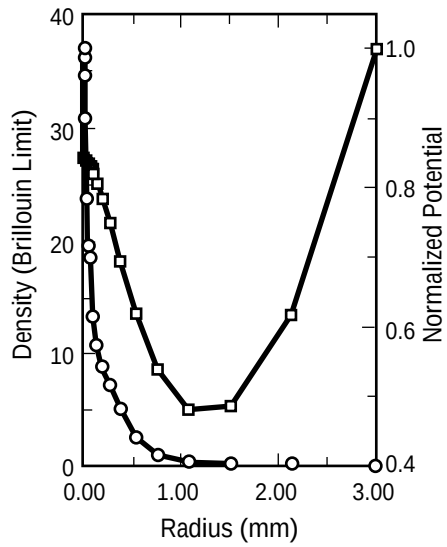

Fig. II-32. The calculated electron density in the trap volume (circles) plotted as a function of the radius, which is normalized to the Brillouin limit. Also shown is the sum of the vacuum potential and the electron plasma space charge (squares), which is normalized to the vacuum potential at the trap wall.

Enhanced Radio-Frequency Field Penetration in an Inductively Coupled Plasma

M. Tuszewski (P-24)

The multibillion-dollar semiconductor industry uses plasma processing to produce various components, including multiple wafers, multichip modules, and flat panel displays. Always searching for methods that will increase yield and throughput and that, at the same time, will allow them to make smaller components, semiconductor manufacturers are focusing much effort on developing uniform, high-density, large-area plasmas that will help them optimize techniques such as sputtering, etching, and ion implantation and deposition. As part of this effort, Los Alamos has worked with Novellus Systems, a leading U.S. manufacturer of semiconductor process equipment, to develop and study a low-frequency, inductively coupled plasma (ICP) source for producing semiconductor devices with 0.25-μm geometries.

ICPs consist of a dielectric chamber surrounded by a conducting coil. Radio-frequency (rf) power is continuously applied to the coil and induces electric fields that partially ionize a gas inside the chamber and sustain a discharge. Most of the rf power is absorbed by the plasma; understanding this absorption is necessary for describing ICP heating and transport properties, which are important factors in predicting whether a plasma is radially uniform. Present models that consider induced rf electric fields (but not magnetic fields) predict that the rf power transfers to plasma electrons within a thin skin layer near the plasma surface. For typical rf frequencies of 0.1–13.56 MHz, the skin depths δ are a few centimeters, whereas the device dimensions are 10–30 cm.

During our work with Novellus, we obtained data that contradicted the current models by indicating deep rf penetration into argon ICP discharges with small skin depths. Because such deep penetrations are needed in semiconductor manufacturing processes,

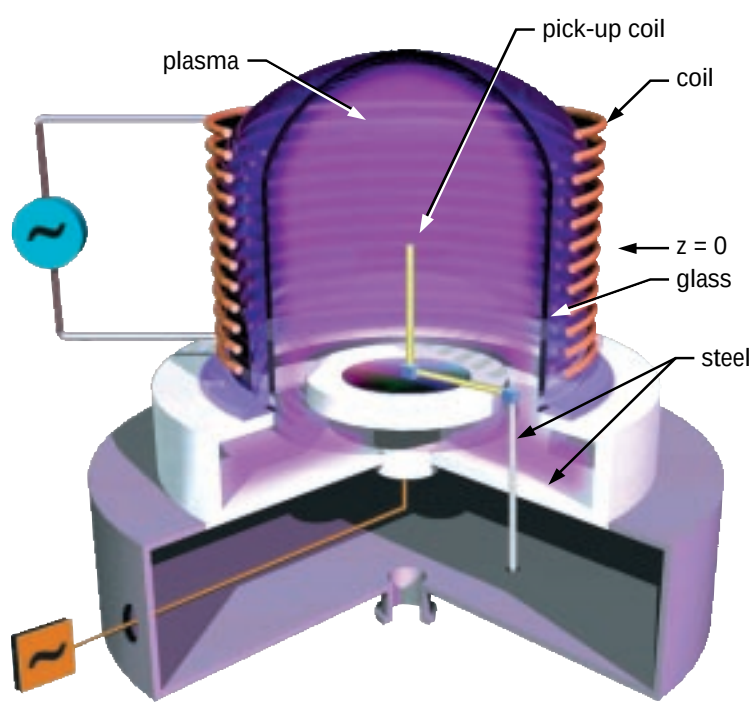

Fig. II-33. Sketch of the inductively coupled plasma.

this enhanced rf field penetration—previously unknown to the semiconductor manufacturers—was an important breakthrough. We realized that we would have to invoke a new mechanism to explain the enhanced penetration. Fluid calculations suggested that this mechanism is a reduction of the plasma conductivity by the induced rf magnetic fields when the electron cyclotron angular frequency ω_c exceeds both the rf angular frequency ω and the electron-neutral collision frequency ν, a condition that is satisfied for many low-pressure ICPs. Hence, the induced rf magnetic fields must be included in ICP models to predict electron heating and the resulting plasma transport.

To test this mechanism experimentally, we measured the induced rf magnetic fields inside a cylindrical ICP, which is sketched in Fig. II-33. A 13-turn copper coil was wound around a glass bell jar with an inner radius of 16.5 cm, and the coil was powered by a 2-kW, 0.46-MHz ($\omega = 2.9$ megacycle) rf generator. A small pick-up coil (with 18 turns, a diameter of 4 mm, and a length of 5 mm) with shielded, twisted leads was inserted near the closed end of a 6-mm-diameter ceramic tubing, which was connected to a stainless-steel shaft via ceramic transition pieces. We oriented the pick-up coil to measure the z (upward) component of the induced rf magnetic field, and we obtained radial scans in the coil midplane ($z = 0$) by rotating the steel shaft.

Argon discharges were sustained with gas pressures of 5–50 mtorr and with rf powers of 0.5–1.5 kW. We obtained radial profiles of the ion density (Fig. II-34) and estimates of the electron temperatures T_e from a voltage-swept, cylindrical Langmuir probe. For the discharges of Fig. II-34, the T_e profiles are radially uniform, and the electron energy distributions are almost Maxwellian. We also calculated the collision frequency to within 10% of the collision frequencies used in other ICP experiments and models. Our measured magnitudes $|B|$ of the induced rf magnetic field B_z are shown with symbols in Fig. II-35 for 5-mtorr argon discharges. The $|B|$ profiles are quite flat near the wall and change curvature at smaller radii. The magnitudes of B and of the coil azimuthal electric field E_c increase with rf power.

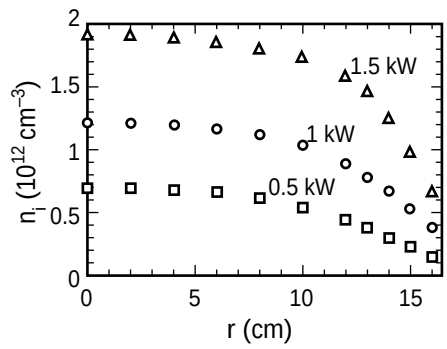

Fig. II-34. Measured radial profiles of the ion density for argon discharges with 5-mtorr gas pressure and with 0.5-, 1-, and 1.5-kW rf power.

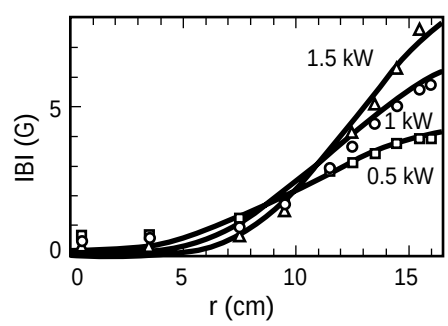

Fig. II-35. Radial profiles of the rf magnetic-field amplitude for 5-mtorr argon discharges. The measured data are indicated with symbols, and the magnetized calculations are shown with solid lines.

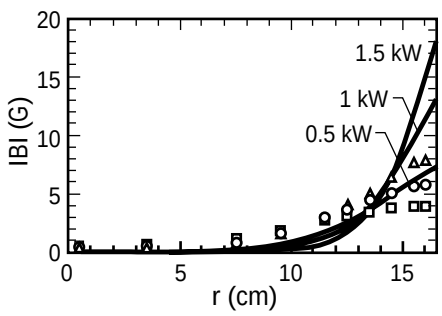

Fig. II-36. Radial profiles of the rf magnetic-field amplitude for 5-mtorr argon discharges. The measured data are indicated with symbols, and the unmagnetized calculations are shown with solid lines.

We first compared our magnetic-field data with the predictions from existing models by using a fluid approach to describe the ICP discharges. For simplicity, we used a one-dimensional model with $B = B_z(r)$, where r is the radius of the ICP. Combining Faraday's, Ohm's, and Ampere's laws, we obtained the following expression:

$$(1/r)(d/dr)(r/\sigma)(dB/dr) = i\omega\mu_0 B \quad , \tag{1}$$

where $\sigma = ne^2/[m(\nu + i\omega)]$ is the plasma conductivity, n is the plasma ion density, m is the electron mass, and μ_0 is the permeability of free space. We solved this equation with the density profiles of Fig. II-34.

The calculated radial $|B|$ profiles are shown in Fig. II-36 with solid curves, and the experimental data are also shown with symbols for comparison. The calculated $|B|$ magnitudes and decays are overestimated by factors of 2–3. In addition, the exponential-like calculated profiles do not reproduce the change of curvature observed near the wall. The uncertainties in the calculated penetration depths δ_c are estimated to be about 40%, but these uncertainties do not explain the above discrepancies. Clearly, a better model is required.

Previously, when we had calculated σ, we had neglected a magnetic term that introduces a nonlinearity into the electron momentum equation from which σ is derived. After including this magnetic term, we were able to define the following effective conductivity $\langle\sigma\rangle$ that is time averaged over an rf period:

$$\langle\sigma\rangle = \sigma_0/(1+|\omega_c|^2/\nu^2)^{1/2} - i\sigma_0(\omega/\nu)/(1+|\omega_c|^2/\nu^2)^{3/2} \ , \tag{2}$$

where $\sigma_0 = ne^2/(m\nu)$ is the zero-frequency collisional conductivity. Replacing σ with the value of $\langle\sigma\rangle$, we solved Eq. 1 again. The calculated $|B|$ profiles are shown in Fig. II-35 with solid curves. The calculated and observed $|B|$ magnitudes agree within 5% near the wall, and the calculations also reproduce the shape of the observed profiles. The edge flattening and the change in the profile curvature are due to low edge plasma conductivities $\langle\sigma\rangle$.

We also measured the $|B|$ profiles for argon discharges with higher gas pressures of 10–50 mtorr. The magnetized calculation agrees with the data for all pressures, and the discrepancy between the unmagnetized calculation and the data gradually diminishes as the gas pressure increases. The experimental data and both

calculations coincide within the uncertainties for 40- and 50-mtorr discharges. This agreement is expected since $\langle\sigma\rangle \approx \sigma$ in high-pressure discharges for which ν exceeds $|\omega_c|$ through most of the plasma volume. The agreement between the data and the calculations also implies that the combined experimental uncertainties are less than a factor of 2.

In addition to studying argon discharges, we also measured and calculated the $|B|$ profiles of oxygen discharges, which are more representative of industrial ICPs. These oxygen discharges yield results that are qualitatively similar to those for argon, except that the rf penetration depths are larger by factors of 2–3 because the oxygen discharges have lower plasma densities. The rf magnetic fields of the oxygen discharges are 1–3 G on the axis. Hence, the plasma conductivity is substantially reduced by the rf magnetic field at all radii.

Although we did not experimentally investigate cases with $|\omega_c| > \omega > \nu$, numerical averages of σ over an rf period suggest that Eq. 2 remains a good approximation whenever $|\omega_c|$ is greater than ω and ν, regardless of the relative magnitudes of ω and ν. Hence, the ICP rf-power absorption depends on the largest of ω, ν, $|\omega_c|$, and the effective stochastic frequency ν_s. The regime where $|\omega_c|$ is the largest has been overlooked until now. Because the induced rf magnetic fields are only 3–10 G for typical rf powers (seemingly negligible), they are usually neglected in ICP models. However, the corresponding values of $|\omega_c| \approx (50–180) \times 10^6$ rad/s are often larger than typical values of $\nu \approx (5–20) \times 10^6$ s^{-1} and $\omega \approx (1–85) \times 10^6$ rad/s. As a result, the rf penetration depths δ are often substantially increased by the rf magnetic field, and the ohmic heating-power densities ($\sim 1/\delta^2$) can be reduced by an order of magnitude.

In summary, the induced rf magnetic fields of a low-frequency ICP show substantial penetration, whereas existing models predict absorption in a thin skin layer. Fluid calculations resolve this apparent contradiction: the induced rf magnetic fields appreciably reduce the plasma conductivity, which leads to a larger rf penetration. The rf magnetic fields can significantly modify the electron heating and the resulting plasma transport in many of today's low-pressure ICPs, and they should therefore be included in future ICP models.

MEGA: Search for the Rare Decay $\mu^+ \rightarrow e^+\gamma$

M. D. Cooper, M. Brooks, A. V. Chernyshev, G. W. Hart, G. E. Hogan, M. A. Kroupa, V. D. Laptev, D. M. Lee, G. B. Mills, R. E. Mischke (P-25), F. J. Naivar, C. Pillai, J. C. Sturrock (LANSCE-6), P. S. Cooper (Fermi National Accelerator Laboratory), Y. Chen, M. Dzemidzic, A. Empl, E. V. Hungerford, III, K. Lan, B. W. Mayes, II, W. von Witsch (University of Houston), K. Stantz, J. Szymanski (Indiana University), C. Gagliardi, R. E. Tribble, X. Tu (Texas A&M University), D. D. Koetke, R. Manweiler, S. Stanislaus (Valparaiso University), K. O. H. Ziock (University of Virginia), L. E. Piilonen (Virginia Polytechnic Institute and State University)

Searching for rare decays like $\mu^+ \rightarrow e^+\gamma$ is a sensitive method to discover physics beyond the standard model of electroweak interactions because this model predicts their rates to be zero or immeasurably small. Even though no such transitions have been observed, most physicists believe that the standard model must be imbedded in a larger theory because of the number of unexplained constants it contains. Nearly all of the candidates for the larger theory predict rare decays to proceed at rates close to the current limits.

For a rare decay to be seen at a measurable rate, the process must be mediated by a new particle that is virtually exchanged between leptons and/or quarks. The structure of the electroweak theory is simpler if the mass scale for these new particles is below 1 TeV. The current experiments that are searching for rare decays are sensitive in the mass range between 50 GeV and 1 TeV, spanning the gap between direct production experiments and the 1-TeV scale. The possibilities for a discovery of great importance are nonnegligible. In the past two years, there has been intense speculation over one particular theory, supersymmetry. Supersymmetry postulates matching all of the known particles of spin ½ or 1 with superpartners that have either spin 1 or ½, respectively. These new particles can mediate the process $\mu^+ \rightarrow e^+\gamma$ and induce rates within the sensitivity range of the MEGA (muon decays to an electron and a gamma ray) experiment. These models predict that $\mu^+ \rightarrow e^+\gamma$ will be the largest rare decay. Supersymmetry can also be a low-energy reduction of a grand-unified theory, in which case the rates are felt to be large because of the high mass of the newly discovered top quark. If one samples supersymmetric models, the MEGA experiment spans about half of the potential parameter space with its branching-ratio sensitivity (90% confidence) down to 10^{-12}; the current limit is 5×10^{-11}.

The MEGA apparatus was described in the 1994 Physics Division progress report (M. D. Cooper et al., "MEGA: Search for the Rare Decay $\mu^+ \rightarrow e^+\gamma$," in "Physics Division Progress Report, January 1, 1994–December 31, 1994," G. Y. Hollen and G. T. Schappert, Eds., Los Alamos National Laboratory report LA-13048-PR [November 1995], p. 76). Only a brief recap will be repeated here. MEGA took advantage of the intense beams of the surface muons available at LAMPF (a 20-MHz average stop rate was used). The detector was contained in a large, warm-bore solenoid (1.5 T, 1.85 mφ × 2.9 m long) and consisted of two arms (Fig. II-37). The first, a set of special, cylindrical, proportional chambers, measured the kinematic properties of the decay electrons, and the other, the world's largest pair spectrometers, determined the same quantities for the photon. All of the charged particles arising from muon decay were confined by the magnetic field to the positron elements, leaving the photon counters in a relatively quiet environment. The MEGA collaboration, currently consisting of six university groups and two national laboratories, completed taking its data at the end of 1995. An intense analysis effort was begun to extract viable candidates from the stored events.

There are 4.5×10^8 events stored on tape from the three data runs that occurred during 1993–1995. These events are the remains of roughly 1.5×10^{14} muons that decayed in the detector during its 1.1×10^7 live seconds. Highly improbable events have been discarded in the hardware and software during the acquisition. The signature for $\mu^+ \rightarrow e^+\gamma$ is a 52.8-MeV photon and a 52.8-MeV electron that are back to back, from a common vertex, and in time coincidence, and the excellent resolution of the spectrometers at high rates allows the potential signal to be separated from the background. To establish which events might fit this description, sophisticated software is being used to reconstruct and sort the events.

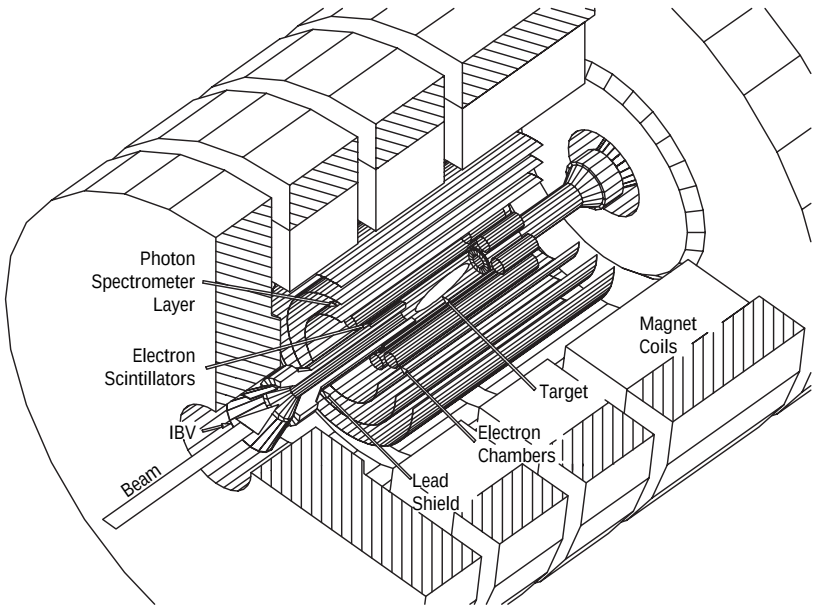

Fig. II-37. A simplified cutaway view of the MEGA apparatus. The detector is mounted inside a superconducting solenoid with a 1.5-T field. The muons enter along the magnetic field and stop in the target. Positrons from muon decays are detected in the eight cylindrical wire chambers and in the cylindrical arrays of scintillators surrounding the beam pipes. The three large cylinders are pair spectrometers for photon detection.

Four pieces of information are needed to measure a branching ratio. First, the energy, time, and geometrical scales of the detector must be calibrated so that the location of the signal is established. Second, the response functions of the detector elements must be determined so that the range of event properties (for example, the energies, times, and angles) for probable events is given by the resolutions. Third, the number of viable candidates, running anywhere from 0 to 100 in our sensitivity range, must be found. Last, the number of muon decays for which the detector was fully efficient $\mu^+ \rightarrow e^+\gamma$ needs to be determined.

The first two necessities of the analysis are given either from the data or from auxiliary measurements. The three simplest kinematic parameters to understand are the positron energy, the photon energy, and the relative time of decay. Figure II-38 displays the energy spectrum for positrons decaying at high rates (250 MHz instantaneously) in black. An idealization of this spectrum would be a roughly flat response up to 52.8 MeV and a precipitous step down to zero counts beyond that point. The experimental result shows that the energy is correctly calibrated to be 52.8 MeV, and the full-width half-maximum of the detector response is 0.7 MeV, as given by the 10%–90% points on the step function. In addition, there are a few percent of unphysical

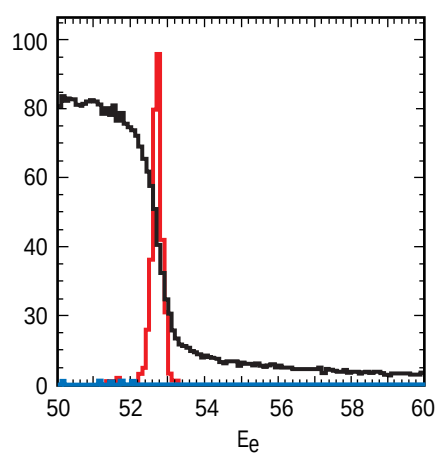

Fig. II-38. The Michel spectrum of normal muon decay at high rates is shown in black. The red curve is the signal expected for $\mu^+ \rightarrow e^+\gamma$ based on Monte Carlo simulations. The blue histogram contains the data with tight cuts on the time difference, the angle between the particles, and the photon energy.

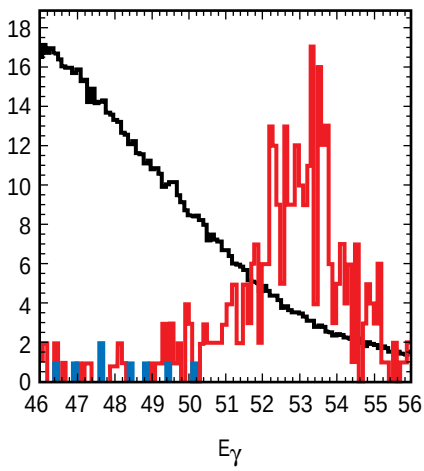

Fig. II-39. The photon spectrum from bremsstrahlung at high rates is shown in black. The red curve is the signal expected for $\mu^+ \to e^+\gamma$ based on Monte Carlo simulations. The blue histogram contains the data with tight cuts on the time difference, the angle between the particles, and the positron energy.

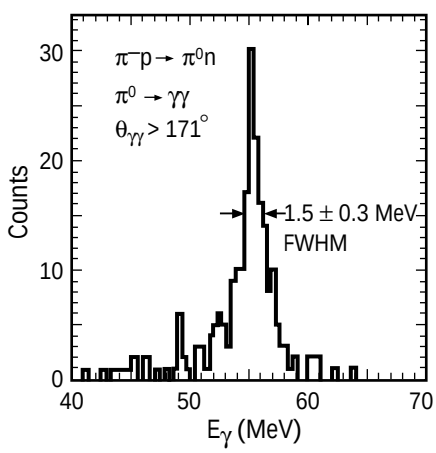

Fig. II-40. A spectrum from $\pi^0 \to \gamma\gamma$ with the angle between the gamma rays greater than 171°. Each π^0 is produced by stopping a π^- in a CH_2 target.

events at a higher energy that are caused by confusion of the pattern-recognition code by extra hits in this high-rate environment; these unphysical events represent a small inefficiency for finding the signal.

The corresponding energy spectrum for the photons is shown in black in Fig. II-39. This spectrum, whose origin is bremsstrahlung ($\mu^+ \to e^+\gamma\nu\nu$), is expected to fall rapidly as the energy approaches the 52.8-MeV endpoint. Again, there are some unphysical high-energy events that represent extra background. This spectrum contains no distinct features to use as a calibration. To overcome this deficiency, photons are measured from the decay $\pi^0 \to \gamma\gamma$. If the π^0 is made from stopping pions via the process $\pi^- p \to \pi^0 n$, the energies of the two gamma rays range from 54.92 to 82.96 MeV. By selecting only decays with an angle of at least 171° between the photons, nearly monoenergetic gamma rays of 55 MeV are isolated, as seen in Fig. II-40. Again, the energy calibration is seen to agree with its predicted value, and the resolution is 1.5 ± 0.3 MeV.

The primary background to the $\mu^+ \to e^+\gamma$ process is random coincidences between a positron from one muon decay and a photon from a second muon decay via the $\mu^+ \to e^+\gamma\nu\nu$ process. At the full beam intensity, the prompt coincidences from $\mu^+ \to e^+\gamma\nu\nu$ are completely swamped by the accidentals. However, if the beam intensity is greatly lowered and the magnetic field is somewhat reduced, a clear peak is observed at a time difference of zero (Fig. II-41). This feature demonstrates that the timing is correctly prepared. The observation of the peak demonstrates that the apparatus can observe a real coincidence process.

At this time, the collaboration has analyzed the 1993 data, which represent one-sixth of the total sample. Each event must be reconstructed by a very-time-consuming program that converts the detector signals into particles whose kinematic properties are known. For this subset of the data, the equivalent of 30 Hewlett-Packard 100-MHz workstations have computed continuously for one month at Indiana University, Los Alamos, and Texas A&M University.

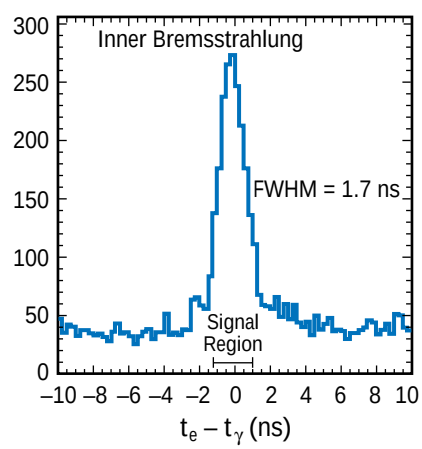

Fig. II-41. The timing spectrum that indicates the presence of coincidences of positrons and photons from the expected process $\mu^+ \to e^+\gamma\nu\nu$.

Figures II-38, II-39, II-42, and II-43 are a set. For the four primary variables that characterize the kinematics, these figures show the raw data (black), the expected signal based on Monte Carlo simulations (red), and the data cut tightly on the three other variables not displayed in the particular figure (blue). The structure in the uncut, relative-time spectrum is an artifact of the on-line filter; otherwise it would be flat. These figures allow the observation of several points. First, the evolution of the full spectrum to a few events is seen as the severe cuts are imposed to isolate the signal. Second, the number of events in the signal region is seen to be zero. Third, the distinct character of the signal is easily identified. Last, the proximity of candidates to the signal region can be evaluated.

The energies of photons and positrons for events that are within ±1.0 ns of being in coincidence and that have an angle between them of at least 178.1° are plotted in Fig. II-44. There are no events inside the box that indicates the signal region. The number of muon decays in the sample is 2.3×10^{13}. Taking Poisson statistics and the detector acceptance into account, a new limit for the branching ratio (90% confidence) for $\mu^+ \rightarrow e^+\gamma$ is established to be 4×10^{-11}. This value represents a slight improvement over the previous best limit of 5×10^{-11}, a result that was based on subtracting 50 events of background. These results are preliminary and may be improved by the imposition of cuts on kinematic properties not considered here; this work is in progress. It is hoped that when the remaining techniques for background reduction have been employed, the result for the remaining five-sixths of the data will be background-free and will get close to the desired sensitivity. Of course, the exciting possibility of actually observing a $\mu^+ \rightarrow e^+\gamma$ signal remains.

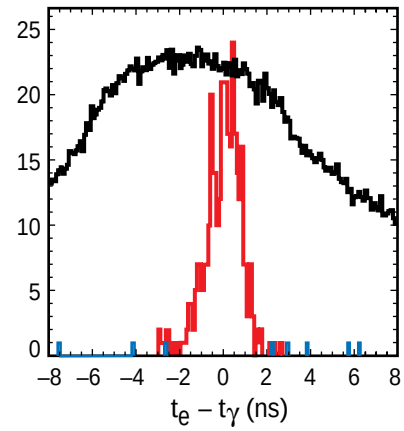

Fig. II-42. The relative timing spectrum at high rates is shown in black. The red curve is the signal expected for $\mu^+ \rightarrow e^+\gamma$ based on Monte Carlo simulations. The blue histogram contains the data with tight cuts on the angle between the particles, the positron energy, and the photon energy.

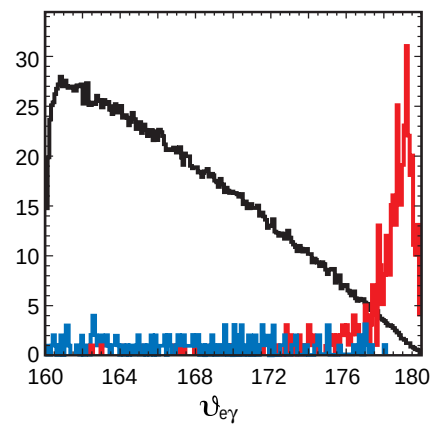

Fig. II-43. The spectrum of angles between the positron and photon at high rates is shown in black. The red curve is the signal expected for $\mu^+ \rightarrow e^+\gamma$ based on Monte Carlo simulations. The blue histogram contains the data with tight cuts on the time difference, the positron energy, and the photon energy.

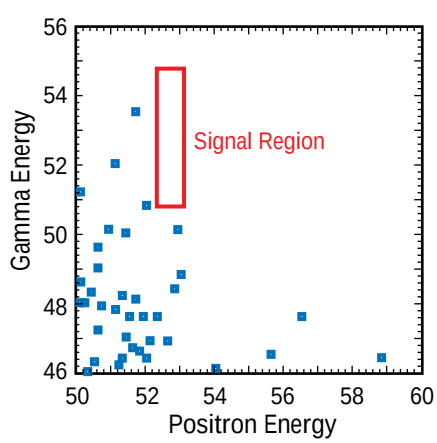

Fig. II-44. The photon energy plotted versus the electron energy for a set of events that are nearly back to back and in time coincidence. The empty box is where a potential $\mu^+ \rightarrow e^+\gamma$ signal should be.

NUSEA—Measurement of the Asymmetry in the Light-Antiquark Nucleonic Sea

M. J. Leitch, M. Brooks, T. Carey, G. Garvey, D. Lee, P. McGaughey, J. Moss, B. Park, J.-C. Peng, P. Reimer, W. Sondheim, N. Thompson (P-25), D. Isenhower, M. Sadler, R. Towell (Abilene Christian University), D. Geesaman, S. Kaufman, N. Makins, B. Zeidman (Argonne National Laboratory), C. Brown, B. Cooper (Fermi National Accelerator Laboratory), G. Petit, X. He, B. Lee (Georgia State University), D. Kaplan (Illinois Institute of Technology), P. Kirk, Y. Wang, Z. Wang (Louisiana State University), M. Beddo, T. Chang, G. Kyle, V. Papavassiliou, J. Webb (New Mexico State University), T. Awes, P. Stankus, G. Young (Oak Ridge National Laboratory), C. Gagliardi, B. Tribble, E. Hawker (Texas A&M University), D. Koetke, P. Nord (Valparaiso University)

Recent measurements of deep inelastic muon scattering by the New Muon Collaboration (NMC)[1] have suggested that the up sea antiquark ($\bar{u}_p$) and down sea antiquark ($\bar{d}_p$) distributions of the proton are not equal. The Gottfried sum rule,[2]

$$S_G = \int_0^1 (F_2^p(x) - F_2^n(x))dx / x$$
$$= \frac{1}{3} + \frac{2}{3}\int_0^1 (\bar{u}_p(x) - \bar{d}_p(x))dx,$$

says that the integral over the nucleon momentum fraction (x) of the difference of the structure functions for the proton (F_2^p) and the neutron (F_2^n) divided by x should be equal to one-third plus a term that is zero if the $\bar{u}_p$ and $\bar{d}_p$ distributions are equal. The NMC result for the Gottfried sum rule is $S_G = 0.235 \pm 0.026$. This result implies that $\bar{u}_p < \bar{d}_p$ in the proton.

One possible cause for an enhancement of $\bar{d}_p$ over $\bar{u}_p$ is Pauli blocking.[3] Here the idea is that because the proton is composed of two up quarks and a down quark (uud), it is less likely that a $u\bar{u}$ pair can be formed since the u would be blocked by the two up quarks in the proton more strongly than a d from a $d\bar{d}$ would be blocked by the single down quark in the proton. Another possible cause is from the pion-cloud model[4] of the proton. In this model the proton can produce pions in the cloud through mechanisms such as the following:

$$p \to p\pi^0 \Rightarrow p + \frac{1}{\sqrt{2}}(u\bar{u} + d\bar{d})$$
$$p \to n\pi^+ \Rightarrow n + (u\bar{d}).$$

Together, these mechanisms give more down antiquarks than up antiquarks.

A direct measurement of $\bar{u}_p$ and $\bar{d}_p$ can be made using the Drell-Yan (DY) process (Fig. II-45), in which a quark from an incident proton annihilates with a sea antiquark in a target nucleus and forms a virtual photon that then decays into a $\mu^+\mu^-$ pair. If this measurement is done on hydrogen and deuterium targets, then the following is true:

$$\left.\frac{\sigma_{p+d}(x)}{2\sigma_{p+p}(x)}\right|_{x_F>0} \cong \frac{1}{2}\left(1 + \frac{\bar{d}_p(x)}{\bar{u}_p(x)}\right),$$

where $\sigma_{p+p}(x)$ is the DY cross section for protons incident on hydrogen, and $\sigma_{p+d}(x)$ is the DY cross section for protons incident on deuterium. Using this process, the NA51 Collaboration[5] at the European Center for Nuclear Research obtained the result $\bar{u}/\bar{d} = 0.51 \pm 0.04 \pm 0.05$ at $x = 0.18$. The NUSEA experiment E866 at Fermilab, which we report on here, has measured the deuterium to hydrogen ratio in the DY process over values of x ranging from 0 to 0.3. This range is much wider than that of the NA51 experiment, and

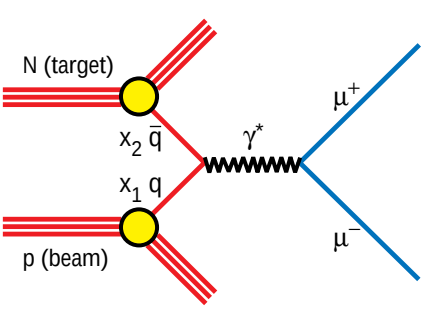

Fig. II-45. Diagram of the Drell-Yan process.

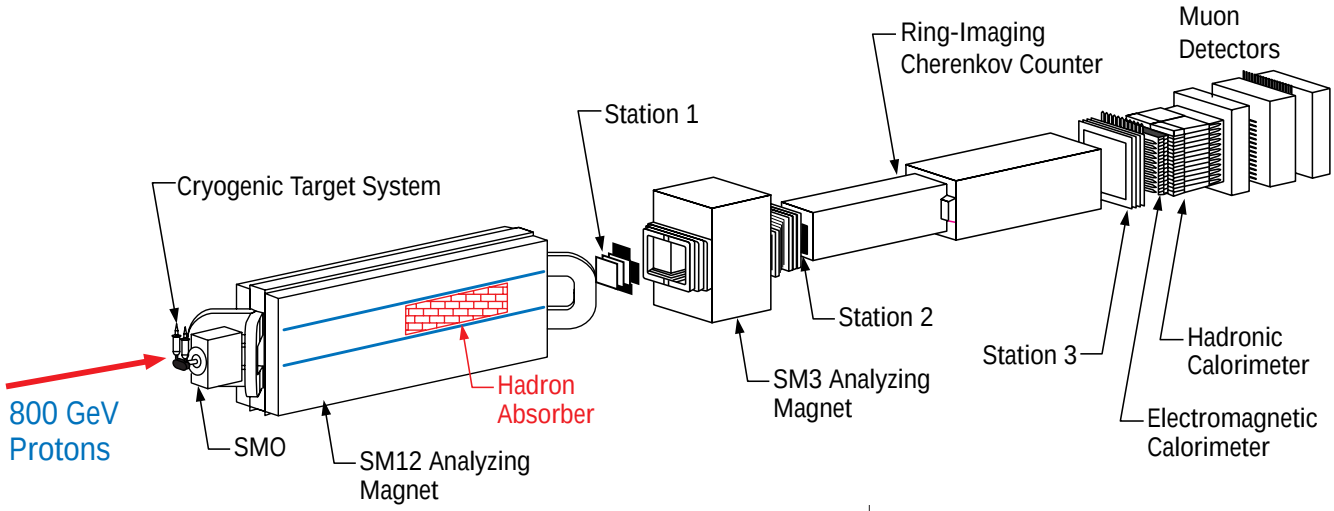

Fig. II-46 Schematic view of the NUSEA pair spectrometer.

the NUSEA experiment has over 350,000 events recorded, compared with NA51's 6,000 events. Los Alamos personnel are leaders in the NUSEA experiment and in two previous experiments, E772 and E789; all three experiments used the same spectrometer. The earlier experiments studied nuclear effects on dimuon production and the production of *D* and *B* mesons. Pat McGaughey, from Los Alamos, is the spokesperson for the NUSEA Collaboration.

The NUSEA pair spectrometer (Fig. II-46), which is on one of the 800 GeV/*c* proton beam lines at Fermilab, detects $\mu^+\mu^-$ pairs for very high incident-proton intensities (≈10^{11} protons/s). Two 20-in.-long cryogenic targets, one filled with liquid hydrogen and the other with liquid deuterium, and an empty cryogenic vessel are located just upstream of the first magnet. On alternate 20-second beam spills, the target intercepting the beam is changed from deuterium to hydrogen to empty. The portion of the beam that does not interact with the targets is stopped in a 168-in.-long copper beam dump. Opposite-sign muon pairs are bent vertically above and below the beam dump by the first two magnets (SM0 and SM12) and are tracked through a series of scintillator hodoscopes and drift chambers before and after the last bending magnet (SM3). Using the hits in the drift chambers, we measure the bend angle in SM3 and, from this angle, determine the momentum of each muon. Then the muon tracks are traced backwards through the known magnetic field of SM12 and SM0, and the muons' momenta and direction at the target are reconstructed. Thick absorber walls both in SM12 and in front of a set of hodoscopes and proportional tube detectors assure that all of the tracked particles are muons because hadrons or electrons would not penetrate the absorbers. Finally, the pair mass is reconstructed from the tracks at the target.

A 6-month-long measurement of $\bar{u}/\bar{d}$ has just been completed, and analysis of the data is well under way. We present our preliminary results here. Data were taken at three magnetic-field settings that emphasized high, intermediate, and low masses. Figure II-47 shows the combined mass spectra for the three mass settings as well as that for the high-mass setting alone. In addition to the continuum DY

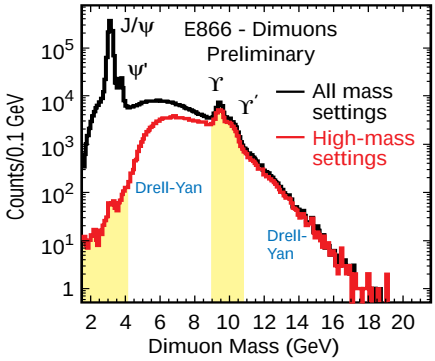

Fig. II-47. Dimuon mass spectra obtained in the NUSEA experiment. The black curve shows the composite spectra for the three mass settings, while the red curve shows the spectrum for the high-mass setting alone. Only the unshaded regions for the high-mass setting are used in the preliminary analysis presented here. The shaded regions were not used so that only DY would be included and all contributions from the resonance mass peaks excluded.

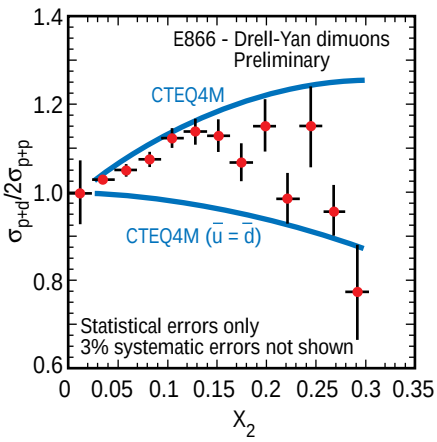

Fig. II-48. Preliminary results from the NUSEA experiment for the ratio of the deuterium cross section divided by two times the hydrogen cross section ($\sigma_{p+d}/2\sigma_{p+p}$) plotted versus the target momentum fraction (x_2) of the sea antiquark.

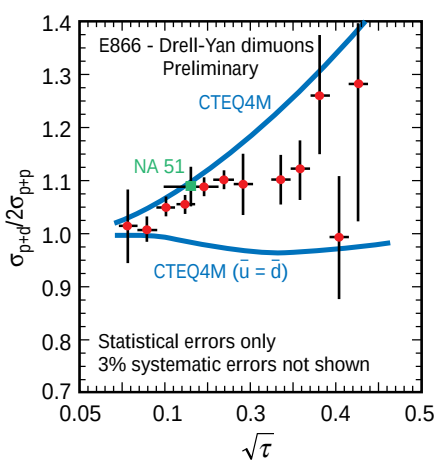

Fig. II-49. The same ratio seen in Fig. 4 plotted versus $\sqrt{\tau}$, where $\tau = x_1x_2$. The single data point from the NA51 experiment is shown along with the NUSEA data.

muon pairs, one also sees peaks corresponding to production and decay of the J/Ψ, Ψ', and Υ, and Υ' resonances. For the $\bar{u}/\bar{d}$ analysis that follows, we excluded the mass regions corresponding to these resonances. Preliminary results for the ratio of deuterium to hydrogen versus x, obtained from an analysis of most of the data for our high-mass setting, are shown in Fig. II-48. Results are not yet available for the other mass settings because of the need to correct for rate-dependence effects that are not present in the high-mass data. Also shown are theoretical calculations with phenomenological CTEQ4M[6,7] structure functions and a calculation based on CTEQ4M but with $\bar{u} = \bar{d}$. The former fixes its $\bar{u}/\bar{d}$ asymmetry from the NMC and NA51 data. In Fig. II-49 we plot the ratio versus $\sqrt{\tau}$, where $\tau = x_1x_2$, and x_1 and x_2 are the beam and target momentum fractions, respectively. Here the NA51 data point is seen to be consistent with our data.

As the analysis of our NUSEA data progresses and data from the other two magnetic-field settings are incorporated into our results, we will have a direct and accurate measurement of the $\bar{u}/\bar{d}$ asymmetry over a wide range of x. At the present our preliminary analysis confirms that $\bar{d}$ is enhanced over $\bar{u}$ when x is in the range of 0–0.2. Below about $x = 0.2$ our results agree well with the CTEQ4M theoretical result, but at higher x they fall substantially below it.

In addition to the $\bar{u}/\bar{d}$ asymmetry measurement, NUSEA has been approved for an extension during which we will address a number of issues, including many that relate to our future studies at the Relativistic Heavy-Ion Collider. We will measure the polarization of DY pairs and of J/Ψ resonances to try to better understand their production mechanisms, notably whether the J/Ψ resonances are initially produced in a color-octet state.[8] We will also measure the nuclear dependence of J/Ψ production near zero and at very large x_F (where $x_F = x_1 - x_2$) in order to better determine the most important nuclear effects in p-A reactions. Finally, we will study DY pairs at masses below the J/Ψ resonances and try to understand the different contributions to the continuum at these low masses.

References

1. M. Arneodo et al. (New Muon Collaboration), "Reevaluation of the Gottfried Sum," *Physical Review D* **50**, R1 (1994).

2. K. Gottfried, "Sum Rule for High-Energy Electron-Proton Scattering," *Physical Review Letters* **18**, 1174 (1967).

3. R. D. Field and R. P. Feynman, "Quark Elastic Scattering as a Source of High-Transverse Momentum Mesons," *Physical Review D* **15**, 2590 (1977).

4. A. Szczurek et al., "Testing the Meson Cloud in the Nucleon in Drell-Yan Processes," *Nuclear Physics A* **596**, 397 (1996).

5. A. Baldit et al. (NA51 Collaboration), "Study of the Isospin Symmetry Breaking in the Light Quark Sea of the Nucleon from the Drell-Yan Process," *Physics Letters B* **332**, 244 (1994).

6. H. L. Lai et al., "Global QCD Analysis and the CTEQ Parton Distributions," *Physical Review D* **51**, 4763 (1995).

7. H. L. Lai et al., "Improved Parton Distributions from Global Analysis of Recent Deep-Inelastic Scattering and Inclusive Jet Data," to be published in *Physical Review D*.

8. E. Braaten and S. Fleming, "Color-Octet Fragmentation and the Ψ' Surplus at the Fermilab Tevatron," *Physical Review Letters* **74**, 3327 (1995).

Neutrino Oscillation Results from the Liquid Scintillator Neutrino Detector

W. C. Louis, R. L. Burman,
F. J. Federspiel, G. T. Garvey,
G. B. Mills, V. Sandberg, R. Tayloe,
D. H. White (P-25),
J. B. Donahue (LANSCE-7),
collaborators from
University of California at Riverside,
University of California at San Diego,
University of California at Santa Barbara,
Embry-Riddle Aeronautical University,
University of California Intercampus Institute for Research at Particle Accelerators,
Linfield College,
Louisiana State University,
Louisiana Tech University,
University of New Mexico,
Southern University,
and Temple University

In the past few years, a number of experiments have searched for neutrino oscillations, in which a neutrino of one type (such as $\bar{\nu}_\mu$) spontaneously transforms into a neutrino of another type (such as $\bar{\nu}_e$). In the standard model of particle physics, neutrinos are considered to be massless, but the existence of neutrino oscillations would imply that neutrinos actually do have mass. Neutrino mass of even a few electronvolts would profoundly affect theories related to cosmology and to the development of structure in the universe.

In 1995 the LSND (Liquid Scintillator Neutrino Detector) collaboration published data showing candidate events that are consistent with $\bar{\nu}_\mu \rightarrow \bar{\nu}_e$ oscillations.[1] Since then, the collaboration has reported additional data that provide stronger evidence for neutrino oscillations.[2,3] The LSND results complement hints from solar and atmospheric neutrino experiments that neutrino oscillations occur. In the solar experiments the sun emits fewer neutrinos than the standard solar model predicts, and in the atmospheric experiments the ratio of muon neutrinos to electron neutrinos that are generated by cosmic-ray interactions in the upper atmosphere is unexpectedly low. This current neutrino data combined with data from future experiments may eventually allow physicists to determine the masses and mixings of all three flavors of neutrinos.

The LSND experiment at the Los Alamos Neutron Scattering Center (LANSCE)[4] is a high-sensitivity search for $\bar{\nu}_\mu \rightarrow \bar{\nu}_e$ oscillations from μ^+ decay at rest. With its 1-mA proton intensity and 800-MeV energy, LANSCE is an intense source of low-energy neutrinos. The LANSCE neutrino source is well understood[5,6] because almost all neutrinos arise from π^+ or μ^+ decay; π^- and μ^- are readily captured in the iron of the shielding and the copper of the beam stop. The

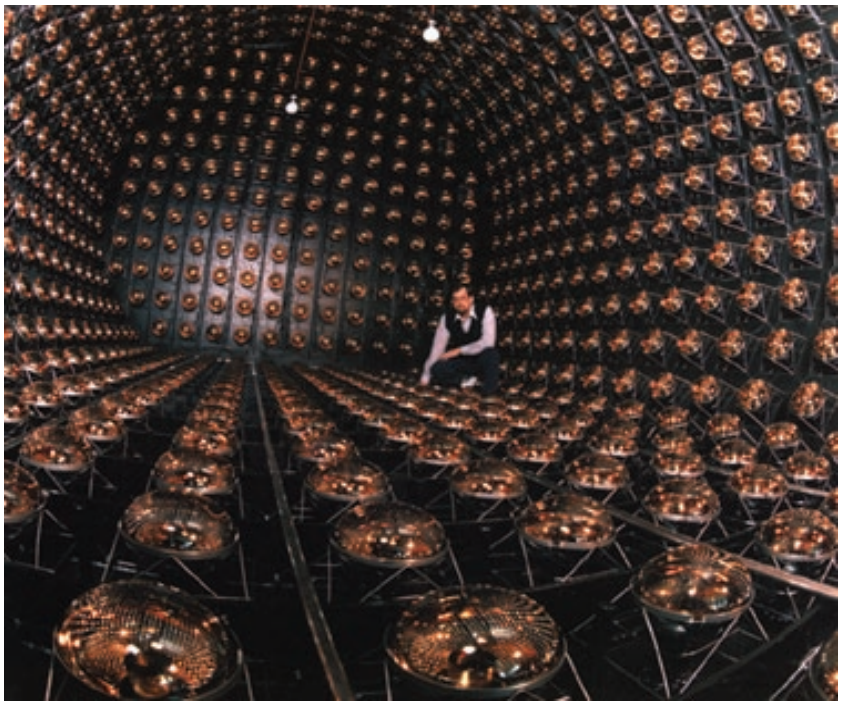

Fig. II-50. An interior view of the LSND detector, showing a portion of the 1,220 phototubes that cover the inside surface.

production of kaons and heavier mesons is negligible at the 800-MeV LANSCE energy. In the 36- to 52.8-MeV energy range, the ratio of $\bar{\nu}_e$ to $\bar{\nu}_\mu$ is calculated to be only 4×10^{-4}, so the observation of a significant $\bar{\nu}_e$ rate would be evidence for $\bar{\nu}_\mu \rightarrow \bar{\nu}_e$ oscillations.

The LSND detector consists of a cylindrical tank, 8.3 m long by 5.7 m in diameter, surrounded by a veto shield[7] that detects cosmic-ray muons going through the detector. The center of the detector is 30 m from the neutrino source. Mounted on the inside surface of the tank are 1,220 Hammamatsu phototubes (8 in. each), which cover 25% of the surface. These phototubes can be seen in Fig. II-50, a photograph of the inside of the LSND detector. The tank is filled with 167 metric tons of liquid scintillator, which consists of a small concentration of the organic compound butyl PBD in mineral oil. Because of the low scintillator concentration, both Cerenkov light and scintillation light can be detected, and a relatively large attenuation length of more than 20 m occurs for wavelengths greater than 400 nm.[8] A typical 45-MeV electron created in the detector produces approximately 1500 photoelectrons, of which around 280 are in the Cerenkov cone. The phototube time and pulse-height signals are used to reconstruct the electron and positron tracks with an average rms position resolution of ~30 cm, an angular resolution of ~12°, and an energy resolution of ~7%. The Cerenkov cone for relativistic particles and the time distribution of the light (broader for nonrelativistic than for relativistic particles) provide excellent particle identification.

The signature for a $\bar{\nu}_e$ interaction in the detector is the reaction $\bar{\nu}_e p \rightarrow e^+ n$. The recoil neutron, n, then undergoes the reaction $np \rightarrow d\gamma$, in which γ is a correlated 2.2-MeV photon. To distinguish between a correlated photon and a photon that is accidentally coincidental, we use a likelihood ratio, R, which is the probability that the photon is correlated divided by the probability that it is accidental. The ratio depends on the number of phototubes that the photons have hit, the reconstructed distance between the photon and the positron, and the relative time between the photon and the positron. Figure II-51 shows the R distribution for events with positrons in the energy range of 20–60 MeV, where an event is defined as the primary positron and any associated photons. The R distribution yields a range of 26.9–78.5 excess events after beam-off background is subtracted from beam-on readings; this range includes statistical and systematic errors. If these excess events are due to neutrino oscillations, then the oscillation probability, including statistical and systematic errors, is in the range of 0.14%–0.43%. With such a small probability, it is not surprising that neutrino oscillations are difficult to detect.

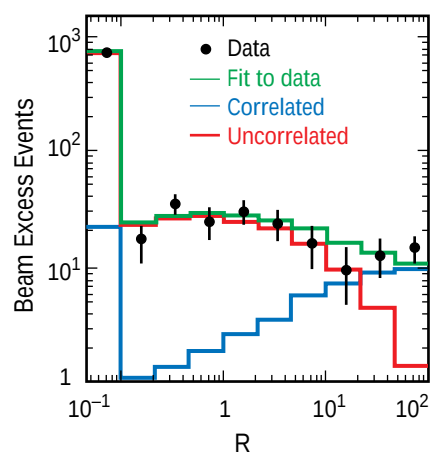

Fig. II-51. The R distribution for events with positron energies in the range of 20–60 MeV. Shown are the total fit to the data (green), the component of the fit with uncorrelated photons (red), and the component with correlated photons (blue). High values of R indicate a high probability that a photon is correlated.

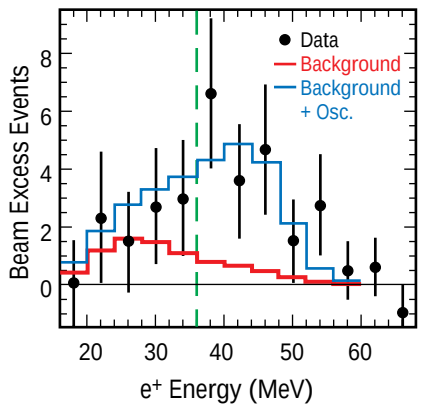

Fig. II-52. The positron energy distribution for events with R>30. Shown are the beam-excess data, estimated background from all neutrino reactions (red), and neutrino background plus the expected distribution for neutrino oscillations at asymptotically large Δm^2 (blue).

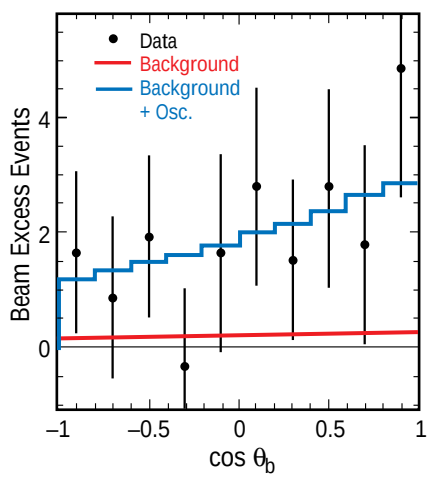

Fig. II-53. The angular distribution for events with R>30, where θ_b is the angle between the positron direction and incident neutrino direction.

Fig. II-54. The 90% and 99% likelihood regions of Δm^2 vs $\sin^2\theta$ for the LSND experiment, including systematic errors. Also shown are the 90% confidence level limits from KARMEN at ISIS, E776 at BNL, and Bugey reactor experiments; their 90% likelihood regions lie to the left of the limits.

Figures II-52 and II-53 show the positron energy and angular distributions (with beam-off background subtracted) for events that have an associated photon with R>30. If R is greater than 30, the total efficiency of detecting 2.2-MeV photons is 23%, and the probability that an event has an accidental photon in coincidence is 0.6%. In the 36- to 60-MeV energy range, a range chosen because it has little background from known neutrino interactions, there are 22 beam-on events and a total estimated background range of 4.0–5.2 events; the total estimated background includes beam-off background and known neutrino-induced interactions. The probability that this excess of beam-on events is a statistical fluctuation is less than 10^{-7}.

If neutrino oscillations cause the observed excess, then Fig. II-54 shows the allowed region (90% and 99% likelihood regions) of $\sin^2 2\theta$ plotted against Δm^2. This plot is a maximum likelihood fit to the excess events, where θ is the mixing angle and Δm^2 is the difference between the squared masses of the two neutrino mass eigenstates. For this plot to have meaning, neutrinos must have mass, and furthermore, different flavors of neutrinos must have different masses. Also shown in Fig. II-54 are the 90% confidence limits from the ongoing KARMEN neutrino experiment at the spallation neutron source ISIS,[9–11] the E776 experiment at Brookhaven National Laboratory,[12] and the Bugey reactor experiment.[13] To the left of these limits are the 90% likelihood regions. If we consider the regions from all four experiments, the most favored region has a Δm^2 of approximately 0.2–2 eV^2/c^4.

By acquiring additional data from the experiment and studying the performance of the LSND detector, we expect to improve our understanding of the phenomena described in this article, and we hope eventually to settle the issue of whether neutrino oscillations exist.

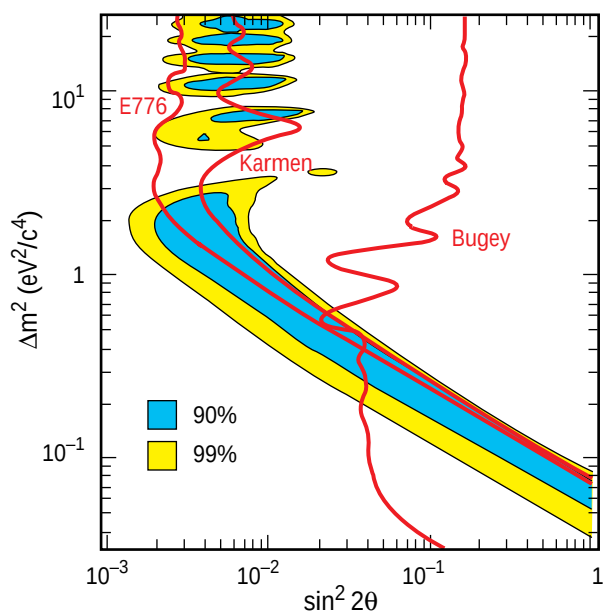

References

1. C. Athanassopoulos et al., "Candidate Events in a Search for $\bar{\nu}_\mu \rightarrow \bar{\nu}_e$ Oscillations," *Physical Review Letters* 75, 2650 (1995).

2. C. Athanassopoulos et al., "Evidence for $\bar{\nu}_\mu \rightarrow \bar{\nu}_e$ Oscillations from the LSND Experiment at the Los Alamos Meson Physics Facility," *Physical Review Letters* **77**, 3082 (1996).

3. C. Athanassopoulos et al., "Evidence for Neutrino Oscillations from Muon Decay at Rest," *Physical Review C* **54**, 2685 (1996).

4. C. Athanassopoulos et al., "The Liquid Scintillator Neutrino Detector and LAMPF Neutrino Source," *Nuclear Instruments and Methods in Physics Research A* **388**, 149 (1997).

5. R. L. Burman, M. E. Potter, and E. S. Smith, "Monte Carlo Simulation of Neutrino Production by Medium-Energy Protons in a Beam Stop," *Nuclear Instruments and Methods in Physics Research A* **291**, 621 (1990).

6. R. L. Burman, A. C. Dodd, and P. Plischke, "Neutrino Flux Calculations for the ISIS Spallation Neutron Facility," *Nuclear Instruments and Methods in Physics Research A* **368**, 416 (1996).

7. J. J. Napolitano et al., "Construction and Performance of a Large Area Scintillator Cosmic Ray Anticoincidence Detector," *Nuclear Instruments and Methods in Physics Research A* **274**, 152 (1989).

8. R. A. Reeder et al., "Dilute Scintillators for Large-Volume Tracking Detectors," *Nuclear Instruments and Methods in Physics Research A* **334**, 353 (1993).

9. B. Bodmann et al. (KARMEN Collaboration), "First Observation of the Neutral Current Excitation $^{12}C(\nu,\nu')^{12}C^*(1^+,1)$," *Physics Letters B* **267**, 321 (1991).

10. B. Bodmann et al. (KARMEN Collaboration), "Cross Section of the Charged Current Reaction $^{12}C(\nu_e,e^-)^{12}N_{g.s.}$," *Physics Letters B* **280**, 198 (1992).

11. B. Zeitnitz et al. (KARMEN Collaboration), "KARMEN: Neutrino Physics at ISIS," *Progress in Particle and Nuclear Physics* **32**, 351 (1994).

12. L. Borodovsky et al., "Search for Muon-Neutrino Oscillations $\nu_\mu \rightarrow \nu_e$ $(\bar{\nu}_\mu \rightarrow \bar{\nu}_e)$ in a Wide-Band Neutrino Beam," *Physical Review Letters* **68**, 274 (1992).

13. B. Achkar et al., "Search for Neutrino Oscillations at 15, 40, and 95 Meters from a Nuclear Power Reactor at Bugey," *Nuclear Physics B* **434**, 503 (1995).

Proton Radiography

*J. B. McClelland, J. Amann,
J. Boissevain, C. Espinoza, J. Gomez,
G. Hart, G. Hogan, C. Morris,
C. Reidel, H. A. Thiessen, H. Ziock,
J. Zumbro (P-25),
K. Alrick, F. Cverna, R. Gallegos,
N. Gray, V. Holmes, S. Jaramillo,
N. King, K. Morley, P. Pazuchanics,
G. Yates (P-23),
D. Flicker, A. Mathews, J. Sarracino,
P. K. Tang (XNH),
K. Adams (XTM),
P. Ginsberg (DX-1),
R. London (DX-3),
H. L. Stacy (DX-4),
T. Fife (DX-5),
H. E. Tucker (DX-6),
C. T. Mottershead (LANSCE-1),
B. E. Takala (LANSCE-3),
F. Merrill, C. Pillai,
L. Rybarcyk (LANSCE-6),
S. Cushing (LANSCE-7),
S. Balzer, P. Flores,
R. T. Thompson (Bechtel Nevada),
collaborators from ESA Division and
Lawrence Livermore National
Laboratory*

Introduction

Protons can be used to probe with high spatial and temporal resolution the interior structure of systems that are static, imploding, or exploding. Protons have already been used to image thin systems, but the technique was limited by the image blurring caused in the object by the multiple scattering of the protons. The new development coming out of Physics Division is the introduction of a magnetic-lens system to remove much of this blur. Also, we are extending this technique further to gain information on the material composition of the object being probed by allowing a second detection of the transmitted protons through a reduced aperture. Experiments have been performed at the Los Alamos Neutron Scattering Center (LANSCE) and the Alternating Gradient Synchrotron (AGS) at Brookhaven National Laboratory (BNL) to confirm many of the concepts of proton radiography. A three-year program has begun to demonstrate the capabilities of proton radiography as a tool for advanced hydrotesting of nuclear-weapons primaries using high-energy (50-GeV) protons. A program at LANSCE is starting, using 800-MeV protons as a research tool for Science-Based Stockpile Stewardship (SBSS), looking at shock-wave propagation in high-explosive (HE) systems.

The SBSS Program and the Stockpile Stewardship and Management Program were developed to assure the reliability and safety of the weapons in the enduring stockpile without the use of nuclear testing. Effects that will need to be addressed will arise due to aging of components, remanufacture of weapons and weapon components, or possible packaging changes. In the past, such effects often were assessed with nuclear testing. As part of this comprehensive program to understand the fundamental physics of a nuclear device through modeling and nonnuclear experiments, the integral performance of a nuclear assembly must be measured with substantially improved fidelity. An advanced radiographic capability is an essential component of this program, providing the ability to measure the integral performance of stockpiled primaries using inert materials and thereby derive nuclear performance information that previously could only be obtained from nuclear testing. Detailed data from these hydrodynamic experiments are the necessary starting points for modeling the explosion phase of the primary and thus for assessing the performance and safety of stockpiled primaries.

The primary is the most difficult component of a nuclear weapon to assess for reliability because changes, though small, have the potential to affect the boost process. Three of the most important parameters affecting primary boost and thus yield performance are the level of supercriticality produced by HE compression, the shape of the boost cavity, and mix within the cavity. For assessing nuclear safety in an accident, the integral of the level of supercriticality over of time must be determined. Hydrodynamic testing is the only available tool for measuring the integral performance of a primary up to the beginning of criticality. Currently, pin measurements (wherein electrical pins of varying lengths are arrayed inside of a primary or primary surrogate and are progressively shorted out as the primary implodes) and radiography of an imploded pit and cavity are used to constrain computational simulations from which nuclear performance and safety are calculated. In the absence of nuclear testing, it is essential that hydrotest capabilities be expanded to include experimental validation of calculated nuclear performance. A multiaxis (>2 axes), multipulse, radiographic system does not currently exist, and none is anticipated for the near future. The Advanced Hydrotest Facility (AHF) is being proposed to meet this challenge.

Hydrodynamic radiography refers to that technology used to view inside thick material objects (specifically the primaries of nuclear weapon assemblies) as they are undergoing implosion and compression because of the detonation of surrounding HE. The principal tool of hydrotesting is thick-object-penetrating radiography. The images obtained must be formed very quickly (in ~50 ns or less) to freeze the motion of the moving components and features and to avoid motion blur. The images are negatives, in that the information depicting the primary assembly's internal structure is obtained from the attenuation of the penetrating radiation. Current state-of-the-art facilities are PHERMEX at LANL and FXR at Lawrence Livermore National Laboratory (LLNL). Both are important elements of current stockpile maintenance, and efforts are continuing to upgrade their capabilities through double pulsing and enhanced detector capability. These two facilities will remain the prime radiographic facilities until the completion of the Dual Axis Radiographic Hydrotest (DARHT) facility in FY 1999 (for the first axis) and FY 2002 (for the second axis). DARHT will improve radiographic resolution and x-ray intensity (dose) and provide dual-axis tomographic data to evaluate asymmetries in primary assemblies. It will also provide improved data for the development of the analysis tools that will be needed for the proposed AHF. The AHF is proposed to provide improved understanding of three-dimensional effects associated with aging and weaponization features of weapons and to provide time-dependent, high-resolution measurements of pit density and gas-cavity configurations. It would expand multipulsed, multiaxis capabilities well beyond those being planned for DARHT.

An advanced radiographic capability will have to provide accurate information about densities and material positions, from which we can infer the degree of supercriticality, the shape of the boost cavity, and the mix that would be present in an actual imploding primary. Allowed manufacturing tolerances can cause an implosion to be three dimensional even in normal operation, and accidental detonations are almost always three dimensional. As a result, radiographs are needed from a number of directions (at least 4 and preferably 12) so that material densities can be reconstructed with accuracies sufficient to derive nuclear parameters. Also, since the implosion progresses with time, a temporal series of radiographs (5–10) is needed over a time period relevant to the processes being recorded. This time window may need to cover a period as long as the full implosion. Two radiation species are under consideration as possible advanced technologies for an AHF: multi-MeV x-rays and multi-GeV protons. The overall utility and performance of both types of radiation will be studied to select an optimal technology mix.

In x-ray radiography, a beam of energetic electrons is accelerated and then focused onto a dense, high-atomic-number material target, producing bremsstrahlung x-rays. The necessary penetrating dose requires many kiloamperes of electron beam current with >10 MeV of kinetic energy impinging on a converter target located about a meter from the hydrodynamic object. To resolve small feature-sizes within a weapon-primary assembly, the x-ray source must be a very small spot size (approaching a point source) thus requiring a very-small-diameter electron beam. There are two technology paths under consideration for x-ray hydrodynamic radiography: linear induction accelerators (LIAs) and inductive voltage adders (IVAs). The LIA approach uses a single high-voltage, high-transport-current (20- to 40-MeV, 1- to 6-kA), large accelerator producing a long-duration electron beam that is distributed via a kicker into many axes, each of which transports a shorter-duration beam to a bremsstrahlung converter. The IVA approach uses smaller medium-voltage, higher-current (12-MeV, 40-kA), individual accelerators to directly generate the short-duration pulses that are delivered to the bremsstrahlung converters.

In proton radiography, a high-energy beam of protons impinges directly on the object to be radiographed. There is no need for an equivalent bremsstrahlung converter since the proton beam directly illuminates the primary assembly. Unlike x-rays, protons undergo a large number of very forward-angle scatterings as they pass through the object and the exit window of the containment vessel. This introduces a blur to the image that is then removed, for the most part, by a magnetic lens system between the object and the detectors. The residual blurring can be further reduced by increasing the energy of the proton beam. For typical weapon-primary assemblies and containment-window thicknesses, this corresponds to proton beam energies near 50 GeV. The proton beam is produced in conventional accelerator architectures, including an injection linac and synchrotron ring. The inherent time structure of the acceleration process lends itself naturally to the variable pulse formats needed for advanced radiography. Each pulse in the ring is of short duration (less than 50 ns), with many pulses present in the ring. A kicker system is used to deliver the required pulse format, both the pulse spacing and the total duration of the pulse train. Each pulse can then be split into multiple pulses and delivered simultaneously to the object through multiple beamlines. The number of protons in a single pulse must be adequate to meet the density and field-of-view requirements. At the present time, it is estimated that 5×10^9 protons per pulse per axis are needed. With 10 axes, this would imply 5×10^{10} protons per pulse. Considerably more intensity is available with current technologies (over 10^{13} at the AGS at BNL and the proton storage ring [PSR] at LANSCE), so that higher fluxes are available if warranted by refinements in the radiographic requirements. Figure II-55 is a schematic of a proton-based AHF, showing the injection linac, 50-GeV ring, beam distribution system, firing point, and lens system.

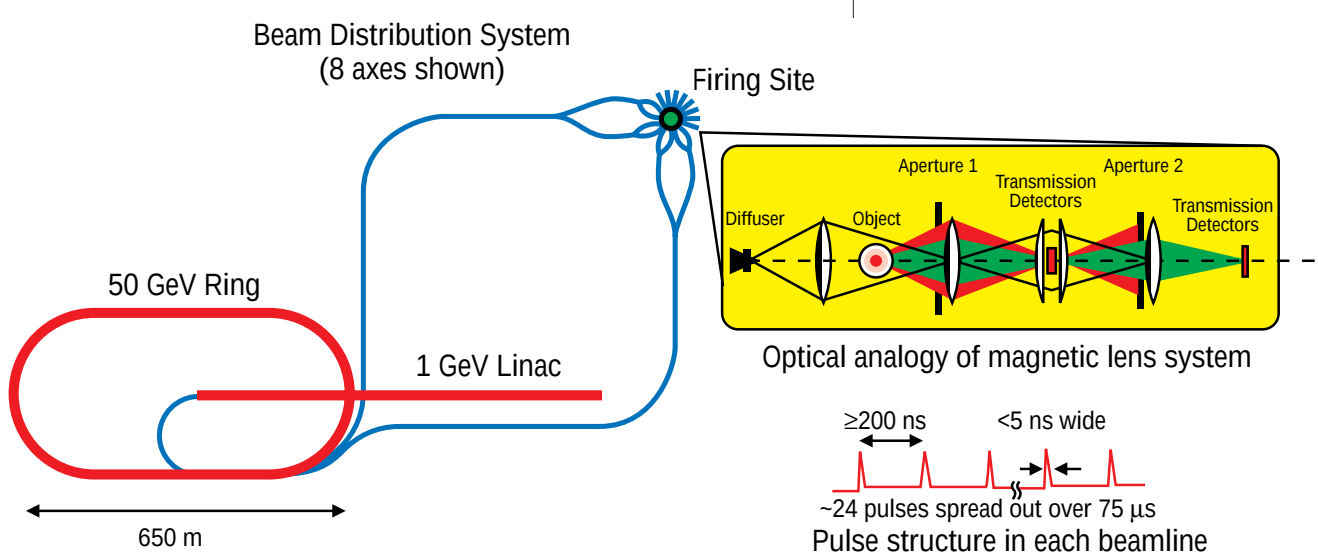

Fig. II-55. Schematic of a proton-based Advanced Hydrotest Facility.

Proton Radiography

Proton radiography marks a sharp departure from flash x-ray technology, which has been the exclusive radiographic tool for stockpile support for more than thirty years. Here, the primary proton beam of a suitably high energy (near 50 GeV) is used to image the imploding object directly. Both the nuclear attenuation and the multiple scattering of the protons contain information on the distribution and composition of materials in the object. The principle virtues of protons are (1) the relatively long mean-free-paths of protons, well matched for the imaging of dense objects, (2) the maturity of proton-accelerator technology, which can accommodate the multiaxis, multipulse format required for an AHF, (3) lack of significant scattered background in the final image, (4) sensitivity to both material density and composition, (5) direct utilization of the proton beam as the radiographic probe, (6) high detection efficiency, (7) high reliability because the beam is coasting in the storage ring before the time of firing, and (8) the ability to easily deliver a test beam in advance of firing. The capabilities of proton radiography will likely exceed the current AHF requirements in several categories, providing a great deal of flexibility for enhancing future AHF capabilities. What is mostly wanting for protons at this time is radiographic experience with weapons-relevant dynamic systems. Common to both protons and x-rays is the need for fast, large-format, pixelated detectors; simulation capabilities to better understand the performance of the full radiographic system; and the facility issues related to practical problems of actually making the required measurements.

800-MeV SBSS Research Tool

We can use 800-MeV protons to radiograph dynamic systems with areal densities up to 20 g/cm^2 for low-Z materials using intensities available from the LANSCE linac, typically 2×10^9 protons per 40-ns pulse. This capability is well suited for studies of HE shock propagation. A dynamic radiographic system has been installed in Line B at LANSCE, including a beam transport system, imaging lens, multiframe detection system, and containment system. LLNL is collaborating on this project and has been involved in simulations and detector development. The first experiments have looked at shock propagation in HE hemispheres and have also explored cylindrical geometries. The major issues to be addressed are how the shock from the detonator propagates through the HE and which parts of the HE react as a function of HE properties and temperature.

Figure II-56 shows the measured spatial resolution of the LANSCE apparatus. A metal "comb" with 1- and 2-mm-spaced slots was radiographed. The fitted position resolution was found to be better than 0.5 mm full width at half maximum (FWHM).

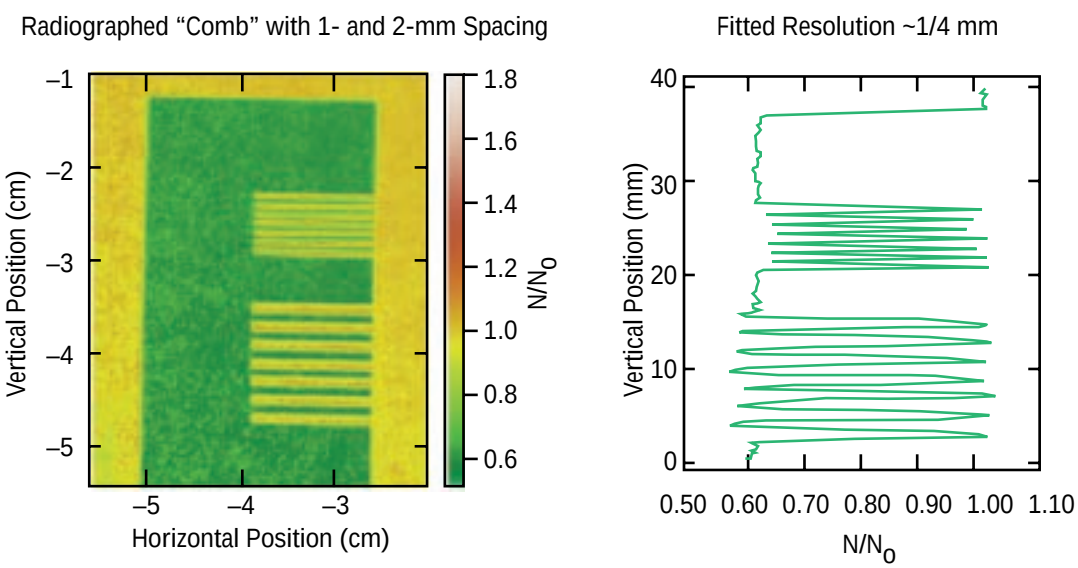

Fig. II-56. Measured resolution of the LANSCE proton-radiography apparatus.

Figure II-57 shows a detonation wave at four different times in an HE assembly. The assembly consists of two embedded hemispheres of high explosives with a detonator. The inner shell is normal HE and the outer shell is insensitive high explosive (IHE). The diameter of the outer shell is approximately 5.7 cm, with a total HE mass of 92 g. The dotted line represents the edge of the unreacted HE. The propagation of the detonation wave is clearly evident in the radiographs as it propagates from the detonator to the outer surface of the IHE. What is shown is actually the ratio of the dynamic radiograph to a radiograph of the object taken before detonation. This enhances the changes visible in the dynamic radiograph. The images were recorded on a phosphor image plate that allows for one image per shot. An active camera system has now been installed, which is capable of taking up to six frames during the time of a single HE explosion.

The limitations to thin, low-Z systems at 800 MeV come primarily from multiple scattering within the object and aberrations in the lens system. Both of these effects become less important as the beam energy goes up, so these are not basic limitations for weapons-geometry hydrotests. A beam energy of approximately 50 GeV would be adequate to achieve 1% density measurements on a 1-mm^2 pixel size, with submillimeter resolutions for thick, dense systems (several hundred g/cm^2).

It is possible to overcome some of the limitations at 800 MeV by reducing the aperture in the lens through which the transmission is measured. This reduces the effects of chromatic aberrations in the lens. However, this also reduces the transmitted intensity, and hence, the sensitivity of the measurement. By using the beam from the PSR at LANSCE, the initial intensity of the pulse can be increased by four orders of magnitude, since 2×10^{13} protons are stored in a PSR pulse. A

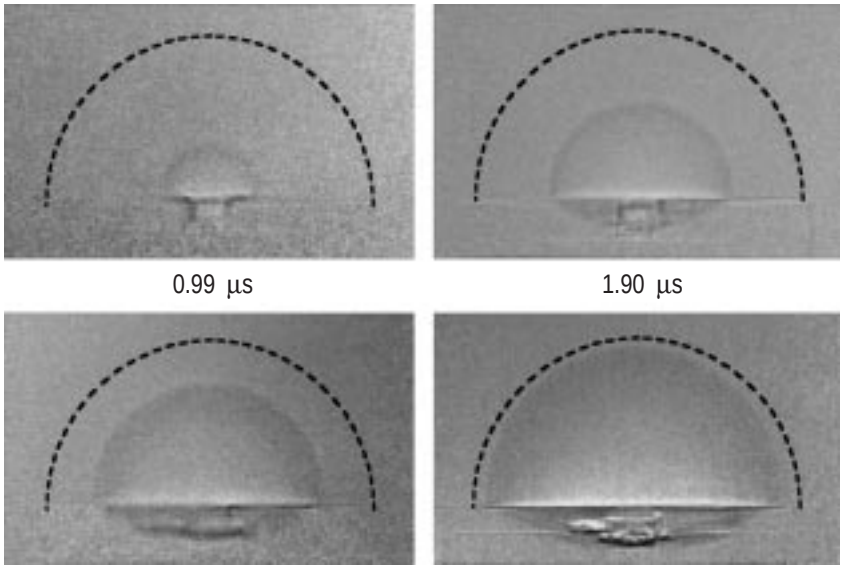

Fig. II-57. Proton radiographs of shock propagation at four different times in an HE assembly.

development has been recently completed where the PSR pulse was split into two pulses separated by 360 ns, each pulse being less than 50 ns wide. The PSR is being upgraded to store three pulses at full intensity. By using this splitting technique, 6 pulses could be extracted from the PSR and delivered to a firing site to radiograph thicker (100 g/cm^2) higher-Z dynamic systems. A study was recently completed that showed how to marry the higher-intensity 800-MeV proton radiography capability with neutron resonance spectroscopy, which can measure temperature and velocity in materials, in one facility at LANSCE.

Advanced Hydrotest Capability

Protons are one of three technology options being considered for an AHF. Recently, the three weapons program directors from LANL, LLNL, and Sandia National Laboratories (SNL) requested a technology development plan that would demonstrate over a three-year period the viability of the three technologies. LANL was designated the coordinating laboratory for protons, LLNL for LIAs, and SNL for IVAs. Technical Contracts, modeled after the Nova Technical Contracts for NIF, have been drafted that define the critical issues to be addressed, together with the tasks and goals, and Implementation Plans with cost and schedule information for accomplishing the Technical Contracts have been completed, as well as an additional contract covering physics requirements. Work began in FY97 toward these objectives. LLNL is now collaborating with LANL on proton radiography, and all planning is being done jointly with them.

The 3-year plan addresses the following critical issues for proton radiography:

- demonstration of proton radiography performance on a suitable array of test objects under conditions as near as possible to the anticipated design parameters of an AHF;
- development of instrumentation capable of meeting the AHF requirements for spatial and temporal resolutions and required pulse format;
- demonstration of a proton-accelerator concept capable of meeting AHF requirements;
- examination of the effects of the confinement system on resolution and of its interfacing to the lens system; and
- demonstration, in conjunction with the physics requirements modeling effort, that uncertainties in the radiographic image, after correction for known experimental effects, are consistent with criticality, cavity shape, and mix physics-data requirements.

One of the major experimental efforts of this plan is to construct a new beamline at the AGS at BNL to accept up to eight pulses of 25-GeV protons directly from the AGS at intensities typical of an AHF. This will allow tests of thick, weapons-geometry objects at near-AHF conditions. Previous experiments at the AGS used secondary beams of lower energy and intensity. These provided some of the early concept validation of proton radiography and have set the stage for this next

step. Figure II-58 shows a proton radiograph of the French Test Object using 10-GeV protons at the AGS. The reconstructed densities and material boundaries are in good agreement with the known values. We plan to move the present proton-radiography experiments from Line B to the adjacent Line C, providing more space for multiple-lens configurations and larger containment vessels for larger HE charges. It is expected that this new area will be available for experiments in the FY98 run period at LANSCE.

Another major element of the program is development of high-resolution detection systems that are capable of multiple-frame recording. Since protons are charged, direct detection is possible. A prototype pixelated silicon array has been constructed, capable of buffering 1024 frames with 200-ns interfame separation. Electro-optic systems are also being developed. We anticipate that the testing of these systems will use the LANSCE beam and Line B apparatus over the next three years. This same setup can be used to evaluate and test new containment designs that would be applicable to the AHF requirements. Data from the Line B/C experiments will be used to benchmark and validate many aspects of the simulation and analysis effort for AHF development. At the end of this research and development program, proton radiography will be in a position to be evaluated, together with the other two technologies, as a viable tool for advanced radiography.

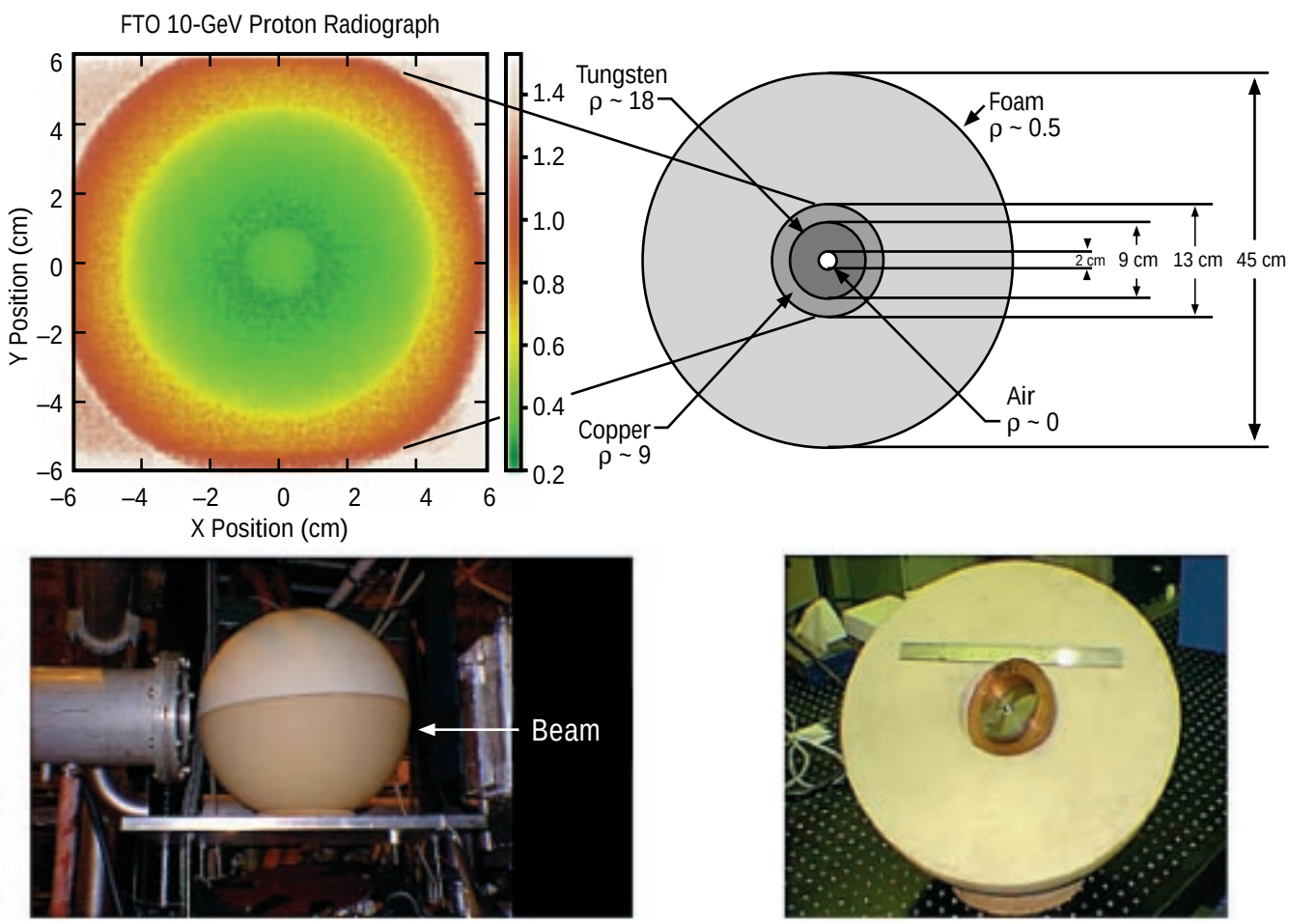

Fig. II-58. Proton radiograph of the French Test Object using 10-GeV protons from the AGS at BNL.